

Active origami platforms for human-robot interactions

Présentée le 2 septembre 2022

Faculté des sciences et techniques de l'ingénieur
Laboratoire de robotique reconfigurable
Programme doctoral en robotique, contrôle et systèmes intelligents

pour l'obtention du grade de Docteur ès Sciences

par

Frédéric Henri Vaskin GIRAUD

Acceptée sur proposition du jury

Prof. J. A. Schiffmann, président du jury
Prof. J. Paik, directrice de thèse
Prof. C. Pacchierotti, rapporteur
Prof. M. Wiertelowski, rapporteur
Prof. S. Henein, rapporteur

Abstract

Robots are employed to assist humans in lengthy, challenging, and repetitive tasks. However, the fields of rehabilitation, haptics, and assistive robotics have shown a significant need to support and interact with people in their everyday life. To facilitate these needs, robots must overcome constraints in compactness, degrees of freedom (DoF), and mechanical performance. First, these mechanisms should target the meso-scale to comply with human biomechanics, thereby enabling efficient and precise interactions. Subsequently, to evolve with humans, these robots should inherit the human versatility to face a constantly changing environment and adapt to many different tasks. Consequently, their mechanism should provide sufficient controllable DoF to enable multiple functionalities. Finally, the mechanical performances of these DoF should be compatible with the human bandwidth in force, speed, and motion range. However, making compact, mechanically efficient, and multi-functional robots is full of challenges requiring novel design, manufacturing, and control solutions. First, creating a meso-scale device requires careful material selection and the assembly of small components, which is laborious and increases manufacturing cost, time, and complexity. In addition, devices with several DoF and functionalities also require more parts to create numerous links and joints, actuators, and thus space, affecting the compactness of systems. Finally, aiming for mechanical performance in terms of force, speed, and motion range requires transmissions or bulky actuators, which also influence the size of the system. Therefore, achieving a suitable trade-off between functionalities, compactness, and mechanical performance is challenging as improving one criterion negatively influences the other two.

This thesis aims to bridge the gaps between compactness, DoF, and mechanical performance to design robots for human meso-scale interactions. Consequently, we address the following research questions:

How to design and improve the mechanical performance of robots at the meso-scale? Conventional mechanisms address this question by using mechanical transmissions that convert the actuator input into the desired force and motion output. However, the meso-scale renders the development of conventional transmissions system a challenge. This necessitates investigating novel mechanisms using alternative kinematics and joint types.

Can the number of DoF of a system be increased with minimal impact on its compactness? Developing structures with numerous degrees of freedom is challenging at meso-scale. Hence, there is a need to study novel designs and manufacturing methods that utilize material properties to efficiently create compact minimal assembly devices with numerous links and joints.

How can we optimize the robotic design trade-off between volumetric compactness, multi-DoF, and mechanically efficient platforms? Addressing previous questions requires innovative solutions in the design and manufacturing of meso-scale robots. Backed by these investigations, one can attempt to create the end-goal platform of this thesis.

How to interface this novel hardware to a computer for high-level control and simulation? Robot system developers need to provide an interface and a set of tools for users to program their hardware for different applications. This high-level control interface can be coupled with a simulation engine for visualization or achieving interactive tasks in a virtual environment. To overcome the limitations of conventional mechanics in answering our research questions, a novel robotic paradigm is required.

Origami robots are characterized by their quasi-2D structure, folding joints, and the subsequent manufacturing method: functional material layers are stacked to achieve low-profile and scalable structures that fold into 3D robots. This method considerably simplifies the assembly process and allows the creation of planar sheets with several joints. In addition, the latter can be combined with distributed actuation to self-fold into multiple shapes, thereby targeting a wide range of applications. Finally, this layered structure includes links and flexure joints that serve as compact kinematic transmissions when folded and connected to actuators. However, this technology has the following limitations. First, the lamination process renders the creation of joints other than flexure hinges challenging. Thus, pin joints are combined to generate the desired motion, affecting the system's compactness. This further complicates an already challenging design process that needs to allow folding the layers into a 3D robot with the required mechanical functionalities. Second, the mechanical characteristics of the actuators are limited at the meso-scale, affecting the overall performance of the system. Finally, using origami transmissions with conventional actuation does not solve the compactness issue due to the actuator size and the need for extra elements to connect motors and origami structure.

This thesis proposes novel origami robots to bridge the gaps between compactness, DoF, and mechanical performance for human meso-scale interactions. All four aforementioned research questions were addressed, leading to the development of hybrid robots combining the decades of experience of conventional mechanics with the advantages of origami robotics at the meso-scale.

First, to enhance the performances of robots at the meso-scale, the creation of compact *low-profile compliant transmissions* benefiting from origami's minimal assembly of functional layers was explored. The transmissions obtained can reproduce conventional kinematics or generate unconventional motions using materials properties.

Second, the development of multi-DoF compact robots was studied using the aforementioned low-profile compliant transmissions to create a multi-functional structure. The resulting robot is a fingertip haptic device called *Haptigami* that can render vibrotactile and three-DoF force feedback without compromising bulkiness.

Subsequently, backed by the previous investigations in design and manufacturing, this study

aimed at answering the main research question. We combined the previous device contributions and developed Flexure Variable Stiffness Actuators (*F-VSA*), a novel compliant actuator that uses the origami flexure hinges' inherent stiffness to avoid hindering mechanical simplicity.

Finally, we developed a software architecture that enables high-level control of the human-robot hardware and is compatible with multiple simulation engines. We used this architecture to control our robots and provide feedback to the user, based on interactions in a virtual environment.

These novel robots rely on non-conventional structures, actuators, and kinematics that require exploring and testing suitable control strategies. Hence, kinematic and stiffness models were developed and used to tune the position, force, and stiffness of the end-effector. Several characterization platforms and experimental protocols suitable for testing the precision and efficiency of our unique robotic systems were also created.

This thesis introduced new concepts to extend the current limits of robotics and avoid compromising between size, capabilities, and DoF of the robots at the meso-scale. Consequently, the results of this study pave the way for the development of robots that adapt to multiple environments, interactions, and application scenarios, compatible with the human bandwidth without hindering the user's motion and comfort in everyday life.

Résumé

Historiquement, les robots sont utilisés dans des environnements industriels pour aider les humains dans des tâches longues, difficiles et répétitives. Cependant, des domaines récents tels que la rééducation, l'haptique ou la robotique d'assistance nécessitent des systèmes pouvant être mis en œuvre en symbiose avec l'humain pour accompagner et interagir avec les personnes dans leur vie quotidienne. Pour répondre aux attentes de cette transition, les robots doivent satisfaire à des contraintes en termes de compacité, de degrés de liberté (DL) et de performances mécaniques. D'évidence, ils ne bénéficient plus de l'espace important disponible en milieu industriel et doivent éviter de gêner la mobilité et le confort de leurs utilisateurs du fait de leur taille. Ces mécanismes devraient cibler la méso-échelle pour adhérer à la biomécanique humaine permettant ainsi des interactions efficaces et précises. Par la suite, pour évoluer avec les humains, ces robots doivent hériter de la polyvalence humaine pour faire face à des environnements diversifiés et changeants et s'adapter à de nombreuses tâches différentes. Par conséquent, leur mécanisme devrait fournir suffisamment de DL contrôlables pour permettre de multiples fonctionnalités. Enfin, les performances mécaniques de ces DL doivent être compatibles avec les capacités sensori motrices humaines en termes de force, de vitesse et d'amplitude de mouvement. Fabriquer des robots compacts, mécaniquement efficaces et multifonctionnels est une tâche complexe si l'on réfléchit seulement en termes de miniaturisation des systèmes mécaniques conventionnels. En premier lieu, la création d'un dispositif à l'échelle centimétrique (méso-échelle) nécessite une sélection minutieuse des matériaux et l'assemblage de petits composants; cela trouve sa traduction en termes de temps, de complexité de fabrication et finalement de coût. En outre l'impératif de multiples DL et fonctionnalités augmente également le nombre de pièces utilisées à la création de nombreux liens et articulations. Ajoutons à cela la nécessité d'actionneurs supplémentaires. Cette inflation de composants est gourmande en espace, affectant la compacité des systèmes. Viser des performances mécaniques comme force, vitesse et amplitude de mouvement fait croître également la taille du système exigeant des transmissions ou des actionneurs encombrants. Par conséquent, parvenir au compromis pertinent entre fonctionnalités, compacité et performances est un défi car l'amélioration d'un critère influence négativement les deux autres.

Cette thèse a l'ambition de s'inscrire dans le cadre général de l'amélioration et de la création de systèmes robotiques capables d'interagir avec l'être humain à l'échelle millimétrique.

Précisément, elle se propose de contribuer à concilier mieux les exigences parfois antagonistes évoquées ci-dessus de la compacité, des degrés de liberté, des performances mécaniques dans la conception de tels systèmes robotiques.

A cette fin, les quatre questions de recherche suivantes se sont imposées à notre démarche :

Comment concevoir et améliorer les performances mécaniques des robots à l'échelle méso ? Les mécanismes conventionnels répondent à cette question en utilisant des transmissions mécaniques, puis en convertissant le mouvement généré par l'actionneur en force et déplacements souhaités. L'échelle méso rend le développement d'un tel système de transmissions difficile. La réponse sera recherchée par l'étude de nouveaux mécanismes utilisant des cinématiques et des types d'articulations alternatifs.

Peut-on augmenter le nombre de DL d'un système avec un impact minimal sur sa compacité ? Cet objectif implique le développement de structures à nombreux degrés de liberté, ce qui est difficile à méso-échelle. Pour le rendre possible, il est nécessaire d'étudier les nouvelles méthodes de conception et de fabrication qui utilisent les propriétés des matériaux. Il s'agit de créer de nouveaux dispositifs d'assemblage, simplifiés, compacts, avec de nombreuses pièces rigides ou souples et des articulations que ces matériaux rendent imaginables.

Comment créer des plates-formes compactes, multi-DL et mécaniquement efficaces pour les interactions homme-robot ? Les questions précédentes soutiennent des solutions innovantes dans la conception et la fabrication de mécanismes à méso-échelle. En s'appuyant sur ces investigations, on peut tenter de créer le prototype qui répond à l'objectif final de cette thèse.

Comment interfacier ce nouveau matériel à un ordinateur pour un contrôle et une simulation ? Les développeurs de robots doivent fournir une interface et un ensemble d'outils permettant aux utilisateurs de programmer leur matériel pour différentes applications. Cet environnement de contrôle peut être couplé à un moteur de simulation pour visualiser ou réaliser des tâches interactives dans un monde virtuel.

Pour surmonter les limites actuelles de la mécanique conventionnelle et se conformer à nos objectifs de recherche, un nouveau paradigme robotique est nécessaire.

Nous avons interrogé les possibilités intéressantes offertes en ce sens par les robots Origami ; Ils se caractérisent par leur méthode de fabrication dans laquelle des couches de matériaux fonctionnels sont empilées pour obtenir des structures discrètes et évolutives qui se replient en robots 3D. Cette méthode simplifie considérablement le processus d'assemblage et permet la création de structures planes à plusieurs joints. Ces structures actionnées pour se plier automatiquement en plusieurs formes autorisent un large éventail d'applications. Cet empilement peut être utilisé comme transmission compacte après pliage et connexion aux actionneurs.

Cependant, l'état de l'art de cette technologie est actuellement limité. Tout d'abord, le processus de stratification rend difficile la création de joints autres que les charnières flexibles. La nécessité de combiner plusieurs liaisons pivot pour générer le mouvement souhaité, affecte la compacité du système. Cela complique davantage un processus de conception déjà difficile qui devrait permettre au mécanisme de se plier en robot 3D en conservant ses fonctionnalités. En outre, une multitude de DL est difficile à contrôler et actionner. Elle supposerait l'intégra-

tion d'actionneurs et de mécanismes supplémentaires au détriment de l'encombrement. Par ailleurs, les caractéristiques mécaniques limitées des actionneurs à méso-échelle diminuent les performances globales du système. On le comprend, malgré leurs performances en termes de vitesse et de force, l'utilisation de transmissions origami avec actionnement conventionnel ne résout pas en l'état du moins, les problèmes de compacité. En résumé les inconvénients sont liés à la taille de l'actionneur, au besoin d'éléments supplémentaires pour connecter moteurs et structure origami, et au processus d'assemblage.

Cette thèse fait néanmoins le choix d'utiliser la robotique "Origami" inspirante en termes de diversité de solutions, très stimulante dans l'invention de nouvelles formes de robots capables à petite échelle de mouvements complexes. Elle cherche à l'améliorer pour favoriser une miniaturisation des robots qui n'altère pas leurs performances tant mécaniques que relatives aux degrés de liberté. Les trois premières questions de recherche susmentionnées ont été abordées, menant respectivement à la création de trois robots hybrides combinant les décennies d'expérience de la mécanique conventionnelle avec les avantages de la robotique origami à méso-échelle. La quatrième question occupe nécessairement la dernière partie de notre travail et s'attache à la conception de l'outil informatique de contrôle et d'adaptation du robot par l'utilisateur, elle s'accompagne de la conception matérielle et mathématique d'outils de mesure et de test. Reprenons chronologiquement ces quatre directions de recherche pour en préciser les apports :

Le premier projet a permis d'améliorer les performances des robots à l'échelle méso. Nous avons exploré la pertinence de créer des transmissions de type origami compactes bénéficiant de l'assemblage simplifié de couches fonctionnelles. Les transmissions obtenues peuvent reproduire des cinématiques conventionnelles ou générer des mouvements non conventionnels en utilisant les propriétés des matériaux.

Le deuxième projet s'attache au développement de robots compacts multi-DL utilisant les transmissions de type origami susmentionnées pour créer une structure multifonctionnelle. Le robot résultant est un dispositif haptique au contact de la dernière phalange des doigts de la main appelé *Haptigami*. Il permet un retour haptique vibrotactile selon trois degrés de liberté avec une compacité optimisée.

Le troisième projet complète les précédents en faisant la démonstration qu'il est possible de concilier compacité, degrés de liberté et performances mécaniques. En s'appuyant sur les contributions des deux projets précédents, nous avons pu réaliser des actionneurs à rigidité variable utilisant des charnières flexibles de type origami possédant spontanément une rigidité inhérente (F -VSA).

Quatrièmement, nous avons créé une architecture logicielle qui permet un contrôle d'interfaces homme-robot et qui est compatible avec plusieurs moteurs de simulation. Nous avons utilisé cette architecture pour contrôler nos robots et donner un retour à l'utilisateur en fonction des interactions se produisant dans un environnement virtuel.

Ces robots reposent sur des structures, des actionneurs et une cinématique non conventionnelle qui nécessitent d'explorer et de tester des stratégies de contrôle appropriées. Par conséquent, des modèles mathématiques (cinématique et de rigidité) ont été développés et

utilisés par la suite comme base pour ajuster les caractéristiques des mouvements du robot (position, force et rigidité). Enfin, pour évaluer la précision des modèles mathématiques proposés et l'efficacité des robots dans la réalisation d'une tâche, nous avons développé plusieurs plateformes de caractérisation ainsi que des protocoles expérimentaux adaptés pour tester les systèmes robotiques uniques décrits ici.

Ainsi, à travers ces quatre plateformes robotiques, cette thèse a introduit plusieurs idées pour repousser les limites actuelles de la robotique. Les concepteurs peuvent utiliser ces innovations pour éviter les compromis entre la taille, les capacités et les fonctionnalités à méso-échelle. Les résultats de cette étude devraient ouvrir la voie aux robots pour s'adapter à de multiples environnements, interactions et scénarios d'application, compatibles avec les capacités sensori motrices humaines sans entraver le mouvement et le confort de l'utilisateur. Cette thèse trouve également sa motivation dans l'horizon plus large d'une collaboration améliorée et plus harmonieuse entre robots et humains à laquelle nous espérons avoir apporté notre part modeste mais concrète.

Acknowledgements

I would like to express my gratitude to my supervisor Prof. Jamie Paik for giving me the opportunity to work in this great laboratory. She is the reason why RRL, my second home for the last four years, has been such a stimulating, rewarding, and supporting environment. I am thankful for her mentoring during my numerous PhD's adventures that strongly encouraged my professional and personal development.

I am incredibly grateful to my thesis committee, Prof. Schiffmann Jurg, Prof. Henein Simon, Prof. Wiertlewski Michaël, Prof. Pacchierotti Claudio for reviewing my work and providing insightful comments and suggestions.

Hardship reveals friendship, and I am extremely thankful to all the lab members for all these fulfilling moments that helped me through deadlines and disobedient robots. I owe an important part of my progress to the mentoring of the first RRL generation: Peter, Matt, Chris Zhenishbek, and Harshal. This also includes my travel partners Jian-lin and Sagar, that have always been a strong and reliable, moral and scientific support. I was part of the new RRL generation with Fabio, Anastasia, Kevin, and Mete, the best possible cohesive team to face the hazard of PhD life, but also to throw celebrations for all the milestones. They are also decent Super Smash Bros opponents.

I am deeply indebted to my family: Roland for offering his precious help in last minutes manufacturing and proofreading, Eliz for her artistic insight, and in particular my parents for believing in me and supporting me in every way possible. I would not be where I am without their constant encouragement in pursuing my studies.

I am also thankful to the friends I made and evolved with during my academic life that pushed me forward in many ways: Julien, Álvaro, Nathan, Felix, Laurent, Iñaki, and Michael.

Last but not least, I am deeply grateful to Orane for everything. Her unwavering support and cheerfulness from the start to the very end were the backbone of my work and determination.

Lausanne, June 20, 2022

F. G.

Contents

Abstract (English/Français)	i
Acknowledgements	ix
List of Figures	xv
List of Tables	xvii
Introduction	1
1 Design of low-profile compliant transmission mechanisms	17
1.1 Introduction	17
1.2 Conventional Transmissions	19
1.2.1 Slider-crank	20
1.2.2 Cam-follower	21
1.3 Design and Modelling of multi-layers low-profile transmissions	21
1.3.1 General design considerations	21
1.3.2 Slider-crank	22
1.3.3 Cam-follower	24
1.4 Manufacturing process of multi-layer low-profile transmission mechanisms . .	26
1.4.1 Mechanisms	26
1.4.2 Actuation	28
	xi

Contents

1.5	Experiments and characterization	29
1.5.1	Kinematics	29
1.5.2	Pulling force	30
1.6	Discussion and conclusion	31
2	Haptigami: a fingertip haptic interface with cutaneous force feedback	33
2.1	Introduction	33
2.2	Haptic feedback of wearable fingertip devices	36
2.3	Design and fabrication of an origami-inspired haptic platform with integrated transmissions	38
2.3.1	Actuation and closed-loop control of the piezo-motors	38
2.3.2	Low-profile compliant slider-crank mechanism	39
2.3.3	Origami-inspired base structure with embedded transmissions	40
2.3.4	Working principle	40
2.4	Kinematic model of Haptigami	41
2.4.1	Kinematic model	41
2.4.2	Kinematics validation	44
2.4.3	Maximal roll and pitch frequencies	45
2.5	Force characterization	45
2.5.1	Experimental setup	45
2.5.2	Pitch and roll	47
2.5.3	Compression	48
2.5.4	Vibrotactile feedback	48
2.6	Conclusion and future work	49
3	Flexure Variable Stiffness Actuators	51
3.1	Introduction	51

3.2	Flexure Variable Stiffness Actuator overview	54
3.2.1	F-VSA design and features	54
3.2.2	Matrix Structural Analysis method overview	55
3.3	F-VSA system: a four-DoF device with force and stiffness output	58
3.3.1	Design and capabilities	58
3.3.2	Manufacturing methods	60
3.3.3	Origami fabrication of the F-VSA system	61
3.3.4	System description for the MSA	62
3.3.5	Force and stiffness control strategy	64
3.3.6	Actuators and sensing	65
3.4	Design of experiment	65
3.4.1	Experimental setup	66
3.4.2	Stiffness modulation experiment	67
3.4.3	Force control experiment	67
3.5	Experimental results	68
3.5.1	Stiffness modulation results	69
3.5.2	Force control results	70
3.6	Conclusion and Future work	70
4	Robot-computer interface and simulation	73
4.1	Challenges in robotic software development	73
4.2	Communication interface architecture	74
4.2.1	Hardware	75
4.2.2	High-level control	75
4.2.3	Simulation engine	75
4.3	Application examples	76

Contents

4.3.1 Haptigami	76
4.3.2 F-VSA system	77
4.3.3 Hand-grasped kinesthetic haptic device	78
4.4 Conclusion	79
5 Conclusion and future outlook	81
A Appendices	89
A.1 Slider-crank mechanism CAD design	90
A.2 Cam-follower mechanism CAD design	91
A.3 Haptigami CAD design	91
A.4 F-VSA CAD design	94
A.5 Workplace determination	94
A.6 Matrix Structural Analysis	95
A.7 Modeling example: MSA applied to a diamond	97
Bibliography	99

List of Figures

1	The state-of-the-art of compactness in origami robotics	5
2	The state-of-the-art of multi-DoF origami robots	6
3	The state-of-the-art of mechanically capable origami robots	8
4	Advantages and limitations of origami robotics and thesis objectives	9
1.1	Transfer of conventional mechanisms into quasi-2D systems	18
1.2	Kinematic schematic for slider-crank and cam-follower low-profile mechanisms	20
1.3	Layer-by-layer representation of the slider-crank and cam-follower low-profile mechanisms	22
1.4	Manufacturing process for low-profile compliant mechanisms	27
1.5	PCBmotor assembly and optical sensors integration	28
1.6	Experimental setup used to measure the low-profile transmissions' force and motion	29
1.7	Experimental results of force and kinematic experiment	30
2.1	Haptigami on finger and degrees of freedom presentation	34
2.2	Cutaneous feedback capabilities	35
2.3	Comparison of Haptigami with state-of-the-art haptic devices in terms of number of functionalities and wearability	36
2.4	PCBmotors integration with magnetic encoders	38
2.5	Haptigami's mechanism and fabrication	39
2.6	Haptigami's kinematic model and closed-loop control experiment and results .	42

List of Figures

2.7	Force characterization setup and results	46
3.1	The flexure variable stiffness actuator system	52
3.2	Comparison of SEAs, VSAs, and F-VSAs	54
3.3	Working principle of the F-VSA system	58
3.4	Proofs of concept using four manufacturing methods	60
3.5	Origami folding sequence of the F-VSA system	62
3.6	Description of the F-VSA system for the MSA method	63
3.7	Experimental setup design to measure the end-effector force of the F-VSA system in all the workspace	66
3.8	Stiffness characterization of the F-VSA system	69
3.9	Control of the F-VSA system to render a vortex-shaped force field	71
4.1	General interface architecture	74
4.2	Haptigami interface	77
4.3	F-VSA system interface	78
4.4	Hand-grasped kinesthetic haptic device interface	80
A.1	Slider-crank mechanism CAD design	90
A.2	Cam-follower CAD design	91
A.3	Haptigami CAD design - floor 1	92
A.4	Haptigami CAD design - floor 2	93
A.5	F-VSA CAD design	94
A.6	MSA model of a single diamond	97



List of Tables

2.1	Haptigami motion achieved through motors direction of rotation	41
2.2	Haptigami's maximal force capabilities	49
3.1	Relation between force vector and pair of motors	67
3.2	Mechanical capabilities of the F-VSA system	68

Introduction

Robots have been primarily used by humans employing a controller-peripheral method to achieve repetitive tasks in a defined environment adapted to their characteristics. The research regarding human-robot interactions (HRI) has aimed at extending the use of robots in numerous other fields [1–3] by amalgamating the cognitive abilities of humans with the mechanical capabilities of robots. In particular, HRI contributes to assistive robotics, medical applications, or enhancing physical capabilities where the robot output is directly connected to the human. This is a continuous interaction where the user adapts their force and motion input to the feedback returned by the robot. These types of collaborations demand the robots to be compact, versatile with multiple-DoF, and yet mechanically capable.

- **Compactness:** Low-profile and lightweight mechanisms are agile and can considerably improve HRI devices. Owing to the compactness of the mechanisms, multiples of them can be embedded in a device, increasing number of functionality while maintaining its overall volume and size. In particular, compactness considerably improves wearable technologies or the field of haptics that is sensitive to space constraints because the device weight and volume can severely impact the targeted feedback.
- **Degrees of Freedom:** Robots with numerous DoF are agile and can address multiple tasks and adapt to different environments. They can even reconfigure depending on the targeted application. In addition to improving the device's capabilities, DoF contribute to effective HRI, as robots must be compatible with the human workspace and sensory system's DoF. In order for a device to be more wearable, it is critical to match the system's compliance to the human biomechanics, and it usually requires not only a material-level compliance matching, but also an increased number of controllable DoF to match the biomechanical capabilities.
- **Mechanical capabilities:** It defines the speed, force, and range of motion of each DoF of the robot. The mechanical capabilities should be compatible with the targeted application and fit the human somatosensory and motor capabilities for HRI.

It is challenging to combine these features into a compact, multi-DoF, and mechanically capable system.

Conventional mechanisms' challenges at the meso-scale

Robotic mechanisms rely on the 3D assembly of complex components and systems dedicated to a task. These parts are combined to create actuators that produce the initial motion, and mechanisms that transform and transfer this motion to the end-effector. The mechanisms modify the mechanical capabilities of the actuator, such as the force, speed, and range of motion to fit the application. Currently, most industrial robots are dedicated to a single task that must be performed with high speed and precision. However, their fundamental manufacturing methods and working principle limit combining compactness, multiple DoF, and high mechanical capabilities in a single system.

Manufacturing challenges for compactness

Most industrial robots have few spatial constraints, and their overall size is often not an issue. Their links and joints are composed of multiple parts with materials and thickness chosen to ensure rigidity, robustness, and ability to withstand strong forces. However, it is difficult to transfer these assets of industrial robots to target meso-scale applications. As the dimensions of the robots are reduced, the material thickness is also lower, thereby affecting rigidity and robustness. Therefore, the design of meso-scale robots requires the careful selection of materials with properties and design suitable for the application despite the small components' cross-sectional dimension. Regarding the robots' manufacturing process, industrial fabrication chains require multiple DoF to create complex 3D robots. This method is difficult to apply at the meso-scale where the assembly challenges are multiplied and requires high precision and complex machines to handle small components. Hence, novel assembly-free or minimal assembly manufacturing methods that can mass-produce miniature robotic systems must be investigated. Finally, these items are closely interlinked together, and thus, the compatibility between material choice, dimensions, and manufacturing process must be ensured. Combining these points and creating a compact and resistant robot that is easy to design and fabricate complicates the problem further.

Compact robots with multiple DoF

Most conventional mechanisms are made of several rigid components that are difficult to miniaturize without hindering their mechanical characteristics. Hence, increasing the number of DoF requires additional components that affect the system size. This compromise between meso-scale and DoF requires studying novel manufacturing methods and combining them with a careful material selection. The number of actuators must be increased to control a system with a large number of DoF. As the size of the actuators is often linked to their capabilities, they require sufficient volume to generate enough forces for the application, rendering the integration of multiple actuators into small systems with numerous joints a challenging task. The development of novel actuators that rely on different physical principles of their materials can facilitate this integration.

Mechanically capable meso-scale robots

Mechanical efficiency is defined as the DoF's characteristics in terms of force, speed, and the range of motion. In common mechanisms, actuators provide the initial input tuned and transformed by the transmissions. Since the size of the actuators is directly related to their capabilities, implementing a mechanically capable system at the meso-scale is challenging. For example, a higher volume can accommodate bigger coils for electromagnetic actuators or increased pneumatic piston surface areas, resulting in increased torque and force outputs. Hence, small systems that require a large force output must explore other physical principles for their actuation, that do not trade size with capabilities. Transmissions often solve the actuator's capabilities issue. However, their implementation is challenging at the meso-scale. First, they consist of several joints and links that are difficult to miniaturize. Then, the transmissions' design directly affects their mechanical capabilities: a longer lever arm produces more torque, a larger crank produces more displacement, etc... This design constraint makes it difficult to achieve the desired output with a compact design. Lastly, friction loss has a greater impact on the mechanical capabilities at the meso-scale owing to reduced system forces. Miniature robots necessitate the development of novel, compact, and capable transmissions with a large output range. This can be achieved by exploiting alternative manufacturing processes, smart materials, and new design methodologies.

This section highlighted the difficult trade-offs between compactness, functionalities, and mechanical capabilities. When attempting to increase the number of functionalities or enhance the capabilities of a robot, the compactness is negatively affected. Meanwhile, reducing the system size is challenging for the manufacturing process and material robustness. This trade-off is an important limitation of the current HRI systems since most of them use conventional mechanics to achieve their functionalities. A discussion about the impact of these limitations on the state-of-the-art of wearable haptic devices can be found in section 2.2. The objective of this thesis is to investigate novel designs and methods to achieve this trade-off and improve HRI devices.

Research questions

As stated, there are gaps between the three main design of meso-scale robotic systems: compactness, multiple DoF, and mechanical capabilities. In this thesis, I investigated the following questions:

First, to adapt the actuators' input in terms of speed, force, and displacement, any robotic system uses transmissions. However, transmissions are often made of several rigid components that are difficult to scale down and use. Therefore, I addressed the question *How to design and improve the mechanical capabilities of robots at the meso-scale?* by developing novel transmissions that rely on new manufacturing processes and material properties to recreate or reinvent the conventional transmission's kinematics.

Second, increasing the number of DoF augments the form factor of the robot because

of additional components and actuators. Hence, the question *Can the number of DoF of a system be increased with minimal impact on its compactness?* I achieved this trade-off by using intelligent design methods and novel fabrications techniques to optimally utilize material properties and create compact devices with numerous links and joints.

Consequently, by combining the previous questions' results in terms of design and manufacturing, I was able to investigate this thesis' main research objective: *How can we optimize the robotic design trade-off between volumetric compactness, multi-DoF, and mechanically capable platforms?*

Finally, any robotic designer has to address *How to interface this novel hardware to a computer for high-level control and simulation?* For this purpose, I propose a framework architecture that enables the users to control and use these novel platforms for multiple applications, therefore improving their distribution and impact.

The working principle and manufacturing methods of conventional mechanisms are insufficient for addressing these questions. Thus, there is a need for a new robotic paradigm that can overcome the current limitations. This thesis attempts to answer these questions using origami robots, an alternative design approach for creating meso-scale robots with numerous folding joints.

Origami robots as a solution for compact meso-scale mechanisms

Origami robotics, also known as Robogamis [4–6] uses a new robotic design paradigm. It relies on a lamination process to create quasi-2D structures that fold into 3D mechanisms efficiently. It uses functional layers with different material properties to create and embed links, joints, sensors, and actuators. This robotic design method offers the advantage of MEMS manufacturing in terms of high customizability and mass production at the meso- and macro-scales. The resulting robots are compact, scalable, and versatile with a large number of DoF. In addition, they rely on a fast, cheap, and assembly-free manufacturing technique, and thus, can overcome the limitations of conventional robots. This section presents the improvements and current constraints of origami robotics regarding each criterion from the trade-off between compactness, DoF, and mechanical capabilities.

Compactness of origami robots

The manufacturing process of origami robots consists of the 2D assembly of layers of materials with different functionalities. In contrast to conventional mechanisms that rely on rigid components to create links and joints, origami robotics exploit the material's mechanical properties. Hence, the layers of rigid materials such as *FR4* or *acrylic* can be used for the links and flexible materials like *Kapton* or *PET* for the joints. Another method involves using a single material for the entire system and adapting its stiffness locally by changing the material's thickness. Therefore, the system's mechanical properties are fully determined by the choice of materials and do not require the use of additional bulky components, which improves

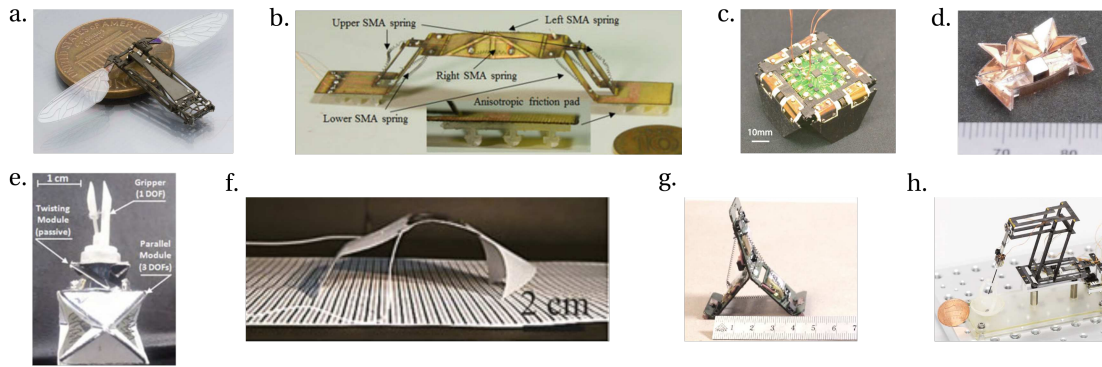


Figure 1: The state-of-the-art of compactness in origami robotics. Origami robots can be compact due to their low-profile support structure, folding joints, and heat or electromechanical actuation. a. Monolithic fabrication of millimeter-scale machines [7], b. Omega-Shaped Inchworm-Inspired Crawling Robot With Large-Index-and-Pitch (LIP) SMA Spring Actuators [8], c. Robogami: A Fully Integrated Low-Profile Robotic Origami [4], d. An Untethered Miniature Origami Robot that Self-folds, Walks, Swims, and Degrades [9], e. A Novel 4-DOF Origami Grasper With an SMA-Actuation System for Minimally Invasive Surgery [10], f. Origami Robot: A Self-Folding Paper Robot With an Electrothermal Actuator Created by Printing [11], g. Designing minimal and scalable insect-inspired multi-locomotion millirobots [12], h. Origami-inspired miniature manipulator for teleoperated microsurgery [13]

the system's compactness. Robots made of functional materials are shown in Fig. 1 and use two main actuation methods. The first one is a thermally activated smart-materials used as actuators or joints in [4, 8–10, 12] or thermal expansive materials [11] to induce deformation of the origami structure. Then, piezo-crystals are combined with the origami structure as a transmission and actuators to make the Robobee [7] fly, or position a manipulator's end-effector [13].

Origami robots also owe their compactness to the lamination process: a minimal assembly method where the layers of functional materials are stacked together. In addition to rigid and flexible layers that define links and joints, the functional layers also include actuators and sensors. Instead of a complex assembly in the 3D space used in conventional mechanics, the lamination process only requires a precise alignment of the layers and an adhesive to fix them together. Therefore, the system is built as a whole, simplifying its assembly and eliminating the need to fabricate nor assemble small components such as bolts and screws. In addition to solving the meso-scale manufacturing issues, this method is scalable and can be transferable at the macro-scale as long as the layers' sizes are compatible with the machines in charge of the lamination. From all the robots presented in Fig. 1, only [11] does not use lamination. Instead, it employs a printer to depose the layers of materials.

However, origami robotic flexure hinges suffer from two main limitations. First, although the lamination process is efficient for creating folding joints, it is laborious when developing other joint types. For example, a linear joint requires the combination of several folding joints, which complicates the overall structure and design. Hence, the compactness gained

Introduction

by material selection and layer-by-layer manufacturing is lost with the increase in links and folding joints, combined to achieve the desired motion of the end-effector. This additional complexity also results in a more laborious design process.

In addition, during the design of origami robots, the folding process that transforms the 2D stack of functional layers into a 3D structure must be considered. This step is not needed in conventional robotics, where the design directly represents the system's final state. Therefore, the crease pattern's design process should guarantee that the sheet folds into the desired shape and performs the intended task correctly. This is an important design challenge due to the lack of simulation tools and design software for origami robots. Thus, these constraints limit the capabilities of origami robotics to achieve complex devices at the meso-scale.

Multi-DoF system

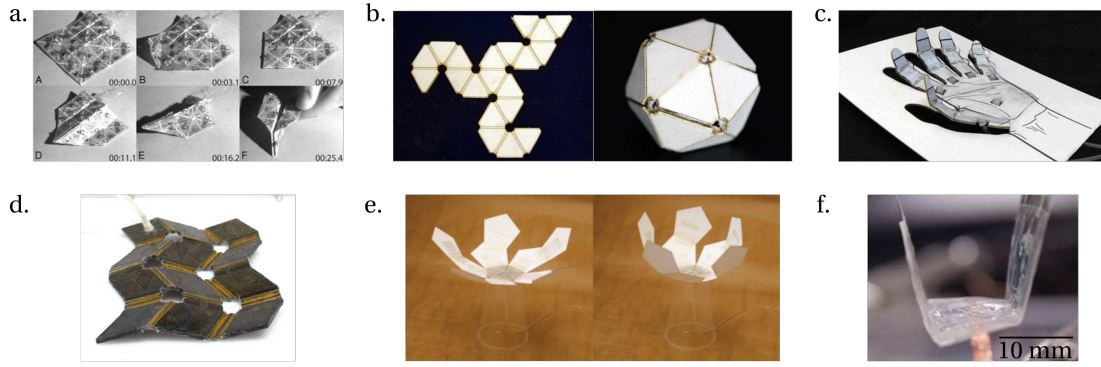


Figure 2: State-of-the-art multi-DoF origami robots. These devices can reconfigure owing to their numerous DoF and distributed actuation method. a. Robotic origamis: self-morphing modular robots [14], b. Self-folding origami: shape memory composites activated by uniform heating [15], c. Pouch Motors: Printable Soft Actuators Integrated with Computational Design [16], d. Programmable Fluidic Networks Design for Robotic Origami Sequential Self-Folding [17], e. Self-folding and Self-actuating Robots: a Pneumatic Approach [18], f. Reconfigurable and programmable origami dielectric elastomer actuators with 3D shape morphing and emissive architectures [19]

Owing to their 2D folding design, origami robots provide a platform for the development of multi-DoF robots with sufficient mechanical flexibility to adapt to several environments and scenarios. This is because the lamination process makes the creation of numerous links and joints easy and efficient, providing the resulting sheet with numerous DoF. Consequently, the robot attains the ability to fold into a 3D structure while providing the end-effector with sufficient workspace to perform multiple tasks. Moreover, several 3D configurations can be achieved from a single sheet. Hence, the origami robot can select the folding steps to reach the most efficient configuration for a specific task. Finally, multiple DoF make the overall structure compliant, comfortable, and safe for human interaction. Figure 2 shows the state-of-the-art regarding robots with numerous DoF.

Most robots use a distributed actuation strategy for a multitude of joints. It involves attach-

ing a bending actuator to each joint during the manufacturing process. Since electromagnetic actuators can lead to compactness issues, origami robots rely on other physical principles. Diverse origami robots have been constructed by distributing bending [20, 21] or linear [22] SMAs [15, 18, 23]. Alternatively, pneumatically-driven origami mechanisms [16, 17] and dielectric elastomer actuators (DEAs) [19] are used to fold multi-hinged patterns with complex deformation physics. Despite their small volume, these actuation methods generate high forces and are easy to integrate as a functional layer during the manufacturing process. They provide origami robotics with multiple controllable DoF without affecting the system's compactness. Furthermore, their range of force match the human motor capabilities.

Unfortunately, the power and compactness of smart and pneumatic actuators are attained at a cost. Achieving a reconfigurable and multi-DoF compact system requires overcoming the challenges and control issues of the actuators. First, commonly used distributed actuators suffers from limitations that affect the multi-DoF origami robot's capabilities to interact with humans. For example, SMAs have high power consumption, DEAs are actuated by high voltage, and pneumatic actuators require a pressurized air supply. These requisites render their integration into wearable applications challenging. In addition, they have irreversible motion and must rely on an antagonist pair or springs to return to a resting position, making the system more complex and less compact. Finally, SMAs and pneumatic actuators have low bandwidth, thereby limiting the application range of origami robotics.

Compared to electromagnetic devices, SMAs, DEAs, and pneumatic actuators are non-linear systems whose position control is challenging. They often require advanced or data-driven modeling, which affects their deployment outside a laboratory environment. In addition to the actuators' limitations, a system with numerous degrees of freedom is challenging to control. The system is required to select the best strategy to achieve a specific task, rendering the solving of the reverse kinematics laborious. Furthermore, the overall system reconfiguration requires determining the folding sequence that minimizes the energy loss and prevention of self-collision [24, 25].

Owing to origami robotics, making a multi-DoF structure without compromising compactness is achievable. However, the limited actuator performances affect overall system capabilities and require complex modeling or novel control methods to reconfigure and perform tasks.

Mechanical capabilities in origami robots

Origami robots rely on flexure joints to improve the mechanism compactness by reducing the number of parts, they exhibit superior mechanical properties. First, they consist of a single part, thereby eliminating friction. This is advantageous at the meso-scale, where friction cannot be neglected compared to the amplitude of other internal and external forces. The absence of friction reduces the wear of joints and they do not require maintenance or extra lubrication. Finally, these joints do not have play, making them desirable for precision applications.

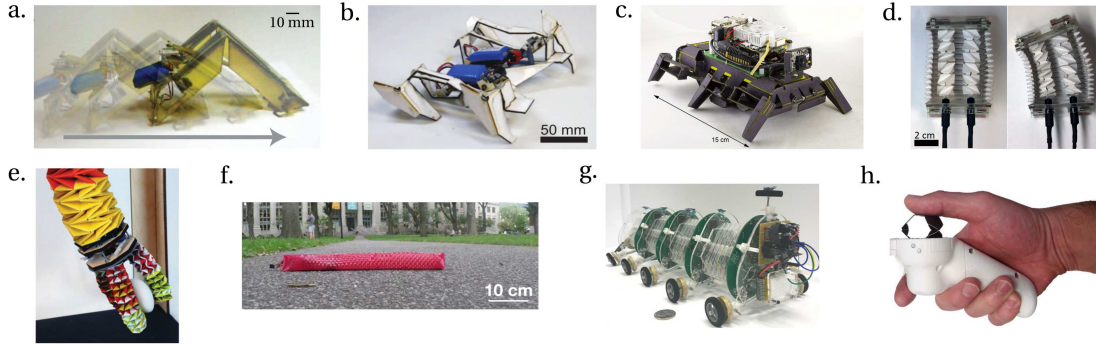


Figure 3: State-of-the-art of mechanically capable origami robots. They use origami as kinematic transmissions to achieve their task with improved force, speed, and motion range. a. Robot Self-Assembly by Folding: A Printed Inchworm Robot [26], b. A method for building self-folding machines [27], c. Integrated Manufacture of Exoskeletons and Sensing Structures for Folded Millirobots [28], d. A crawling robot driven by multi-stable origami [29], e. Design and analysis of an origami-based three-finger manipulator [30], f. Kirigami skins make a simple soft actuator crawl [31], g. OriSnake: Design, Fabrication, and Experimental Analysis of a 3-D Origami Snake Robot [32], h. A portable three-degrees-of-freedom force feedback origami robot for human–robot interactions [33]

Since origami robots are both compact and mechanically capable, several applications such as origami-based transmissions have been developed. They are mechanisms actuated by rotary motors using tendons to transmit the rotational motion and fold the origami joints [30, 32], or actuate legged robots [26–28, 34, 35]. Thus, despite their compactness, origami transmissions provide efficient force transfer from the motor to the end-effector, such as in a force feedback joystick [33]. Furthermore, origami transmissions can efficiently convert motion, as seen in two crawlers. First, Pagano et al. [29] converted the rotary motion of conventional actuators into linear motion. Thereafter, Rafsanjani et al. [31] used the actuator’s linear motion to move forward and change the surface friction coefficient simultaneously through an origami skin. This allowed the reproduction of capable macro-scale mechanisms at the meso-scale with controllable and reversible motions.

These items demonstrate the ability of origami robotics to create a mechanically capable system. However, previous studies that have exploited origami transmissions suffer from limitations regarding miniaturization. First, although origami structures create capable transmission mechanisms, they require powerful actuators to induce a motion that fits the application’s expectations at the end-effector. Moreover, flexure hinges have an inherent stiffness that can increase the actuator’s load.

In addition, most actuators have a rotary motion that is challenging to couple with the DoF of an origami hinge. A direct connection between a traditional DC motor and flexure joint requires torque, which is difficult to generate at the meso-scale for electromagnetic devices. Hence there is still a need to convert the force and speed of the actuators before connecting them to the origami structure and origami robotics does not eliminate the need for gears or

extra transmission.

Hence, although origami robotics can create capable transmissions that improve the mechanism's overall capabilities, they require actuators and transmissions. This requirement does not solve the trade-off between compactness and mechanical capabilities despite the step forward.

Thesis structure and contributions

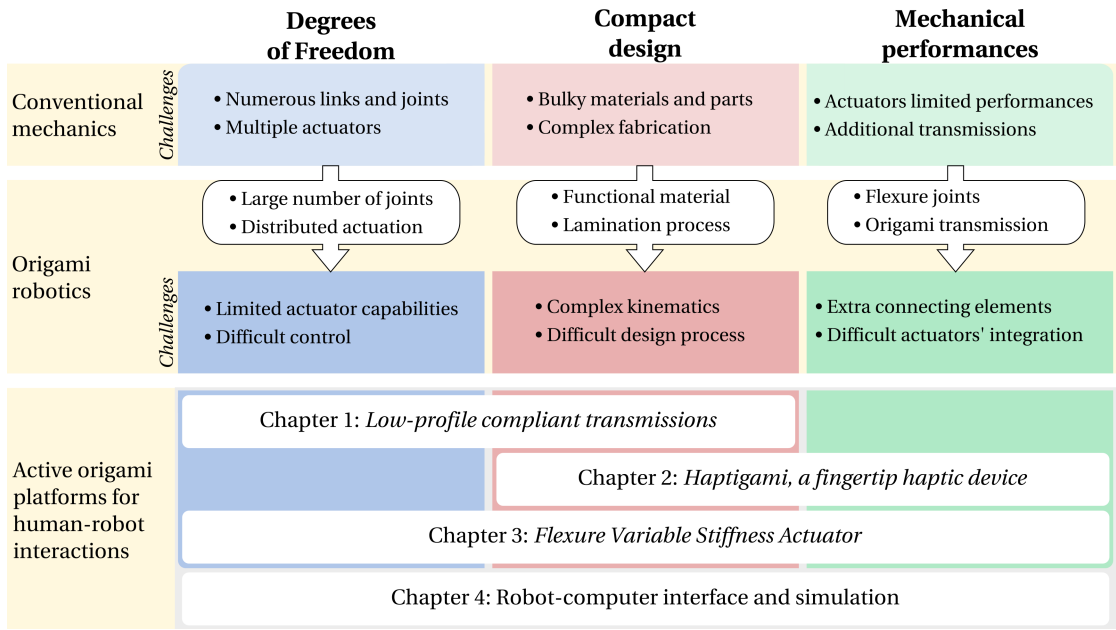


Figure 4: Advantages and limitations of origami robotics and thesis objectives. This study aims to create a meso-scale multi-DoF capable robotic system. This is challenging using conventional mechanics, as it relies on a complex assembly of bulky elements and actuators with limited capabilities at the meso-scale. Origami robotics, a new paradigm in robots, is an interesting candidate. It uses a lamination process, functional materials, and non-conventional actuation to create compact and capable mechanisms with multiple joints. However, current state-of-the-art origami robotics suffer from design, kinematic, and actuation limitations. This thesis aims to overcome these limitations and enable the creation of active platforms for human-robot interactions.

Origami robotics have the potential to develop new methods to fabricate meso-scale systems while pushing the limitations of conventional robotics. Researchers have exploited the advantages of origami robotics in developing either compact, multi-DoF, or mechanically capable robots. However, although the gaps between these three pillars are reducing, there exist challenges that prevent their complete closure. Figure 4 illustrates the advantages and limitations of origami robotics and the primary research objective. In this thesis, we answered the research questions by developing three robotic systems and a framework that enables high-level control and connects with multiple simulation engines.

First, a new design method was developed to make hybrid transmissions. This was achieved by combining the compactness and manufacturing method efficiency of origami robotics with the kinematic design of conventional transmissions. The resulting system answers the first research question as it is compact, mechanically capable, and can be coupled with traditional rotatory actuators to transfer and transform their motion to the end-effector efficiently. Although these transmissions serve one functionality, they can be combined to create compact multi-DoF mechanisms and robots. This last feature is the key to answering the second research question. It enables the creation of the *Haptigami* that uses the aforementioned low-profile transmission mechanisms as building blocks. This robot is a fingertip haptic device able to achieve multiple functionalities despite a low volume and weight. Finally, owing to the previous projects' technical investigations and a better understanding of the origami properties, the last robot addresses the third research question: combining compactness, multi-DoF, and mechanical capabilities into a single embodiment referred to as *F-VSA*, a flexure variable stiffness actuators. This device is a novel elastic actuator that uses the mechanical efficiency of origami as both elastic element and multi-DoF transmissions in a compact embodiment that does not require additional parts and springs. Owing to their non-conventional structures, actuation, and kinematics, it is unlikely that such systems will be compatible with standard robotic protocols. Hence, each of the four robots presented in this thesis required the development of new control algorithms and characterization methods. They necessitate the investigation of model-based and model-free control strategies to achieve their tasks. Moreover, it is challenging to develop a testing setup for measuring the mechanical capabilities, such as the force and speed, of small and compliant robots with numerous DoF. Hence, the development of novel systems and methods to characterize meso-scale devices was investigated. Finally, these novel robotic systems necessitated a high-level control interface to allow users to program and use them for multiple applications. This interface was made compatible with multiple simulation engines to enable the robots to perform tasks in a virtual environment and actuate their hardware accordingly. The aforementioned robots and their contributions are presented in detail in the following chapters:

Chapter 1: Design of low-profile compliant transmission mechanisms

In theory, origami design allows the creation of meso-scale robotic systems and mechanisms that are not affected by the miniaturization and assembly challenges of conventional mechanics. However, in contrast to the rigid approaches, robotic origami application has been limited by the complex deformation and kinematics of the compliant joints and actuation based on active materials or conventional electric motors. To generalize their application at meso-scale, a combination of the predictability of traditional rigid kinematics and the manufacturing flexibility of robotic origami is required. Here a study of conventional transmission mechanisms, including a slider-crank and cam-follower, made in quasi-2D form by selective machining and stacking multiple layers of composite material with minimal assembly is presented. The 5.3 mm thick and lightweight mechanisms transmit rotational motion to translational movements

in- and out-of-plane, owing to a compliant design powered by low-profile piezoelectric motors. Further, analytic models were developed, which were validated in terms of force and motion output using the prototypes. My contributions to this work are as follows:

- Development of new planar and compliant transmission mechanisms and actuation design for meso-scale foldable robots and machines.
- Design and modeling of quasi-2D flat slider-crank and cam-follower with in- and out-of-plane motions.
- Experimental validation of the proposed models with prototypes at unloaded and loaded conditions.

The material presented in this work has been adapted from the following publication:

[36] **Giraud, F. H.**, Zhakypov, Z., and Prof. Paik, J. (2019). Design of Low-Profile Compliant Transmission Mechanisms. In 2019 IEEE/RSJ International Conference on Intelligent Robots and Systems (IROS) (pp. 2700-2707). IEEE. DOI: 10.1109/IROS40897.2019.8967701

Chapter 2: Haptigami, a fingertip haptic interface with cutaneous force feedback

Wearable fingertip haptic devices aim to deliver somatosensory feedback for applications such as virtual reality, rehabilitation, and enhancing hardware/physical control interfaces. However, providing various types of feedback requires several DoF and high mechanical complexity, which are mechanically difficult to achieve at the meso-scale. Using compliant low-profile transmissions embedded in an origami structure and piezo-motors as actuators, a novel 3-DoF fingertip haptic device, *Haptigami*, was designed and fabricated. This under-actuated system, measuring 36 x 25 x 26 mm and weighing 13 g, can render vibrotactile and cutaneous force feedback. This proposed device was tested by creating a novel experimental protocol and robotic platform allowing quantitative characterization of mechanical capabilities. The current prototype of Haptigami produced 678 mN in compression, and 400 and 150 mN in shear for the Y and X directions, respectively. Owing to its unique origami-inspired design, Haptigami introduces a new direction for future designs of lightweight and compact wearable robots. My contributions to this work are as follows:

- *Haptigami*, the first example of using origami robotics in wearable haptics, rendering it the smallest and lightest fingertip haptic device capable of roll, pitch, compression, and vibration.
- Comprehensive modeling and closed-loop control of the kinematics of *Haptigami* that relates motor rotations (inputs) to roll, pitch, and compression (controllable outputs) of the device.

- A new experimental protocol for characterizing the force vs. displacement behaviour of the meso-scale haptic devices in their entire range of motion and all actuation modes (roll, pitch, compression, shear, and vibration).

The material presented in this work has been adapted from the following publication:

[37] **Giraud, F. H.**, Joshi, S., and Prof Paik, J. (2021). Haptigami: a fingertip haptic interface with vibrotactile and 3-DoF cutaneous force feedback. IEEE Transactions on Haptics. DOI: 10.1109/TOH.2021.3104216 ¹

Chapter 3: Flexure Variable Stiffness Actuators

The series elastic actuators (SEAs) and the variable elastic actuators (VSAs) provide shock resistance, energy storage, and greater stable force control. However, they usually require extra springs, mechanical parts, and transmissions, thereby increasing size, weight, and number of moving parts, and reducing the mechanical capabilities. In particular, this mechanical complexity is among the significant challenges in the design of wearable, scalable, and force feedback devices. In this study, flexure variable stiffness actuators (F-VSAs), which combine kinematic transmission, elasticity, and stiffness modulation via a network of folding patterns using flexure hinges, were proposed. Thus, F-VSAs allow the creation of robots benefiting from the advantages of SEAs and VSAs without hindering form-factor or mechanical efficiency. To illustrate the design strategy of F-VSAs, a four-DoF robot that provides stiffness and force output is presented. Further, an analytical model that estimates the inherent stiffness and the end-effector force output for any particular configuration of the folding pattern was proposed. Finally, the stiffness modulation and force control of the robot was implemented and found to be consistent with predictions from the model. Thus, this novel design strategy facilitates the creation of compact and scalable robots with stiffness and force output for wearable, rehabilitation, and haptic applications. My contributions to this work are as follows:

- Flexure variable stiffness actuators (F-VSAs) - A novel actuation system design that improves mechanical complexity and compactness of state-of-the-art VSAs.
- A comprehensive modeling of F-VSAs to map achievable stiffness for any configuration.
- Design, prototyping, and control of a 4-DoF F-VSA system and experimental validation of the prototype.

The material presented in this work has been adapted from the following publication:

[38] **Giraud, F. H.**, Mete, M., and Prof. Paik, J. (2022) Flexure Variable Stiffness Actuators. IEEE Advanced Intelligent System. DOI: 10.1002/aisy.202100282

¹Best poster award, Robotac workshop, IROS 2019

Chapter 4: Robot-computer interface and simulation

Every robotic system requires a control framework with their platforms, which enables users to customize and adapt the robots' control strategy for multiple tasks. This chapter proposes a general framework architecture composed of three primary parts: the hardware, high-level control interface, and simulation engine. The high-level control interface is the central part that allows communications with the other two parts. It is compatible with other external hardware and simulation engines. This architecture is *Robotic Operating System* (ROS) based and supports the development of open-source, modular codes in a standardized environment that benefit from the state-of-the-art ROS libraries. The simulation engine allows using hardware to interact with objects in a virtual environment thanks to the robots' sensors. The interactions occurring in the simulation provide data that is processed by the high-level control interface to control the hardware's actuators and provide feedback to the user. We used this architecture to design different applications for three devices: the Haptigami, F-VSA system, and an hand-grasped haptic device. We used Gazebo, a custom ROS program, and Unity as simulation engines, depending on the desired task, to demonstrate our architecture's versatility. My contributions to this work are as follows:

- An open-source ROS-based high-level-control interface architecture that connects to different hardware and simulation engines.
- Control of the hardware depending on the task and interactions occurring in the virtual environment.
- Design of applications for the Haptigami, F-VSA system, and a hand-grasped haptic device using the developed framework.

The material presented in this work has been adapted from the following publications :

[37] **Giraud, F. H.**, Joshi, S., and Prof Paik, J. (2021). Haptigami: a fingertip haptic interface with vibrotactile and 3-DoF cutaneous force feedback. *IEEE Transactions on Haptics*. DOI: 10.1109/TOH.2021.3104216

[38] **Giraud, F. H.**, Mete, M., and Prof. Paik, J. (2022) Flexure Variable Stiffness Actuators. *IEEE Advanced Intelligent System*. DOI: 10.1002/aisy.202100282

Chapter 5: Conclusion and future outlook

This chapter summarizes the achievements and findings of the previous four chapters. First, the motivation, contributions, and future works regarding the robotics systems and their framework realized during this thesis are discussed. These robots close the gaps between compactness, DoF, and mechanical capabilities. The creation of such systems is a challenging task that was addressed owing to this thesis contributions in terms of design and manufacturing, model and control strategies, and characterizations platform and experimental protocol.

Introduction

Finally, the broad impact and future work of compact origami platforms in the field of HRI is discussed.

List of publications

The research regarding the robotic systems developed in this thesis led to the following published works:

1. **Giraud, F. H.**, Zhakypov, Z., and Prof. Paik, J. (2019). Design of Low-Profile Compliant Transmission Mechanisms. In 2019 IEEE/RSJ International Conference on Intelligent Robots and Systems (IROS) (pp. 2700-2707). IEEE. DOI: 10.1109/IROS40897.2019.8967701
2. **Giraud, F. H.**, Joshi, S., and Prof Paik, J. (2021). Haptigami: a fingertip haptic interface with vibrotactile and 3-DoF cutaneous force feedback. IEEE Transactions on Haptics. DOI: 10.1109/TOH.2021.3104216
3. **Giraud, F. H.**, Mete, M., and Prof. Paik, J. (2022) Flexure Variable Stiffness Actuators. Advanced Intelligent System. DOI: 10.1002/aisy.202100282

1 Design of low-profile compliant transmission mechanisms

This chapter combines the advantages of origami robotics in terms of compactness and ease of fabrication with the mechanical capabilities of conventional mechanics. This research is a design method that enables the creation of conventional transmissions using origami's manufacturing process and flexure hinges benefits. These transmissions are low-profile and use functional material that enables out-of-plane motion. They solve both the complex design process and kinematics of transmissions with only flexure hinges. As a demonstration, this research explores the design and fabrication of low-profile slider-crank and cam-follower mechanisms using piezo-motors with a custom-designed frame and encoder as actuators. For these two systems, we developed a kinematic model helping design process and position control. Finally, we created an experimental setup to measure our transmissions' force and position and assess the validity of the kinematic model. These transmissions enable the creation of a compact system able to tune force and motion output without compromising mechanical capabilities.

1.1 Introduction

Conventional mechanisms composed of 3D rigid bodies, such as slider-cranks, cams, gears, or various arrangements of linkages, have long been used for transmitting or converting forces and motions. These existing transmission mechanisms have proved to be efficient and reliable for achieving desired motions, forces, and speeds for specific tasks in macro-scale robotics and machine design. However, their application at the meso-scale, with features of a few hundred micrometers to a few centimeters, has been limited due to the difficulty of physical miniaturization, manufacturing, and assembly of numerous tiny joints and links that require high-precision machining and laborious assembly processes. Researchers have also developed various mechanisms at the micro-scale, known as microelectromechanical systems (MEMS), with features ranging from nanometers to micrometers by replacing the rigid kinematic joints with compliant joints. This allows utilizing different material properties and layer-by-layer manufacturing processes to build active mechanisms without manual assembly. However, the resulting mechanisms generate extremely low forces and reduced motion range, making it

difficult to scale up for targeting macro- and meso-scale mechanisms design. Moreover, the clean-room manufacturing processes based on photolithographic techniques require masks that hinder flexibility and customizability of mechanism design. Therefore, developing a meso-scale transmission mechanism combining the customizability of macro-scale mechanisms and rapid manufacturing processes of MEMS is necessary.

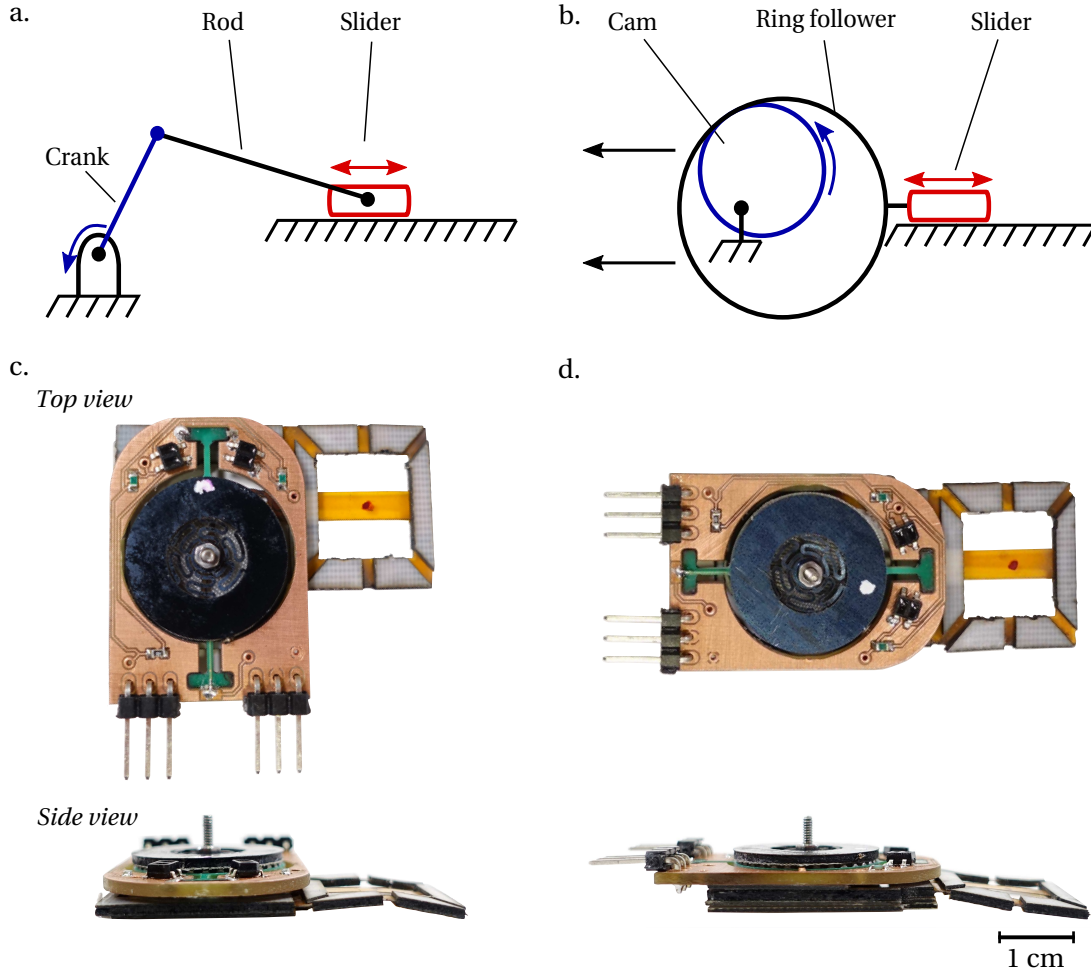


Figure 1.1: Transfer of conventional mechanisms into quasi-2D systems. a. and b. are the schematic views of slider-crank and cam-follower mechanisms. c. and d. represent their multi-layers, low-profile and compliant versions.

Recently, robotic origami, also known as Robogamis [4–6] have become an effective and versatile platform for creating meso-scale robots and machines with foldable flexure joints, planar linkages, actuators, and sensors. They allow rapid fabrication of complete robotic systems from low-profile multi-material functional layers that are laminated layer-by-layer and pop-up folded with minimal manual assembly ; known as Smart Composite Microstructures (SCM) [39]. This methodology combines the advantages of traditional mechanism design and MEMS fabrication with multi degrees-of-freedom (DoF) origami movements, enabling high customizability and mass production. Diverse origami robots have been constructed as

supports or active structures by distributing bending [20, 21, 40] or linear [10, 22, 41] smart actuators in a pattern of one-DoF folding joints [11, 15, 18, 23]. As these robots employ direct-drive approach, the actuator design limits their force and motion. Smart material-based actuators, such as shape memory alloy, generate high forces at lightweight. However, they suffer from high power consumption, low actuation bandwidth (< 1 Hz), and irreversible motion. Pneumatically-driven origami mechanisms overcome some of these challenges due to single actuation [31, 42, 43] that lacks control over the folding sequence, or actuation distributed [16, 17] to fold multi-hinged patterns with complex deformation physics. Use has also been made of origami-based transmission mechanisms actuated by conventional rotary motors using tendons to transmit rotational motion to fold the origami joints [30, 44], or actuate legged robots [27, 34, 35]. This grants the reproduction of macro-scale mechanisms at small scale with controllable and reversible motions. However, such a hybrid approach still requires a 2D to 3D manual assembly of transmission elements, bulky actuators, and specific coupling components, which are machined or 3D-printed separately. None of the solutions provide a compact transmission mechanism with tunable and controllable motion and force outputs and fabricated with minimal assembly effort.

This chapter presents novel low-profile quasi-2D transmissions with comparable functionality to conventional link-joint mechanisms for tunable actuation of robotic origami folds. We introduce new slider-crank and cam-follower mechanisms created from a multi-layer lamination process using flexible composite materials. The resulting systems convert rotational DoF to translational movements with high compliance, allowing transmission in- and out-of-plane impossible to achieve with conventional rigid mechanisms. We discuss the capability of combining the proposed scalable mechanisms into a multi-mechanism stack to embed easily diverse transmission systems with reduced numbers of actuators. We also propose a new actuation approach based on planar rotational piezoelectric motors that enable reversible, controllable, and easy integration. We illustrate the mechanism prototypes fabricated entirely in quasi-2D and assembled to 3D and their embedding into a complex 3-DoF under-actuated origami platform. We model each mechanism analytically and validate the models at no-load and loaded conditions with characterization tests. Our work addresses the challenges of mechanical transmission, actuation design, miniaturization, and the versatility of meso-scale robots and mechanisms.

1.2 Conventional Transmissions

Numerous transmission systems are present in the literature and have been used for centuries in conventional mechanics. The field of robotics makes important use of rotary motors, which have well-defined behavior and interesting features in terms of force, speed, and integration. Hence, transmissions converting the rotation of these actuators find a purpose in numerous mechanical systems and applications. This chapter focuses on the implementation of recognized and widely used transmission systems converting rotation into translation: a slider-crank and a cam-follower. This section gives an overview of their characteristics.

1.2.1 Slider-crank

Figure 1.1a. shows the schematic of a traditional slider-crank mechanism with three main parts: crank, rod, and slider. When a rotatory actuator drives the crank, the rod attached to it moves, leading to slider translation. Because the force applied to the slider is not horizontal, its displacement is usually constrained by a slot. In order to ensure a complete rotation of the crank, the Grashof's condition regarding the choice of the links' length has to be satisfied.

With the parameters of Fig. 1.2a., the equation that links the displacement x to the crank rotation angle θ can be found in [45] is,

$$x = a \cdot \cos(\theta) + b \cdot \cos(\mu) \quad (1.1)$$

with a transmission angle μ linked to θ by

$$\mu = \arcsin\left(\frac{a \cdot \sin(\theta) - c}{b}\right) \quad (1.2)$$

with, a the crank size, b the rod size and c the offset between the rotor's center and the slider displacement axis.

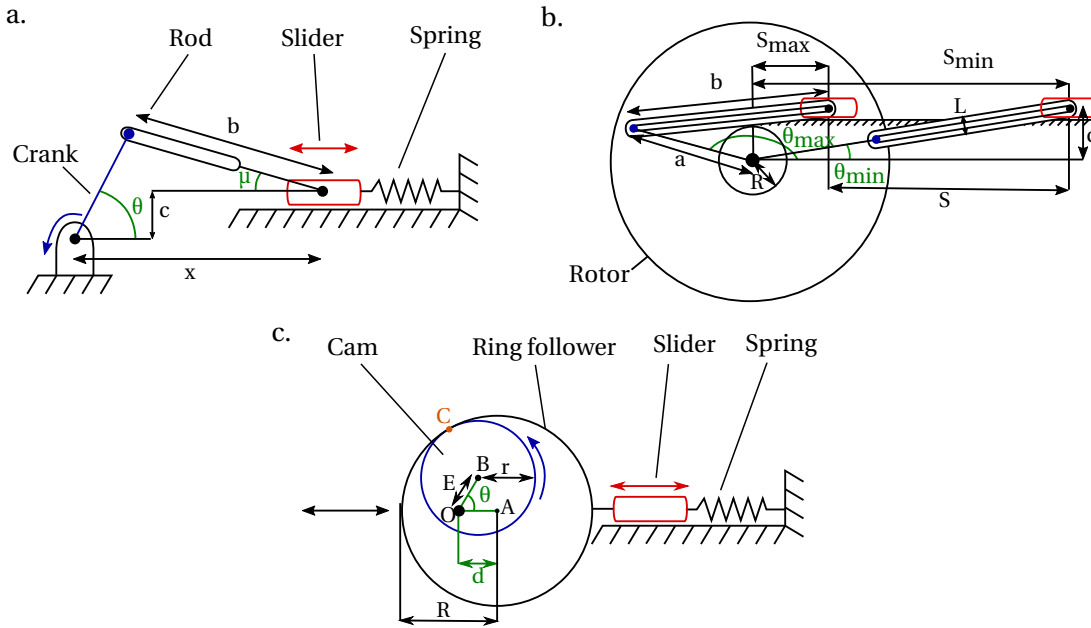


Figure 1.2: A low-profile mechanism schematic used to build kinematic models. a. Offset slider-crank. b. Represents the slider-crank mechanism's limitation in terms of position. θ_{max} is reached when the rod is in contact with the spacer and determines the maximal follower position s_{max} . θ_{min} is reached when rod and crank are parallel, which leads to the follower's minimal position s_{min} ; c. Cam-follower.

1.2.2 Cam-follower

A cam-follower mechanism transforms a rotation into a linear translation and uses the shape of the cam and follower to tune the output motion, force, and speed. The follower choice defines the design method for the cam's shape.

While several types of followers exist, the most common are simple roller or flat-surface followers. Their displacement is usually constrained to a translation by a slot, but they can also have one end attached to a pivot in the case of oscillating followers. The contact with the cam can be made at one or multiple points and should avoid friction for optimal force transmission to prevent mechanical wear.

The cam itself can vary from a simple eccentric circle to a complex non-uniform shape. Their design starts by choosing the follower motion profile adapted to the application speed and acceleration, such as a simple harmonic motion for example. Then, the follower type defines the method to find the outline's parametric equations. Several optimization methods to minimize the cam's surface, or smooth its curves to improve high acceleration performance, can be found in the literature [46].

However, all the existing work regarding slider-crank and cam-follower transmission cannot be directly translated to the 2D plane.

1.3 Design and Modelling of multi-layers low-profile transmissions

1.3.1 General design considerations

This chapter aims to design low-profile transmissions by adding compliance to conventional rigid systems to transmit planar motions to out-of-plane configurations. Therefore, their design requires selective arrangement of multi-material layers with variable compliance. This section focuses on the slider-crank and cam-follower transfer to this low-profile, multi-layers compliant mechanism. Even if these transmissions' working principles differ, they both aim to translate a slider connected to a load. To ensure movements in- and out- of plane, the slider linked to the core mechanism has to be flexible. Consequently, the mechanism design requires layers made of flexible material used as joints between structural links and compose the rod, slider, and follower of the cam to provide compliance and allow the overall structure to fold.

However, two constraints arise from the use of flexible layers:

- First, they are more fragile than rigid ones, affecting the overall solidity of the mechanism. To address this issue, we stacked flexible layers to create components with tuned robustness and stiffness, depending on the functionality.
- Second, the mechanism can not push the flexible slider, which will buckle¹ and be un-

¹Buckling: the sudden change in shape of a structural component under load.

able to move the follower. Consequently, we designed our mechanisms to be uncoupled from the rotor during this phase and added a spring to pull back the follower to its initial resting state. In our case, the spring consists of an integrated origami water-bomb pattern. Nonetheless, it could be designed or chosen externally from the mechanism, depending on the needs.

We used rigid materials for the structure's skeleton to increase its robustness, where the transmissions' flexibility is not affected.

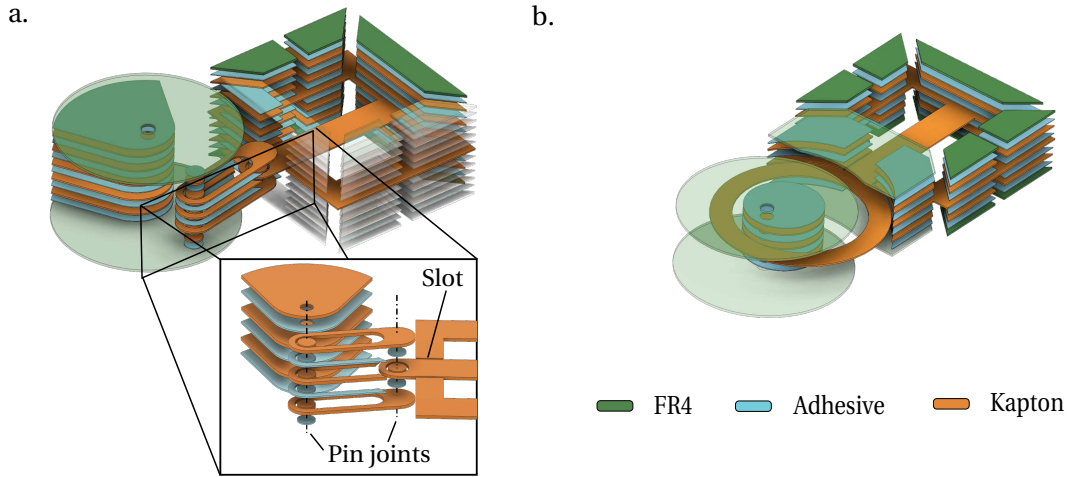


Figure 1.3: Layer-by-layer representation of a. Slider-crank and b. Cam-follower mechanisms.

1.3.2 Slider-crank

Design

The developed low-profile offset slider-crank mechanism is shown in expanded view in Fig. 1.3a. and a picture of the prototype in Fig. 1.1c. As for a conventional slider-crank, this system has a rod, two pivot joints, and a slider. The crank is replaced by a larger diameter rotor, including a pin connected to the rod. When activated, the rotor will drive this pin, pulling the rod and hence translating the slider. In order to decouple translation and rotor rotation during the pushing phase, a slot within the rod allows the rotor pin to slide without applying forces on the slider. Therefore, the contact between the rotor's pin and the end of the rod determines the mechanism's phase. In the forward phase, the follower is led by the rotor, while in the other phase, the follower and rod motions are driven by the flexure hinges' spring. As in conventional mechanisms, the slider's motion is constrained to be linear due to the slot created in the internal layers. A gap made within the rotor, allows the rod to slide inside it when the mechanism is active. The gap is formed from two stacks of layers, one with a circular shape acting as a pin connected to the rod and the other having an area large enough to support the structure, while allowing maximum slider displacement into the rotor.

The general design is composed of layers of different functionality and layout. The two outer layers in green in Fig. 1.3a are rigid and define the mechanism's overall structure. They also provide a solid surface for the piezo-motor to interact with. The inside layers in orange are functional and serve either as spacers to create gaps to minimize friction, or as mechanical elements such as a rod, pin or slider. Adhesive, represented in blue in Fig 1.3a is placed between the functional layers and has a design adapted to its location in the stack to prevent moving parts being glued to structural elements during the manufacturing process.

Model

This section presents the equations used to design a slider-crank with stroke, motion, and dimensions adapted to a targeted application. Well-known conventional slider-crank kinematic equations given in the previous section are still verified in this low-profile design. Nonetheless, the rotor's spacer adds a limitation in terms of maximal stroke. In this section, we analyze this constraint to determine the maximal displacement of the mechanisms. The schematics used to build this model are represented in Figs. 1.2a and b.

As illustrated in Fig. 1.3a, the rotor has a gap inside that allows the crank and slider to move. This space is created by spacers with a radius R , placed in the rotor's center and preventing the rod and slider going through the spacer area. Therefore, Grashof's condition setting the requirement to ensure full rotation of a four-bar linkage system cannot be satisfied. Because of this limitation, the maximum rotation angle is set by one of these two independent conditions: 1) Transmission angle μ (Fig. 1.2a or 2) Spacer radius R (Fig. 1.2b).

1. Transmission angle μ :

The force component on the slider axis should never reach 0, which means that the transmission angle μ has to satisfy:

$$-\frac{\pi}{2} < \mu < \frac{\pi}{2} \quad (1.3)$$

From a geometric consideration, the upper boundary condition is satisfied if,

$$b > a - c \quad (1.4)$$

μ is given by (1.2) and therefore (1.3) becomes:

$$\arcsin\left(\frac{-b+c}{a}\right) < \theta < \pi - \arcsin\left(\frac{-b+c}{a}\right) \quad (1.5)$$

which gives us the boundaries of θ for a chosen a , b and c .

2. Spacer radius R :

As illustrated in Figure 1.2b., the slider's maximal position is limited by the rod's width L and the spacer's radius R . Assuming that $(0,0)$ are the rotor's center coordinates, the line

passing through the two ends of the rod has this equation:

$$(a \cdot \sin(\theta) - c) \cdot x - (b \cdot \cos(\mu)) \cdot y + a \cdot \cos(\theta) \cdot c - a \cdot \sin(\theta) \cdot [a \cdot \cos(\theta) + b \cdot \cos(\mu)] = 0.$$

D is given by the line to point distance relation:

$$D = (|a \cdot \cos(\theta) \cdot c - \frac{a \cdot \sin(\theta) \cdot [a \cdot \cos(\theta) + b \cdot \cos(\mu)]}{(\sqrt{(a \cdot \sin(\theta) - c)^2 + (b \cdot \cos(\mu))^2})}|) \quad (1.6)$$

After simplification, (1.6) becomes,

$$D = |a \cdot \sin(\mu + \theta)| \quad (1.7)$$

From Fig.1.2b, the maximal position is given when,

$$D = R + \frac{L}{2} \quad (1.8)$$

By equating (1.7) and (1.8), θ_{max} can be determined given all the other parameters are defined by the design.

The final maximal position that can be reached is the smallest θ_{max} between (1) and (2).

Regarding the minimal position s_{min} ; it is reached when the rod and crank are parallel as shown in 1.2b. The relation between s_{min} and θ_{min} is found using simple trigonometry:

$$(a + b) \cdot \cos(\theta_{min}) = s_{min} \quad (1.9)$$

The stroke of this mechanism is dependant on θ limitations and is the distance s between the maximum displacement s_{max} for θ_{max} and the low position s_{min} . Therefore the stroke s , given by the design parameters of this system a, b, c, R, L is:

$$s = s_{max} - s_{min} \quad (1.10)$$

$$\Rightarrow s = a \cdot \cos(\theta_{max}) + b \cdot \cos(\arcsin(\frac{a \cdot \sin(\theta_{max}) - c}{b})) - (a + b) \cdot \cos(\theta_{min}) \quad (1.11)$$

1.3.3 Cam-follower

Design

An expanded view and a prototype picture of the low profile cam-follower mechanism developed in this research are illustrated in Figs. 1.3b and 1.1d, respectively. The system's working

principle is similar to a conventional cam-follower. When activated, the cam rotation pushes the surface of a ring-shaped follower, pulling a flexible slider linked to the load, leading to its translation. During the return phase, the constant of the chosen spring decides whether or not there is contact between the cam and follower and, therefore, whether rotor rotation and follower translation are dependent. A slot in the structural layers constrains the slider's motion to be linear. When activated, slider and follower can move inside the rotor due to the gap created by the layers comprising the cam itself.

The thinness of the inside material, and hence flexibility, makes the follower have a curved shape. There is indeed important friction between cam and follower, leading to unwanted tangential forces. In the case where the follower has a flat surface for example, it would be driven to the side, leading to slider torsion and consequently mechanical failure. This design uses a ring as follower, which prevents the tangential motion by creating a side contact between the cam and follower during rotation. Hence, although the ring shape increases friction, the slider's displacement is kept linear, ensuring a properly working mechanism. In order to simplify the model, the cam and ring design are two eccentric circles.

Simpler than the slider-crank, the cam-follower needs less functional layers. Slider, flat-follower, and cam layer can be part of the same layer or stack of layers. Spacers minimizing friction with the two structural rigid layers are placed on the outside. The adhesive is placed between every layer with a specific design depending on the position in the stack to avoid gluing together moving parts.

Model

The mechanism design is shown in figure 1.2c and consists of two eccentric circles. The ring, with a radius R , moves linearly when pushed by the cam of radius r . This section establishes the mathematical equation linking the displacement d to the cam rotation angle θ .

For every θ , because of our circular design, the ring's center A , cam center B and contact point C between cam and ring are aligned. Therefore,

$$\overrightarrow{AC} = \overrightarrow{AB} + \overrightarrow{BC} \quad (1.12)$$

equal to,

$$\|\overrightarrow{AC}\| = \|\overrightarrow{AB}\| + \|\overrightarrow{BC}\| \quad (1.13)$$

Knowing that $\|\overrightarrow{AC}\| = R$ and $\|\overrightarrow{BC}\| = r$ only $\|\overrightarrow{AB}\|$ needs to be found to use 1.13. From Fig. 1.2 we can see that,

$$\overrightarrow{AB} = \overrightarrow{AO} + \overrightarrow{OB} \quad (1.14)$$

$$\Rightarrow \overrightarrow{AB} = \begin{bmatrix} -d \\ 0 \end{bmatrix} + \begin{bmatrix} E \cdot \cos(\theta) \\ E \cdot \sin(\theta) \end{bmatrix} \quad (1.15)$$

$$\Rightarrow \overrightarrow{AB} = \begin{bmatrix} -d + E \cdot \cos(\theta) \\ E \cdot \sin(\theta) \end{bmatrix} \quad (1.16)$$

Hence,

$$\|\overrightarrow{AB}\| = \sqrt{(-d + E \cdot \cos(\theta))^2 + (E \cdot \sin(\theta))^2} \quad (1.17)$$

By inserting (1.17) into (1.13) we get a second order polynomial equation of unknown d :

$$(R - r)^2 = d^2 - 2 \cdot E \cdot d \cdot \cos(\theta) + E^2 \quad (1.18)$$

having two roots that correspond to the symmetric motion relative to the ring's center:

$$d(\theta) = -E \cdot \cos(\theta) \pm \sqrt{(E^2 \cdot \cos(\theta)^2 - E^2 + R^2 - 2 \cdot r \cdot R + r^2)} \quad (1.19)$$

One design constraint is given by (1.19) where $d(\theta)$ exists only if $E^2 \cdot \cos(\theta)^2 - E^2 + R^2 - 2 \cdot r \cdot R + r^2 \geq 0$. This condition is verified if,

$$R - r \geq E \cdot \sin(\theta_{max}) \quad (1.20)$$

with θ_{max} the maximum rotation angle for a specific application. Therefore, the condition to satisfy a full rotation of the cam inside the ring is given by,

$$R - r > E \quad (1.21)$$

1.4 Manufacturing process of multi-layer low-profile transmission mechanisms

1.4.1 Mechanisms

The systems presented in this chapter are created using a layer-by-layer manufacturing process such as the one presented in [21]. It consists of stacking and gluing functional layers of different materials using *Polymelt 701* sheets as adhesive and a heat press. For this project, the choice of materials was reduced to *Kapton*, *FR4* and adhesive. $50\mu\text{m}$ -thick *Kapton* sheets were used because of their flexibility and high mechanical resistance to strain and sandwiched between two 0.3 mm-thick layers of *FR4*. These materials are temperature resistant and thus suit for heat press.

The manufacturing process is identical for the two mechanisms and presented in Fig. 1.4. First, the different adhesive, *FR4* and *Kapton* layers are cut by laser, in our case with a *Trotec Speedy 400*. The layered design has an outline with holes to make manipulation and alignment easier. Problems arise from the *Polymelt 701*, as it is very thin, making bridges and floating parts prone to breaking and extremely difficult to align when removed from the protective layer. We, therefore, adjusted the laser parameters to cut through the adhesive without affecting the

1.4 Manufacturing process of multi-layer low-profile transmission mechanisms

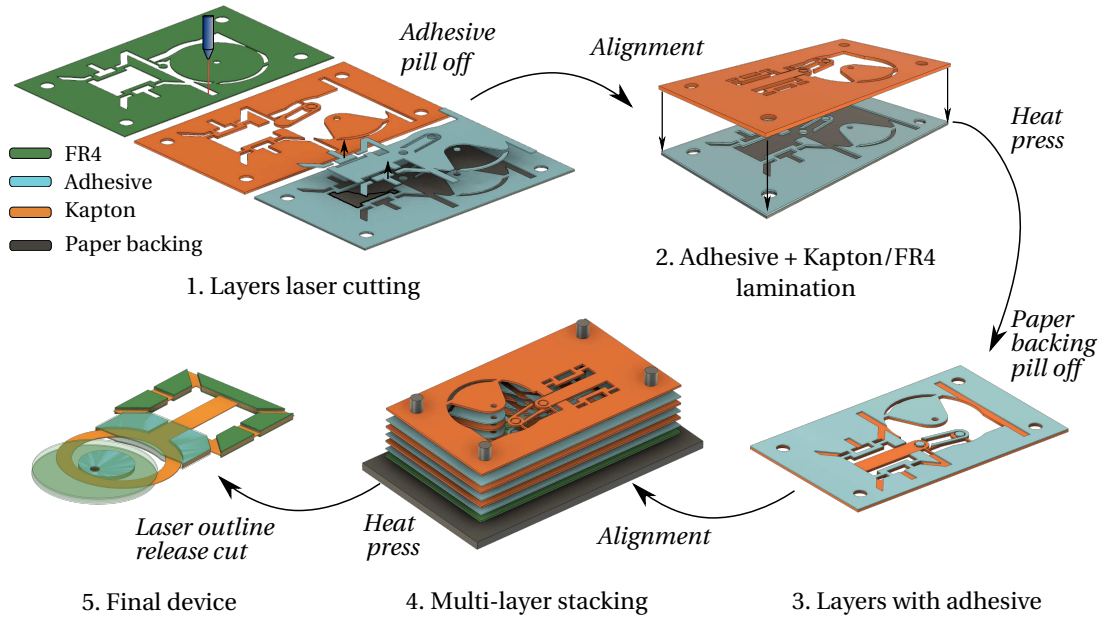


Figure 1.4: Manufacturing process used for the mechanisms described in this chapter. The different layers are laser cut, and corresponding functional and adhesive layers are grouped in pairs. After alignment and heat-press, the adhesive is coated onto the functional layers, and the protective sheets are peeled off. Then, using an alignment platform and heat-press to re-melt the adhesive, all layers are stacked and glued together. Finally, the outline used for the alignment is removed by laser cutting, and the resulting mechanism is fully functional.

protective layers, allowing peeling off the useless parts while keeping the ones of interest rigid enough to be manipulated. The resulting adhesives are fixed onto their corresponding *FR4* or *Kapton* layer using a heat press (90 Kg at 110°C for 10 min). After a cooling-down period, the protective layers are peeled off, leaving the *FR4* or *Kapton* coated with adhesive. These layers are then aligned, and heat pressed using the same parameters to give the final stack. After a second cooling-off period, the resulting layers are placed again into the laser, where outlines and bridges are cut out to give the final mechanism.

Regarding the heat-press, a uniform pressure is applied onto the stack of layers. This information needs to be considered in the design phase because of the layers' flexibility, making the small central part collapse due to gravity. This would result in a non-flat surface and non-uniform pressure, leading to bad layer adhesion in certain parts of the design. For that reason, extra parts, either permanent or temporary, were introduced to support the collapsible parts of the surrounding layers. These support materials are extra pins to support pivots or bridges designed for places where the device functions would not be affected, aim to put uniform tension over all the surface, and avoid moving any floating parts. These additional components become useless after manufacture and fall off at the final laser-cutting stage, producing the functional mechanism.

The CAD layers design of the slider-crank and cam-follower mechanisms can be found in appendix A.1 and A.2, respectively. In order to reduce material waste and fasten the laser cutting, adhesive lamination, and design iterations, our design strategy aims at reducing the number of layers to a minimum. The resulting mechanisms without the actuator have a thickness of 1.25 mm.

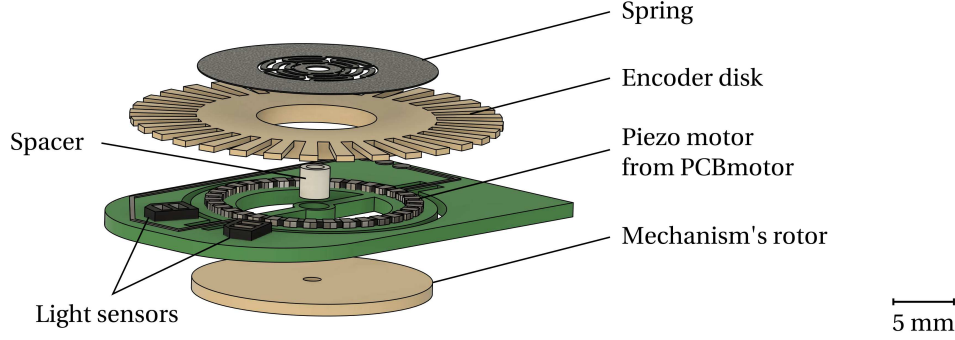


Figure 1.5: PCBmotor assembly and sensors integration.

1.4.2 Actuation

Our mechanisms are compatible with rotary actuators, such as DC motors. However, electromagnetic actuation torque output is strongly dependent on their size. Their application with low-profile origami structures is limited as adding extra coils or gearboxes will impact the overall system compactness. Instead, we choose *PCBmotors* [47, 48] as actuation method that is controllable, bi-directional, and provide decent force and speed for multiple application without the need for extra parts. In addition, they are made of thin piezo elements with high force density and can be produced using pick-and-place techniques directly on the PCB. Hence, they are easy to integrate into planar devices and thus seem particularly adapted to actuate Robogamis.

The *PCBmotors* we used a 20 mm stator radius in order to minimize the final size of the transmission. With this dimension, the manufacturer ensures a free speed of 1.6 rev/s, 8 Nmm stall torque, and maximum output power of 40 mW.

We fixed the *PCBmotors* onto the rotor already integrated into the mechanisms, driving them to translate followers. For better integration, we designed a compact PCB embedding motor, sensors, and a central bearing to keep the rotation axis in the middle. A second rotor fixed onto the other side of the *PCBmotors* contains a spring as advised by [48] and teeth, leading to variations in light during the rotation. Consequently, embedded sensors can detect the light modulation and determine the rotation angle, speed, and direction with a comparator and low pass filter. A spacer is used to mechanically connect the two rotors while ensuring a gap big enough to avoid blocking the motor's rotation. The overall system integrating sensors and actuation is presented by Fig. 1.5.

Equipped with *PCBmotors*, our mechanisms have a thickness of 5.5 mm for a weight of 5.74 g for the slider-crank and 6.29 g for the cam-follower.

1.5 Experiments and characterization

To assess the mechanisms' capabilities in terms of motion and force, we ran two experiments at no load and blocked conditions, respectively.

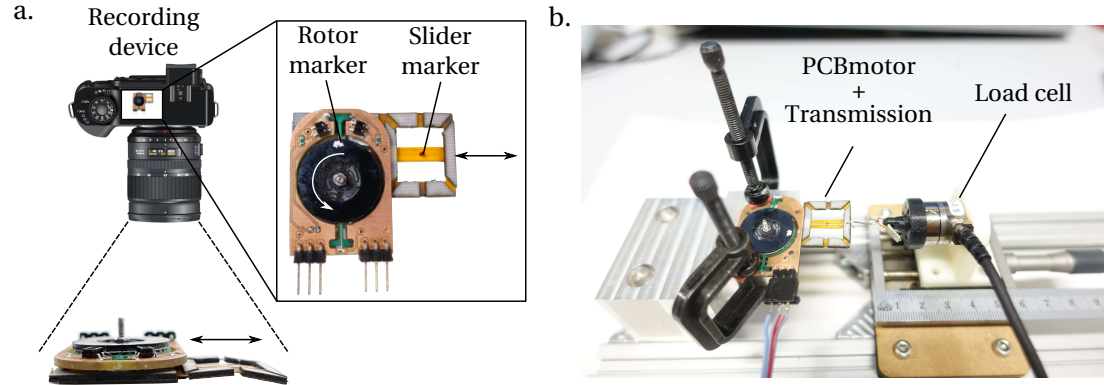


Figure 1.6: Experimental setup used to measure the transmissions' force and motion. a. To characterize the motion profile, a camera is used to record the displacement of two markers, placed on the rotor and slider respectively. b. The force of the complete system is measured for different strokes by moving the load cell. Ruler is shown in cm scale.

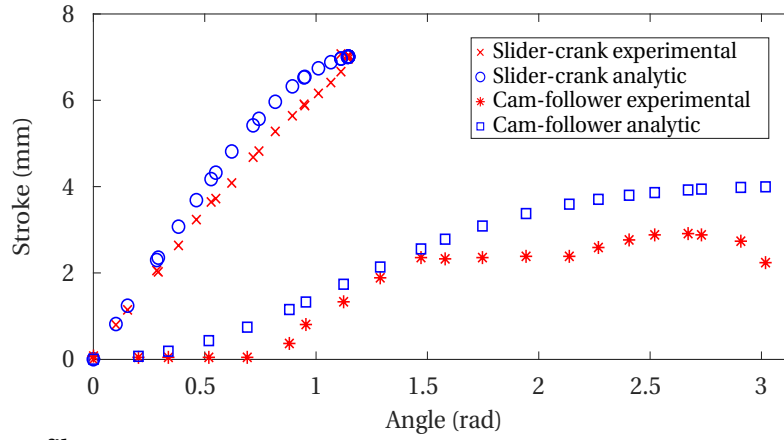
1.5.1 Kinematics

This experiment aims to characterize the follower displacement of the mechanisms relative to the motor rotation angle. We use the results to validate the model developed in the design section.

We fixed the two prototypes onto a horizontal surface, unloaded, with a camera positioned above. Each had the follower and rotor equipped with a marker. Once activated, the camera recorded the movement of the whole system, and a tracker software extracted the follower displacement and rotor rotation angle. The experimental setup is illustrated in Fig. 1.6a.

The motion profiles of the two mechanisms are shown in Fig. 1.7a. Only the forward phase is considered because the return phase is uncoupled from the rotor, meaning that there is no relationship between the angle and displacement. Although both mechanisms have an experimental trend similar to the models, the differences between theory and experiment are nonetheless more important for the cam-follower. This can be explained by the flexibility of *Kapton*, used to make the transmission's internal ring. Indeed, the latter could be deformed by the flexure hinges' spring force, leading to the 1mm difference in the maximal displacement. Friction between the cam and ring also makes achieving a smooth stroke rise difficult.

a. Motion profile



b. Force profile

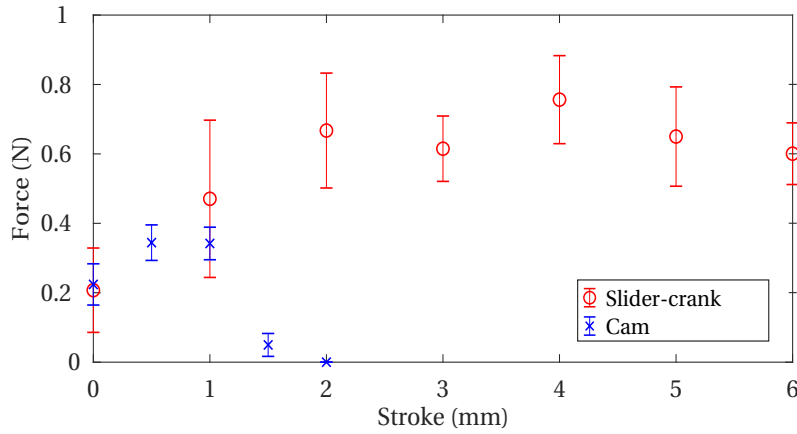


Figure 1.7: Experimental results. a. shows the motion profile: comparison of the stroke, function of the angle, between experimental data and models for unloaded slider-crank and cam-follower transmissions. b. shows the force profile: measure of the linear force at different strokes for the mechanisms.

1.5.2 Pulling force

We characterized the linear force generated by the *PCBmotor*-actuated slider-crank and cam-follower. A picture of the experimental setup is given in Fig. 1.6 b. We fixed the prototypes onto a test bench with their followers linked to a load cell. First, we set the transmission to its initial position corresponding to the maximum extension of the follower. After turning on the *PCBmotor*, we recorded the linear force of the mechanisms in this position. The follower is then moved by steps of 1 mm for the slider-crank and 0.5 mm for the cam and the force measured at each step. We conducted this experiment three times to produce a measurement error estimation. The results are shown in Fig. 1.7b.

1.6 Discussion and conclusion

This chapter presents the design and models of two planar and compliant transmission mechanisms at meso-scale, a slider-crank, and cam-follower. Built using multiple layers of flexible and rigid composite materials, the presented actuator-link-joint mechanisms provide novel transmission solutions for self-folding robotic origami structures. We also proposed a new compact actuation method based on flat piezoelectric motors that enable bidirectional rotation with high torque. We described working principles and proposed a generalized design schema for the mechanisms by establishing parameter-based mathematical models to facilitate customized usage. We experimentally characterized the prototype designs and verified their analytic models. The developed slider-crank and cam-follower mechanism designs generate an average pulling force of 0.76 N and 0.35 N with a maximum stroke of 7 mm and 3 mm, respectively.

Future work requires addressing the several limitations of the proposed mechanisms. Currently, the pin joints lack lubrication to reduce friction losses. The clearances require further optimization to avoid friction and stoppage of the sliding elements to ensure closer behavior to the mathematical models. The flexible components undergo deformation and are fragile, therefore requiring more investigation into the material properties and geometry. We also aim to implement a design method to adapt various mechanisms in origami, such as four or six-bar planar linkages.

2 Haptigami: a fingertip haptic interface with cutaneous force feedback

This chapter demonstrates the benefit of origami techniques in creating a compact multi-DoF fingertip haptic device, called *Haptigami*, able to render vibrotactile and 3-DoF force feedbacks. It uses the low-profile compliant transmissions presented in the previous chapter combined in a complex and under-actuated structure using an assembly-free manufacturing process. This research presents the design principle and manufacturing method, including motors and encoders, used to achieve the *Haptigami*. We developed a model compatible with internal folded compliant transmission mechanism and flexure hinges to control this device and created an experimental setup and protocol to assess its precision. To estimate the *Haptigami*'s capabilities in force, we created a five-DoF experimental platform able to measure the end-effector's force and torque in all its workspace. The results show that this device is compatible with the human bandwidth in terms of force and speed. This robot illustrates that intelligent design with alternative manufacturing and actuation method can create currently the most compact and lightweight robot for this number of functionalities.

2.1 Introduction

Somatosensory feedback includes properties such as compliance, texture, pressure, movement, and temperature, fundamental for perceiving our surroundings. The field of Haptics aims to better understand this type of feedback to recreate these sensations to the user artificially. This has led to numerous advances in Human-Machine Interactions (HMI) [49], rehabilitation [50, 51], robotic control [52], and exploration of virtual world [53]. In particular, there has been a flourishing interest in haptic devices for the fingertips, due to their high sensitivity and importance in manipulation. Existing fingertip haptic devices have a wide range of designs depending on the number of degrees of freedom (DoF), type of haptic feedback, and wearability. While bench-top grounded devices can typically offer more modalities, there are additional benefits to wearable devices as they allow to extend their functionalities to “out-of-the-lab” environments and, therefore, everyday life.

Pacchierotti et al. [54] conducted a concise review of current wearable haptic devices. While

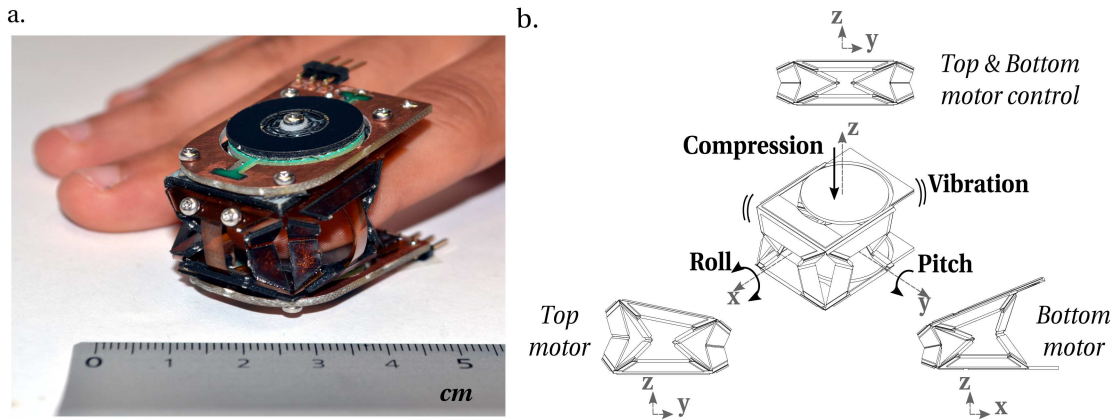


Figure 2.1: Haptigami on finger and degrees of freedom presentation. a. pictured on the user's fingertip; overall dimensions: 36 x 25 x 26 mm and 13 g. b. Haptigami renders vibrotactile and 3-DoF cutaneous feedback.

a large number of devices only produce vibrotactile feedback [54–56], many systems provide 3-DoF cutaneous feedback, including compression, roll and pitch motions, via a parallel mechanism that manipulates a small platform in contact with the fingertip [57–62]. One such device has additional mechanisms that provide haptic feedback to the entire finger [63]. Young et al. [64] presented a 6-DoF device (three positions and orientations), while Gabardi et al. [65] developed a 3-DoF device with a voice-coil that can provide vibrotactile feedback. However, as most of these devices are made using conventional mechanisms consisting of DC motors, linkages, and joints, the additional DoF are at the cost of increased weight, size, and design complexity. This trade-off in the design of such devices has been summarized well in a recent review paper by Culbertson et al. [66]: "Can we enable consumer haptic devices by decreasing cost, size and weight, and power requirements, potentially via the use of novel actuators and smart materials?". One such example is the SPA-skin by Sonar et al. [56], which embeds actuation and sensing into soft, hyper-elastic materials providing force tunable vibrotactile feedback up to 100 Hz with a device of only 1 mm thick. However, stretchable materials hinder the number of DoF, preventing applications with more diverse types of haptic feedback. While designing compact devices capable of producing multiple actuation modes is one challenge, understanding their mechanical behavior is also necessary. However, most papers assess the capabilities of their devices using user studies only, which shows the effectiveness in delivering the desired feedback [66]. Only a few research studies characterize the mechanical force output of their device, albeit in a very limited range of motion [63, 67]. Therefore, although actuation levels are controllable, it is difficult to estimate how much force the user actually feels. Thus, in addition to design innovations for reducing bulk, there is a need to create a link between the multidimensional force output and perceived sensation by the user to establish models and improve the design and development of future haptic devices.

Recently, researchers in robotics have started exploring a new origami-inspired design approach, which combines flexure mechanisms with unconventional actuators using 2D

layer-by-layer manufacturing techniques to create compact, scalable, and highly customizable robots, a.k.a Robogami [4–6, 12, 21, 39, 68]. These properties make Robogami a viable option for developing fingertip haptic devices. However, Robogami cannot be directly implemented for wearable Haptics in its current form. For instance, actuation methods in Robogami mostly include shape memory alloys [12] or pneumatic pouch motors, which suffer from limitations in terms of precise control, reversible motion, and bandwidth. Mintchev et al. [33], have addressed these using DC motors to create a haptic joystick, but at the cost of increased bulk and reduced wearability. In addition to the motors themselves, this increased bulk is also due to the mechanisms required for transmitting force and displacements. We have addressed this challenge in our previous work [69] by designing low-profile slider-crank, and cam-follower transmissions, powered using flat piezo-motors [47, 48]. These mechanisms, measuring only 4.75 mm thick with the motor and transmissions, are compliant such that they can transfer forces out of plane.

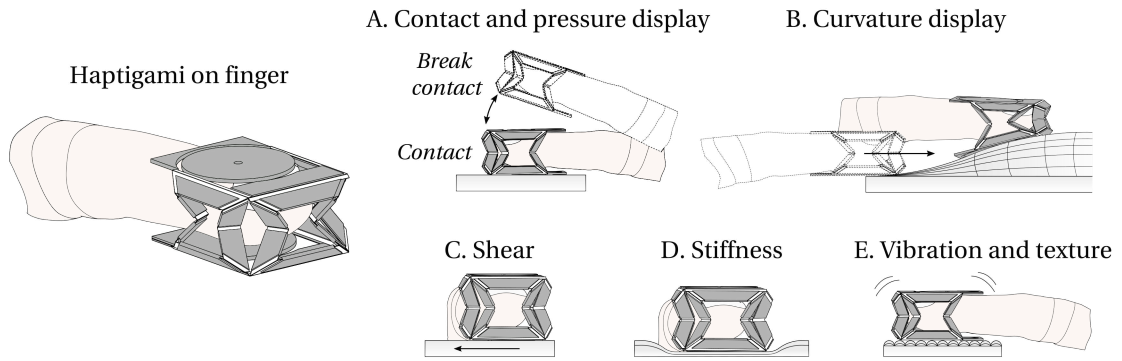


Figure 2.2: Located at the fingertip, Haptigami is mechanically capable of rendering five types of cutaneous stimuli. A. display contact and pressure, B. curvature, C. shear force, D. stiffness, and E. vibrotactile feedback.

In this chapter, for the first time, we integrate this concept into a novel, compact fingertip haptic device called *Haptigami* (Fig. 2.1a), capable of delivering vibrotactile and 3-DoF cutaneous feedback. Our system benefits from two low-profile, high-force density piezo-motors connected to low-profile slider-crank mechanisms, all integrated into an Origami-inspired base structure. Haptigami consists of four such mechanisms, arranged, stacked, motorized, and finally assembled into the final 3D structure. The resulting device is the smallest (36 x 25 x 26 mm) and most lightweight (13 g) fingertip haptic device compared to devices providing similar types of feedback. To quantitatively assess the mechanical capabilities of Haptigami, we developed a novel experimental protocol and a 5-DoF robotic platform to characterize the force output in its full range of motion. Contrary to the commonly used user surveys, this method allows to measure mechanical capabilities of meso-scale systems objectively and can be readily implemented with most other fingertip haptic devices. This chapter is a step towards a new paradigm in designing and fabricating compact haptic devices capable of providing multiple modes of somatosensory feedback to the user.

2.2 Haptic feedback of wearable fingertip devices

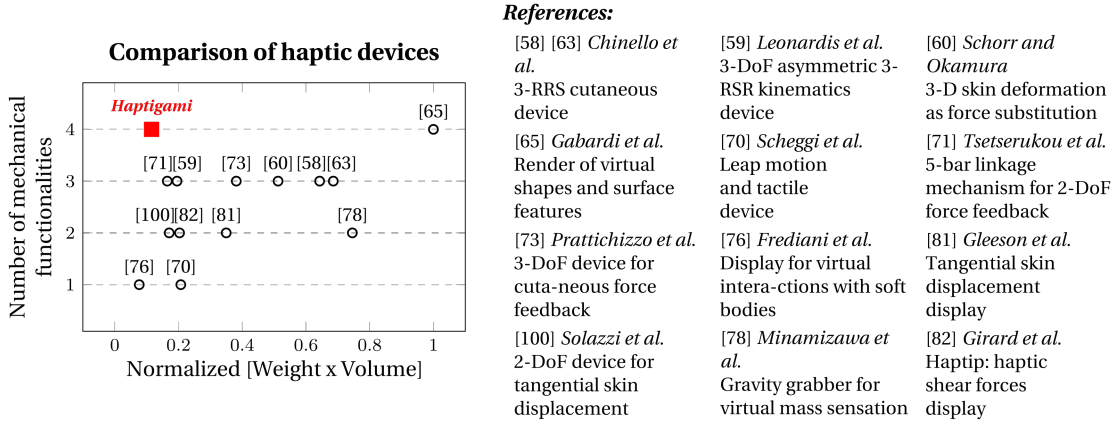


Figure 2.3: Comparison of Haptigami with state-of-the-art haptic devices in terms of number of mechanical functionalities and wearability. The latter is defined here as normalized Weight x Volume.

A device capable of rendering several types of interaction enhances the immersive experience in a virtual world, offering multiple modalities such as size, shape, rigidity, and texture to perceive its surroundings. Our objective was to develop a compact and lightweight device that can achieve five different types of haptic feedback: *A. contact and pressure display*, *B. curvature display*, *C. shear forces*, *D. stiffness*, and *E. vibration and texture* (Fig. 2.2). From a kinematic point of view, each type of feedback can be achieved with a single or a combination of six mechanical functionalities of the device, which include linear motion in the X and Y direction, compression, pitch, roll, and vibration; explained as follows:

A. Contact display: This kind of feedback allows making and breaking of contact with the user, with control on the contact location. The former requires compression, whereas the latter also needs lateral displacement to simulate contact location, requiring between one and three mechanical functionalities. To achieve this, some existing devices have used moving platforms in contact with the fingertip [58–60, 63–65, 70–73], pin arrays [74, 75], soft inflatable systems [76, 77] or a belt underneath the finger [78, 79]. Among these, [58–60, 63–65, 71, 72, 74, 75] can control the location of the contact-point using additional DoF, but at the cost of increased bulkiness.

B. Curvature display: This display aims for users to feel the curvature change of a surface, allowing exploration and shape perception of objects. To attain this effect, existing devices orient the pitch and roll of the platform in contact with the fingertip [58, 63–65, 72, 73, 80]. Similarly, [74, 75] used the compression from a pin array individually controlled in height to create a curved surface. Therefore, this feedback requires at least two mechanical functionalities.

C. Shear forces: This type of feedback conveys information about the shear forces acting on

the fingertip while it interacts with its surroundings [66]. Shear forces can also simulate the weight of an object grasped by the user [78]. This cutaneous stimulus requires a structure able to render lateral displacement and hence between one and two mechanical functionalities. Some parallel mechanisms use a tactor, which moves in a plane [72, 81, 82], or pulls a flexible material [78, 79] underneath the finger to produce this effect.

D. Stiffness: Stiffness sensation comes from the material mechanical reaction to a deformation induced by the user by application of force. Traditionally, such haptic feedback uses externally grounded devices that apply a net external force on the finger [83]. However, authors of [60] showed using a user survey that a normal skin deformation device worn on the fingertips can also render this sensation. By extending this principle, several devices with normal displacement or force modulation of the element in contact with the fingertip [58–60, 63–65, 71, 73] and soft inflatable actuators [76] are capable of this type of feedback using one to three mechanical functionalities.

E. Vibration and Texture: Vibrotactile feedback is among the most widely studied haptic feedback. By controlling the vibration based on the movement, it is possible to produce sensations of texture [84]. Vibrotactile feedback often provides notification with small and lightweight actuators [85–87]. Some studies [65, 75], couple vibrotactile to contact and curvature displays to form perceptual cues, simulating different materials and textures. Hence this requires one to three mechanical functionalities depending if the vibration is coupled with a lateral displacement.

The effectiveness of wearable haptic interfaces is affected by several factors [54] that include speed, force, workspace, size, weight and impairment. A high number of mechanical functionalities is often directly proportional to the overall size and weight of a device due to the added motors and transmissions. A larger device reduces user's dexterity and limits multi-finger tasks. In addition, a heavier device leads to fatigue and interferes with the haptic force feedback. To visualize this, we made a comparison table of the current state-of-the-art haptic devices in Fig. 2.3. The X-axis represents the device's bulkiness, using a metric defined as the normalized product of weight and volume. The Y-axis is the number of mechanical functionalities a device can achieve (pins arrays rely on a different principle to generate haptic feedback, we did not include them in this graph). We see from the figure that there is a clear trend towards increasing bulk with the number of mechanical functionalities. This suggests that in existing devices, more mechanical functionalities often result in a bulkier and, therefore, less wearable device.

Here, we present *Haptigami*, a scalable and lightweight haptic platform that benefits from multi-material 2D fabrication methods for compliant, low-profile actuation. It consists of an origami-inspired parallel mechanism structure powered by piezo-motors and embedded slider-crank transmissions, which can produce vibrations and move in 5 DoF by virtue of its under-actuated design. However, as the current design is unable to uncouple shear from pitch and roll displacement, it can effectively provide four functionalities: pitch, roll, compression,

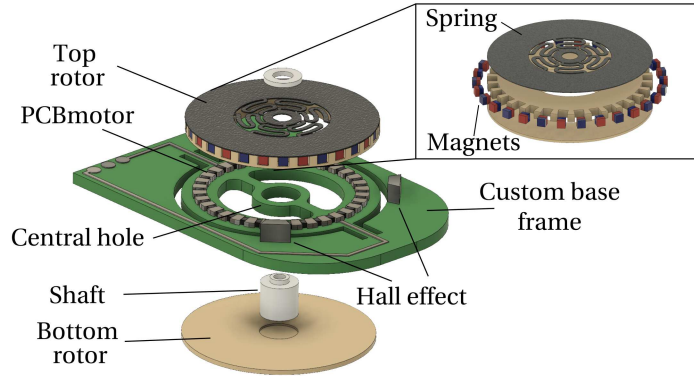


Figure 2.4: Fully integrated actuator with *PCBmotors* implemented on a custom PCB. Hall-effect sensors read the top rotor's magnets alternated polarity to control rotation angle and direction. A spacer glued onto the bottom rotor allows maintaining the two rotors in the center and synchronizing their rotation. As this is a friction-based actuator, a flat spring enables keeping a constant contact force between the rotors and stators.

and vibration. By providing contact and stiffness display via compression, shear and curvature display via roll and pitch, and texture via vibration, the Haptigami is mechanically capable of producing all cutaneous stimuli described in Fig. 2.2. At the same time, its novel and low-profile design makes it relatively compact compared to existing devices. Fig. 2.3 shows Haptigami appearing as an outlier, combining high number of mechanical functionalities with among the smallest normalized weight x volume.

2.3 Design and fabrication of an origami-inspired haptic platform with integrated transmissions

The unique design of Haptigami allows achieving a higher number of functionalities without compromising size and weight. This section describes Haptigami working principle and design of its three major components: piezo-motors, embedded slider-crank transmission, and an origami-inspired base structure.

2.3.1 Actuation and closed-loop control of the piezo-motors

For actuation, we use piezo-motors stator manufactured by *PCBmotor* [48] with a custom frame, a rotor, and a sensing system. The piezo-motor consists of a stator in the form of a PCB and is composed of piezo-crystals arranged in a circle on its two faces. We attached two rotors with flat circular faces, above and below the stator, held together by a spring-loaded shaft. The piezo-motor generates a traveling wave along the crystals, which drives the rotor via friction. It is low-profile with a high-force density, making it suitable for actuating Robogamis. We use a piezo-motor of 20 mm diameter for Haptigami. As per the *PCBmotors* datasheet, it provides a free speed of 96 rev/s, 8 Nmm stall torque, and a maximum output power of 40 mW.

2.3 Design and fabrication of an origami-inspired haptic platform with integrated transmissions

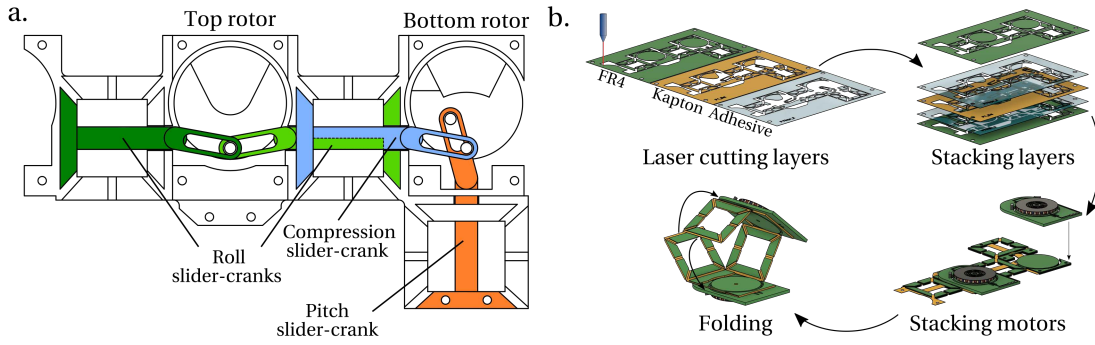


Figure 2.5: Haptigami's mechanism and fabrication. a. Internal structure composed of four low-profile slider-crank mechanisms connected to the three waterbomb patterned sides (two slider-cranks control the same side, allowing compression). Each motor can actuate two independent transmissions and select the one to drive with its sense of rotation. b. Manufacturing process: after laser cutting the Kapton, FR4 fibre-glass, and Polymelt layers, we aligned them and fixed them together by heat pressing. Then we mounted the actuators on top of the rotors already created as the layer stack. Finally, the folding joints allow folding this 2D structure into the 3D device.

We cut out the stator's circular ring from the 20 mm PCBmotor, containing the piezo crystals, represented in white in Fig. 2.4, and placed it on a custom-made base frame via bridges. The base frame also has a central hole to support the shaft connecting the top and bottom rotors. We fixed the bottom rotor rigidly to the shaft, and a customized low-profile spring fabricated from a 0.1 mm steel sheet by laser machining, connected the top rotor. The spring tension maintains an optimal contact force between the stator and rotors, critical for this friction-driven system. We use two of these customized piezo-motors as the actuators for Haptigami.

We personalized a quadrature encoder to enable closed-loop control of the piezo-motor described above. It consists of two bipolar Hall-effect sensors positioned on the stator and thirty $1 \times 1 \times 1 \text{ mm}^3$ square magnets placed with alternating polarity on the side of the rotor. During rotation, the Hall-effect sensors generate two quadrature PWM outputs that go to the microcontroller (Arduino Mega) through a custom-designed electronic low-pass filter. The Arduino's interrupts extract rotation angle and direction, with a resolution of 6° , and uses them as the bang-bang controller input to drive the motors. According to the model presented in section 2.4.1, this resolution translated to values ranging from 3.4° to 4.4° in roll, 0.12° to 2.1° in pitch, and 0.83 mm in compression. The motor driver, supplied by PCBmotor, generates the signal that drives the piezo crystals of the stator. Fig. 2.4 illustrates this flat actuator system.

2.3.2 Low-profile compliant slider-crank mechanism

In order to generate useful movement from a piezo-motor, we developed a novel low-profile and compliant slider-crank transmission described in [69]. The connecting rod, composed of

two Kapton layers of the same thickness and glued using Polymelt adhesive, drives the slider that consists of a single 50 μm Kapton layer. We attached the other end of the connecting rod to the bottom rotor of the piezo-motor, which acts as the crank. During the pulling phase, our transmission functions similarly to a traditional slider-crank. However, during the pushing phase, the flexible elements cannot transmit the motion due to buckling, which may damage the mechanism. To avoid this problem, we introduced a slot in the rod, which allows decoupling of the two phases. We use four such slider-crank mechanisms to generate pitch, roll, and compression, as shown in Fig. 2.5a.

2.3.3 Origami-inspired base structure with embedded transmissions

The base structure forms the main body of Haptigami and embeds the transmissions described above. As for the slider-crank and cam follower, the Haptigami's number of layers has been reduced to a minimum to limit material waste and fasten the manufacturing process. The origami design developed in [33] inspired the base structure. It consists of 27 distinct layers: (i) three 0.2 mm FR4 fiber-glass layers, (ii) one 0.3 mm FR4 layer, (iii) ten 0.05 mm Kapton, and (iv) thirteen Polymelt 701 layers. The first thirteen layers include the blue and dark green slider-crank mechanisms, while the remaining thirteen contain the light green and orange slider-crank presented in Fig. 2.5a. We adopted a four-step manufacturing process (Fig. 2.5b) as described in [69]. After laser cutting the different layers, we stacked them using pins and then glued them together using a heat press to create the 2-D assembly of the device. Finally, we added the actuators of Section 2.3.1 and folded the 2-D assembly using the flexure joints into the 3-D Haptigami, measuring 36 x 25 x 26 mm and weighing only 13 g.

The final structure consists of a top and bottom face connected on three of its edges using a type of origami structure called waterbomb [88], which acts as a spring and helps the device to retain its shape when the piezo motor is not active. The fourth side of the mechanism is open, allowing insertion of the finger. The top and bottom faces of the structure hold the piezo-motor, while the sliders of the four slider-crank mechanisms act as tendons to generate the motion. The compliance of the adopted materials enables the slider-crank mechanisms to transmit motions and forces out-of-plane.

The CAD design of the Haptigami layers can be found in appendix A.3.

2.3.4 Working principle

The presented low-profile Haptigami design is capable of generating roll, pitch, and compression motions and vibrotactile feedback. We use the two piezo-motors and four slider-crank mechanisms described above to drive them. Each motor controls two slider-crank mechanisms, thanks to the decoupling between pushing and pulling phases. We select which of the two transmissions to drive by choosing the motor's direction of rotation. As roll and pitch are connected to different motors, they can be achieved simultaneously. The roll, pitch, and com-

pression motions achieved by Haptigami, along with the corresponding motor commands, are described in Table 2.1:

Top motor direction	Bottom motor direction	Haptigami motion
ccw	-	roll(+)
cw	-	roll (-)
-	cw	pitch (+)
ccw	ccw	compression

Table 2.1: Haptigami motion achieved through motors direction of rotation, clockwise (cw) or counterclockwise (ccw)

As the table describes, it is impossible to achieve compression and pitch simultaneously as compression requires the use of two motors. In order to generate vibrotactile feedback, we alternate the direction of the piezo-motors at high frequency. The direct contact with the user and low inertia aid in transmitting the vibrations to the user's finger with little loss. Thus, the proposed novel robotic platform can produce vibrotactile and 3-DoF force haptic feedback.

2.4 Kinematic model of Haptigami

Haptigami consists of an origami structure actuated by piezo-motors driving the embedded slider-crank mechanisms. As the piezo-motors rotate, the slider pulls on the base structure to create movement, acting as the tendon. In this section, we develop and validate a kinematic model for this mechanism and apply it for closed-loop control of Haptigami.

2.4.1 Kinematic model

Kinematics of most fingertip haptic devices do not change when worn on the finger as they consist of rigid segments and joints [10, 73]. Wearing Haptigami or not changes its kinematics due to its compliant nature. For a realistic kinematic analysis, we could use the true geometry of the finger as the constraint for deriving the kinematics. In this chapter, we model the contact surface to a sphere approximating the fingertip to derive the kinematics equations. This assumption is valid for our analysis because the phalanx does not affect the kinematics since Haptigami pitches only in the forward direction.

We model Haptigami as two squares with equal dimensions and of side length s , as presented in Fig. 2.6b. The bottom face is grounded, while the top face is free, with O and C representing the coordinates of their square centers. The sphere, placed between the two faces, is fixed to the bottom face, with vector $\vec{S}_b = (-Fpos, 0, 0)$ representing the point of contact. $Fpos$ is the distance between the square's center and sphere contact point on the bottom square. We assume the top face to freely slide and roll over the sphere, with the point of contact given by

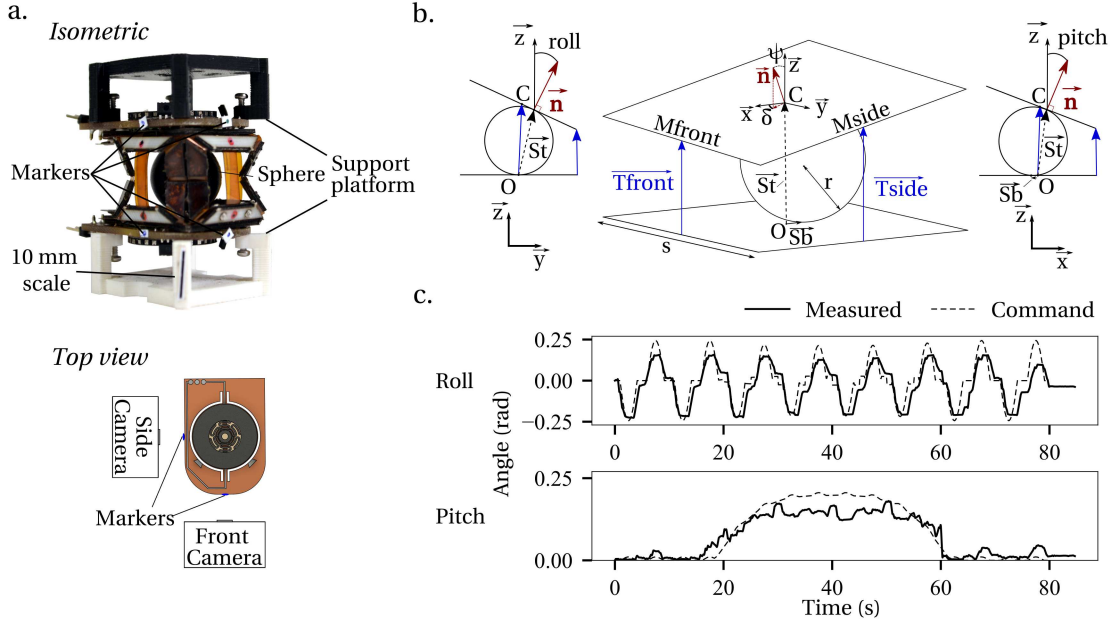


Figure 2.6: Haptigami's kinematic model and closed-loop control experiment and results. a. Experimental setup used to verify kinematic model; We fixed Haptigami on a support platform with a 3D-printed sphere inside and used a front and side cameras to record the marker positions, deducing the tendon lengths and platform orientation. b. We model our system as two plates with a sphere inside, representing the user's finger contact point, and determine the motion of the two plates by the sphere and tendon lengths. c. Comparison between model and the measured values of roll and pitch angles.

vector $\vec{S}_t = \vec{S}_b + r \cdot \vec{z} + r \cdot \vec{n} = (x_0, y_0, z_0)$:

$$x_0 = r \cdot n_x - F_{pos}; \quad y_0 = r \cdot n_y; \quad z_0 = r \cdot n_z + r \quad (2.1)$$

where n_x , n_y and n_z are x, y and z components, respectively, of the unit vector \vec{n} , normal to the upper platform. Using spherical coordinates, \vec{n} is defined as $\vec{n} = (\sin(\psi) \cdot \cos(\delta), \sin(\psi) \cdot \sin(\delta), \cos(\psi))$.

Using the above equations, the plane corresponding to the top face is given by

$$n_x \cdot (x - x_0) + n_y \cdot (y - y_0) + n_z \cdot (z - z_0) = 0 \quad (2.2)$$

We define Haptigami's motion as the relative motion between the top and bottom faces denoted by the Cardan angles roll and pitch, calculated as follows:

$$roll = \frac{\arccos(\psi)}{\sqrt{\sin^2(\psi) \cdot \cos^2(\delta) + \cos^2(\psi)}} \quad (2.3)$$

$$pitch = \frac{\arccos(\psi)}{\sqrt{\sin^2(\delta) \cdot \sin^2(\psi) + \cos^2(\psi)}} \quad (2.4)$$

Controlling the tendon lengths, powered by the piezo-motors allows achieving this motion. The vectors \overrightarrow{Tfront} and \overrightarrow{Tside} , which are connected at the mid-points, $Mfront$ and $Mside$, of the top face edges represent these tendons.

$$\overrightarrow{Tfront} = \begin{bmatrix} 0 \\ (s/2) \cdot (1 - \cos(roll)) \\ Tside_z + (s/2) \cdot \sin(roll) \end{bmatrix} \quad (2.5)$$

$$\overrightarrow{Tside} = \begin{bmatrix} (s/2) \cdot (1 - \cos(pitch)) \\ 0 \\ Tfront_z + (s/2) \cdot \sin(pitch) \end{bmatrix} \quad (2.6)$$

As points $Mfront$ and $Mside$ lie on the top face, they satisfy (2.2).

$$\begin{aligned} n_x \cdot Mside_x + n_y \cdot Mside_y + n_z \cdot Mside_z &= d \\ n_x \cdot Mfront_x + n_y \cdot Mfront_y + n_z \cdot Mfront_z &= d \end{aligned} \quad (2.7)$$

where $d = n_x x_0 + n_y y_0 + n_z z_0$. The set of equations (2.1) to (2.7) gives the kinematics of Haptigami that relate the inputs, $\|\overrightarrow{Tside}\|$, $\|\overrightarrow{Tfront}\|$, to the outputs, $pitch$, $roll$ or ψ and δ . The forward kinematics are difficult to derive due to the complexity of the equations required to isolate ψ and δ . To address this, we use the numeric solver `NLsolve.jl` [89] which gives the correct angle in an average time of 1ms after the first compilation. Solving (2.7) gives the reverse kinematics:

$$\begin{aligned} \|\overrightarrow{Tfront}\| &= (((\cos(pitch)s - s - 2Fpos) \cos(\delta) \\ &\quad - s \sin(\delta)) \sin(\varphi) \\ &\quad + (-\sin(pitch)s + \\ &\quad 2r) \cos(\varphi) + 2r) / (2 \cos(\varphi)) \end{aligned} \quad (2.8)$$

$$\begin{aligned} \|\overrightarrow{Tside}\| &= (((-s - 2Fpos) \cos(\delta) + s \sin(\delta) \\ &\quad (\cos(roll) - 1)) \sin(\varphi) \\ &\quad + (-\sin(roll)s + 2r) \cos(\varphi) \\ &\quad + 2r) / (2 \cos(\varphi)) \end{aligned} \quad (2.9)$$

Additionally, we determine the top plate's centre coordinates as follows:

$$\begin{aligned} \overrightarrow{OC} &= \frac{\overrightarrow{OMside} + \overrightarrow{OMfront}}{2} \\ &\quad + \frac{\overrightarrow{OMside} - \overrightarrow{OMfront}}{2} \times \vec{n} \end{aligned} \quad (2.10)$$

Finally, to control the interface, we converted the tendon lengths into rotation angles of

the driving piezo-motors using the conventional offset slider-crank kinematic equations that relate the motor rotation angle θ , to the tendon length t , as explained in [69]. The slider position x of a slider-crank mechanism, which is a measure of the tendon length, is given by:

$$x = a \cdot \cos(\theta) + b \cdot \cos(\mu(\theta)) \quad (2.11)$$

with

$$\mu(\theta) = \arcsin\left(\frac{a \cdot \sin(\theta) - c}{b}\right) \quad (2.12)$$

where a , b and c , are the crank, rod and offset size, respectively and μ is the angle between the connecting rod and the slider.

We solve the above by using a solver in [90] to get the equation for $\theta(x)$, and we use this equation directly in the control.

2.4.2 Kinematics validation

Here, we control the piezo-motors of Haptigami and compare the achieved pitch and roll motions to those predicted by our kinematics model. We placed a sphere (diameter = 14 mm) inside our prototype at $\vec{S}_b = (-Pos, 0, 0) = (-2, 0, 0)$, to represent a finger as seen in Fig. 2.6b. Using optical markers and two cameras as shown in Fig. 2.6a, we measured the spatial position of Haptigami's top face with respect to the bottom face. To reduce the visual distortion effect on the results, the cameras were put at a distance where the motion of the markers is centered and focused. At this distance, the resolution was 0.05 mm by pixel.

The top motor generates the pitch motion, while the bottom motor is responsible for the roll. We simultaneously sent two sines waves as control signals, traversing the entire rotation range of Haptigami and corresponding to oscillating in both roll and pitch directions. We tracked these reference signals by closed-loop control of the piezo-motors using feedback from our custom encoders presented in Section 2.3.1. We used the auto-tracker *CSRT* algorithm of *OpenCV* [91] for analyzing the video to get the optical marker positions. The performance of this tracking method is assessed in [92] and is more than sufficient for our application due to our low speeds and displacements. The data was acquired at a framerate of 25 fps, then low-pass filtered at 3 Hz.

Fig. 2.6c compares the measured pitch and roll angles of Haptigami to those predicted by our kinematics model. We see that the measured values match our model during the pitch activation time interval from 18 to 60 s, with a root mean squared error of 0.055 rad. We observed a slight reduction in the measured maximum amplitude, which can be attributed to the compliance of the waterbomb structures, affecting the transmission efficiency. In addition, we also observe a higher cross-influence of pitch and roll angles compared to the model. Overall, however, for the approximation of the fingertip as a sphere, our model accurately achieves closed-loop control of the pitch and roll using the embedded hall sensors.

Additional geometrical and mechanical parameters such as more complex finger shape,

skin deformation under pressure, and contact point compliance need to be considered for an updated version of the model. Using a plastic sphere as an approximation of the fingertip allows working with straightforward kinematic equations. Abdouni et al. [93], found the Young's modulus of the fingertip's skin to vary between 20 and 100 kPa in shear, leading to negligible displacements (around 0.02 mm) with the Haptigami shear forces values given by Table 2.2. The same Table gives us the maximal normal force of 693 mN that corresponds to a normal finger deformation of around 1.2 mm according to Dzidek et al. [94]. We estimate the error induced by this deformation by reducing the sphere radius of our current model. This leads to an RMS value of 0.077 rad, which is significant and should be included in a future model. Finally, frictions that differ between plastic sphere and skin could also create disturbances.

2.4.3 Maximal roll and pitch frequencies

To measure the Haptigami's maximum roll and pitch frequencies, we programmed the roll and pitch motors to rotate between their upper and lower limits as fast as possible. We recorded a video of the resulting Haptigami motion and extracted the times when the Haptigami reaches its extremes positions. The roll motion between ± 0.24 rad and the pitch motion between 0 and 0.20 rad have a frequency of 1.6 and 1 Hz, respectively. The pitch speed is slower than the roll due to its slider-crank design as shown by Fig. 2.5 that requires a larger rotor rotation for the same slider displacement.

2.5 Force characterization

Mechanical characterization of any fingertip haptic device is challenging due to the arbitrary physical grounding of the device and preloaded conditions. Here, we present a novel experimental protocol and platform for a quantitative evaluation of meso-scale devices, which can be customized in range and resolution for the target application.

2.5.1 Experimental setup

Similar to the protocol described in [95], we attach the Haptigami onto a bench-top setup, enforce displacement in its range of motion, and measure the blocked forces while powering the two piezo-motors. We accomplish this using a 5-DoF robotic platform as shown in Fig. 2.7a. It consists of three linear motors or stages, capable of enforcing linear displacement in X, Y and Z axis and a pan-tilt mechanism consisting of two servomotors for roll and pitch motions. We affixed the bottom face of Haptigami to the X-Y stages and the top plate to the pan-tilt mechanism, which in turn is fixed on the Z stage as seen in Fig. 2.7a. By controlling these linear motors and pan-tilt mechanism of the characterization platform, we enforce the desired displacement in XYZ and roll-pitch, respectively, to the top plate of the Haptigami. This displacement is based on the model described earlier in Section 2.4.1, assuming a spherical

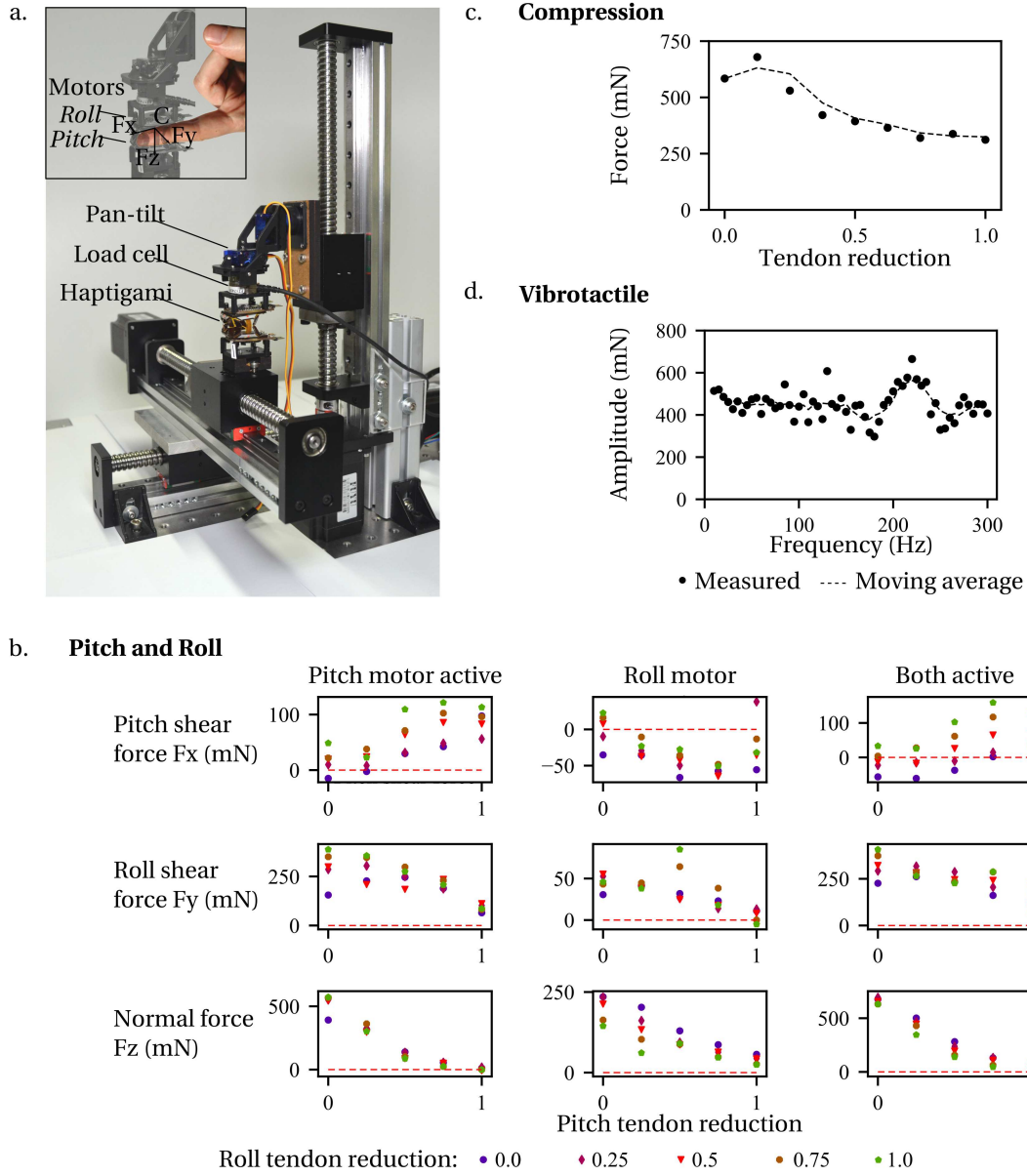


Figure 2.7: Force characterization setup and results. a. Force characterization setup simulating the platform on a finger; we fixed the Haptigami to the 5-DoF platform in direct contact with the 6-DoF load cell. b. For every orientation of its workspace, we measured the force along XYZ axis depending on the actuated motors. The configuration is defined from the normalized tendon length reduction that corresponds to how much the tendon has been pulled by the slider-crank. c. Compression experiment, we attached Haptigami to the platform with a null angle. For different heights, we actuated the roll motors and measured the compression force. d. Vibration experiment, we attached Haptigami to the platform with a null angle and controlled the top motor to move back and forth at different frequencies and measure the amplitude of the resulting signal.

shape for the finger. To calculate the control inputs for the various stages of the characterization platform, we must calculate the individual displacements required in five directions. For the roll and pitch, these values are the same as the roll and pitch angles of the Haptigami. To calculate control values for the X, Y, and Z stages, we consider the X-Y displacements of the Haptigami top plate and those of the pan-tilt mechanism, occurring due to its non-zero arm lengths.

While enforcing the displacement, we measure the blocked force of Haptigami using a *Nano17* 6-axis force sensor from *ATI Industrial Automation* (force resolution = 12.5 mN), attached between the top face of the Haptigami and the pan-tilt mechanism as seen in Fig. 2.7a. We used a custom Labview program to measure the load-cell data and send instructions to the Arduino Mega, which then controls the 5-DoF platform. Lastly, during characterization, we activate the two motors of the Haptigami, also using the Arduino Mega. With this setup, we moved Haptigami to different configurations in its range of motion and characterized it in three scenarios: (i) compression motion (ii) roll and pitch motions (iii) vibrotactile feedback.

2.5.2 Pitch and roll

As seen in Section 2.4.1, the Haptigami motion is a result of shortening of the tendon lengths. We therefore represent its displacement using its input space defined via its tendon length reduction:

$$\text{normalized tendon reduction} = \frac{L_0 - L}{L_0}$$

where L is the current tendon length and L_0 is maximal tendon length, in mm. We displaced the Haptigami in a set of points defined by a grid of 5 x 5, where each grid point corresponds to the front and side tendon lengths, with a maximum value of 2 mm on each side. This motion corresponds to a total pitch of +10° and roll of +12°, assuming a sphere of 14 mm diameter placed inside. We calculated the spatial orientation (x, y, z, δ, ψ) of Haptigami at the grid points using the kinematic model described in Section 2.4.1 and converted into a set of instructions for the 5-DoF robotic platform. For every grid point, we used the following protocol: 1. Move Haptigami to a new position, 2. Activate pitch motor, 3. Activate roll motor, 4. Activate both motors. We programmed each motor activation to last two seconds and then come back to the initial position.

Fig. 2.7b shows the measured forces vs. normalized tendon length reduction of Haptigami. The Y-axis represents the measured forces, while the X-axis and different markers represent displacements in the pitch and roll directions, respectively, expressed in normalized tendon lengths. These forces are generated by the front and side tendons pulled by the pitch and roll piezo-motors, respectively. Therefore they depend on the relative orientation of the tendon force with respect to the top face, as well as its magnitude, which depends on the torque of the

piezo-motor, and orientation and design of the slider-crank mechanism.

With increasing displacement in the pitch direction, the component of the tendon force $\overrightarrow{T_{front}}$ in the X-axis increases. This leads to an increasing pattern of force vs. displacement for X-direction and a decreasing one for the Y and Z directions, as seen in the first column of Fig. 2.7b. A similar pattern is expected for the roll direction, but the measured data does not completely follow this, as seen in the second column of Fig. 2.7b. This deviation could be attributed to mechanical interference in the compliant transmissions due to the fact that both motors contribute to the roll motion. The third column of Fig. 2.7b corresponds to both motors active, pulling in roll and pitch directions. Therefore, the plots are somewhat equal to the sum of the first two columns, which we found was especially true for F_z . Another observation is that the forces are generally higher for pitch motor active, as compared roll motor active. This is because the crank radius for the slider-crank mechanism is smaller for the former as compared to the latter, as described in Section 2.3. Lastly, due to the underactuated and coupled design of the Haptigami, we see from the third row of Fig. 2.7b that compression forces always accompany shear forces. The maximum forces are 690 mN in normal force, 407 mN in shear roll, and 159 mN in shear pitch.

2.5.3 Compression

We controlled the characterization platform to only move its Z stage and displaced Haptigami from an initial height of 20 mm to a final height of 16 mm in steps of 0.5 mm. We activated both motors according to Table 2.1 and measured the maximum compression force at each step, held for 2 s. Fig. 2.7c shows the measured force, with the X-axis denoting the displacement expressed as normalized tendon length. We see that the compression force slightly reduces with increasing displacement, with a maximum value of 678 mN.

2.5.4 Vibrotactile feedback

As explained in Section 2.3.4, Haptigami can generate vibrotactile feedback by alternating its motors rotations at high speed. We powered the top motor at a range of frequencies between 10 and 300 Hz, which correspond to the maximum human perception frequency [96], and measured the force amplitude using the 6-axis load-cell.

The measured vibrational waveform consists of alternated peaks corresponding to the directional change of the piezo-motor. Fig. 2.7d shows the measured peak-to-peak force difference for the various tested frequencies. Other than the small peak at around 220 Hz, the force characteristics seem constant across the frequency range, with a mean value of 451 mN and a standard deviation of 73 mN. While we tested only the top motor here, we believe that using both motors will increase the force amplitude.

	Force (mN)		
	Pitch shear	Roll shear	Normal
Pitch motor	121	387	572
Roll motor	38	85	235
Two motors	159	407	693

Compression: 679 mN

One motor vibration amplitude peak: 664 mN

Table 2.2: Table summarizing the maximum normal, shear and vibrotactile force capacity of our device.

2.6 Conclusion and future work

Producing multiple degrees of mechanical stimulation from a wearable fingertip haptic platform is challenging. Generating a realistic user experience for any haptic interface demands embedding several mechanical functionalities at the centimeter scale, which inevitably pushes the limit of physical and material structural mechanics. Here, we present Haptigami, a novel concept and design of a compact and wearable haptic device that renders cutaneous and vibrotactile feedback. Using only two low-profile piezo-motors, it is able to generate compression, roll, pitch, and vibrotactile feedback, which create a diverse range of haptic sensations, including contact and pressure display, curvature display, shear forces, stiffness and vibration, and texture. The use of piezo-motors and the low-profile mechanisms introduces a new approach in manufacturing low-profile, lightweight and compliant wearable devices. We derived and validated a model for the kinematics of Haptigami prototype. Based on the size of the finger, the kinematics model can be adapted to achieve closed-loop position control. In order to quantitatively assess mechanical capabilities, we developed a novel experimental protocol and platform to characterize the forces applied by Haptigami in its range of motion. The Haptigami provides forces ranging from 150 to 690 mN in different actuation modes, which are greater than the human skin perception threshold of around 41 mN as described by [97]. Using these values, we can model the force output of the Haptigami as a function of its kinematic orientation and inputs to implement force or stiffness control. In addition to the novel design approach, we addressed another challenge in the existing literature related to quantifying haptic feedback. Our presented method of force characterization is complete and comprehensive, providing a repeatable and consistent method of measuring the various modes of actuation in the entire range of motion of the Haptigami. This could be applied to other existing or upcoming meso-scale devices for characterizing their mechanical behavior. By comparing different devices and by additionally conducting user studies, we would be able to link and quantify the relation between the mechanical output of a meso-scale haptic device to the result of a psychophysical experiment.

Due to its size and compliance to the finger, Haptigami has multiple uses. In addition to virtual reality applications, it can provide haptic feedback for object manipulation or, in

general, interaction with a physical environment. It could help to orientate hands in space for reaching an invisible target (e.g. in surgery [98] or assisting blind people). Finally, having both force and position feedback directly at the fingertip augments our ability to manipulate objects [99] in terms of precision and environmental perception by enhancing the perceived sensations.

Our future work will define an optimized design process for what design is optimal for a specific finger size in order to customize Haptigami to its user. Additionally, we will study different Haptigami elements such as piezo-motors, mechanisms, and materials; and design parameters such as origami-structural stiffness, friction, electric signal frequency, and power to improve haptic performance. Furthermore, using Inertial Measurement Units (IMUs), we will implement further closed-loop position control for the pitch and roll motions. Using the data from our characterization, we will develop models for Haptigami force output in order to implement force control. Lastly, we will test the device on several users to better understand the relation between applied the forces and haptic feedback.

3 Flexure Variable Stiffness Actuators

This chapter presents our approach using origami robotics advantages to create a compact, multi-DoF, and mechanically capable system. Backed by the previous chapter's experiences, this device uses the unique properties of flexure joints combined with the numerous degrees of freedom and fabrication advantages of origami robotics. The resulting system is an elastic actuator, called flexure variable stiffness actuator (*F-VSA*) using an origami structure as elastic elements. The latter act as a transmission that does not need extra springs assembly as it benefits from the flexure hinges' inherent stiffness. Hence, our device acts as a variable stiffness actuator (VSA) with integrated springs and transmissions that do not hinder the system's compactness. In this research, we designed and manufactured a *F-VSA* prototype able to adjust the force position and stiffness of the end-effector along four degrees of freedom. To control our device, we implemented a model suitable for complex closed-chain mechanisms that return the *F-VSA*' stiffness matrix. We assessed this model's precision by creating four degrees of freedom experimental platform measuring the end-effector's force for all end-effector positions and origami' structure configurations. Finally, we created and evaluated a control strategy that uses this model to generate a desired force at the end-effector. The *F-VSA* illustrates the capabilities of origami robotics in enhancing the functionalities and mechanical capabilities of mechanical systems without compromising manufacturing process complexity and compactness.

3.1 Introduction

Achieving safe human-robot interaction becomes crucial with the developments of many robotics fields such as rehabilitation, assistance, service, wearables, and haptics. To this end, researchers have explored alternatives to conventional fully rigid actuation methods such as soft actuators and electromechanical motors combined with elastic elements. Soft actuators using pneumatics [100], hydraulics [101, 102], elastomers [103], and smart materials [104] have proven to enhance the user's safety [105, 106]. This category also includes variable stiffness

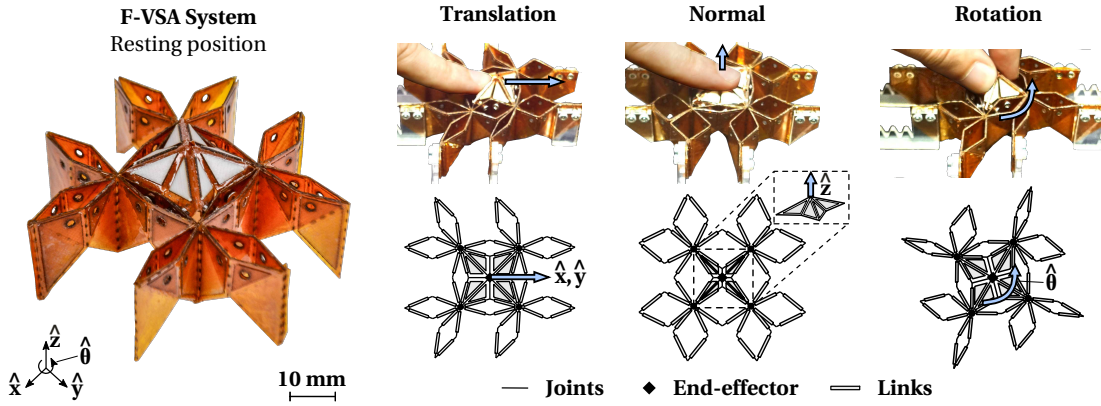


Figure 3.1: The flexure variable stiffness actuator system. It is composed of several compliant four-bars linkages connected to each other with folding hinges and the out-of-plane mechanism in the center serving as end-effector. These diamonds dictate the kinematics of the platform and serve as series elastic elements thanks to their built-in compliance, which act as virtual springs. Moreover, by reconfiguring the diamonds' geometry, this platform can vary the stiffness of these virtual springs. Thus, this device can render variable stiffness and forces by controlling its configuration. It allows the design of compact devices thanks to the compliant diamond patterns and hinges that combine transmission mechanisms, elastic elements, and variable stiffness.

soft actuators relying on jamming¹ [107–109] or smart materials [104, 110]. However, soft actuators suffer from complex modeling, difficult control, low actuation speed, and bulky power supplies [111, 112]. This study focuses on the alternative compliant actuation method that uses conventional actuators coupled with elastic elements such as series elastic actuators (SEAs) and variable stiffness actuators (VSAs), which shows better capabilities regarding the aforementioned soft actuators limitations.

SEAs [113–119] consist of actuators connected to elastic elements and loads in series [120]. The elastic elements serve three main purposes: (i) store and release energy, thus improving energy efficiency [121], (ii) convert the force control problem to a position control problem due to the well-defined relationship between elastic deformation and output force [120], and (iii) reduce peak forces on the motor and user during impact, thereby improving safety [122]. However, SEAs usually hinder the actuator's bandwidth, thus limiting the capabilities. Moreover, they cannot adapt their stiffness with respect to the different loads and conditions, which can cause undesired oscillations [123].

Unlike SEAs, VSAs [124–126] tune the stiffness of their elastic elements to adapt their compliance and bandwidth to changing environments and conditions. For example, higher stiffness configurations enable faster response and better fidelity performance, while lower stiffness configurations reduce the impact of collision and achieve safer and more stable force and

¹The layer jamming mechanism exploits the friction present between layers of thin material, which can be controlled by a confining pressure.

torque output. VSAs are categorized into three general groups based on how they vary their stiffness: spring pretension, changing transmission, and changing physical properties of springs [120, 127]. While each of these categories has specific assets and liabilities, they suffer from a common limitation: the need for extra components and mechanisms [120, 128, 129] which leads to an increase in complexity, weight, size, and time of assembly [130]. These challenges set back the ability of VSAs to target applications requiring miniaturized devices with multi-DoF force outputs [116] such as wearable devices and haptics.

To address mechanical complexity issues of VSAs, researchers have investigated the use of flexure hinges for compliant mechanisms. Flexure-based mechanisms enable the design of miniaturized, compact, and lightweight multi-DoF mechanisms and robots with a reduced number of components [12, 37, 39, 131–133]. In VSA, existing studies [127, 134–136] use flexure hinges and mechanisms as variable stiffness elements. In these works, the flexure mechanisms only serve as compliant springs and attachments connecting the motor to the linkages or other transmission components, which do not solve the complexity issues of VSAs. Moreover, flexure-based mechanisms stiffness is often found by experimental characterizations due to difficult modeling. This is accentuated in mechanisms with complex folding patterns and closed kinematics chains.

In this chapter, we present flexure variable stiffness actuators (F-VSAs) that address the mechanical complexity of VSAs by combining kinematic transmission, elasticity, and variable stiffness in repeating folding patterns as shown in Figure 3.1. The folding patterns are composed of flexure hinges, which act as virtual springs and add elasticity to the system. By virtue of their design, the overall stiffness of F-VSAs is a function of the folding pattern configuration, which can be modulated using actuators. The flexure-based folds serve as links and joints defining the kinematics of a system. Thus, by combining all in one, they do not need extra elastic elements and mechanisms to achieve variable stiffness. Furthermore, our general stiffness modeling approach based on matrix structural analysis method enables the estimation of the stiffness of F-VSAs at different configurations for any folding pattern. Hence, the model allows the modulation of stiffness and force output by the active control of the folding pattern configuration.

Using this method, we create a four-DoF F-VSA system that provides stiffness and force output. The device uses eight motors at its periphery to actuate the central end-effector and control stiffness and force output. We conduct stiffness modulation and force control experiments and verify that we can modulate the stiffness and force output of the system. The proposed model successfully predicts the actual behavior in the entire workspace. Thus, our F-VSA method proposes a new paradigm toward compact multi-DoF robot design for many robotics fields such as wearables, rehabilitation, and haptics, which requires mechanical force and torque control stability.

3.2 Flexure Variable Stiffness Actuator overview

This section describes the flexure variable stiffness actuator (F-VSA) and compares design and capabilities with other elastic actuators such as SEAs and VSAs. To allow force and stiffness control of our system, we also introduce a method to model the stiffness that can be applied to any F-VSA design.

3.2.1 F-VSA design and features

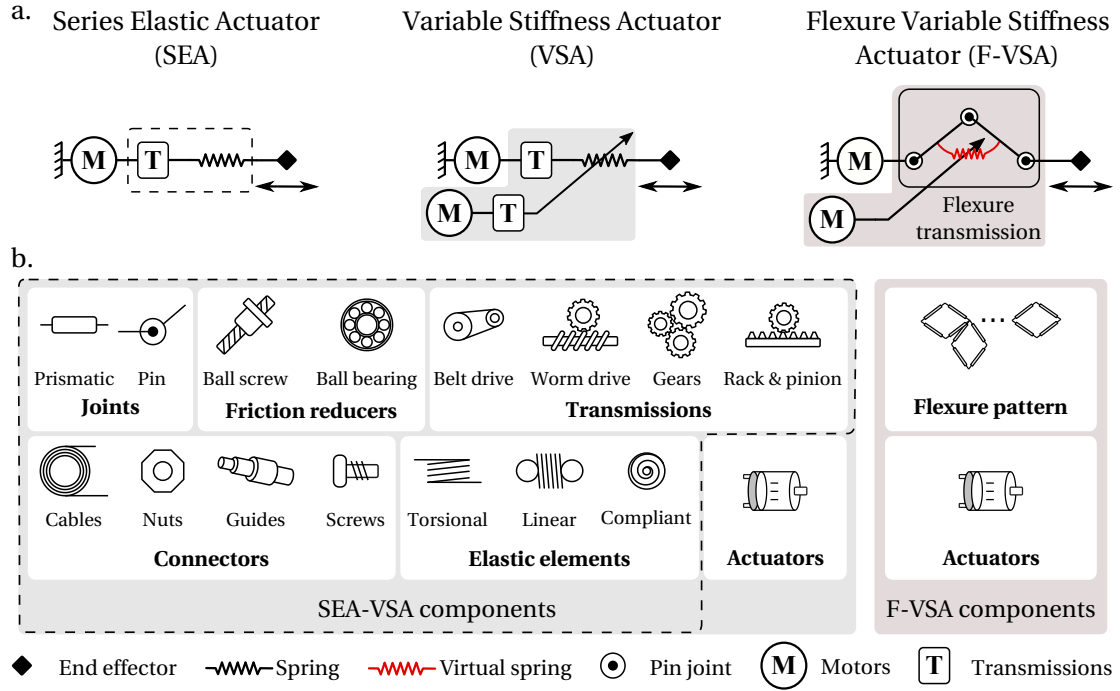


Figure 3.2: Comparison of SEAs, VSAs, and F-VSAs. SEAs are generally composed of many types of components such as joints, transmissions, connectors, elastic elements, and friction reducers. SEAs cannot adapt the stiffness of their springs to changing conditions. On the other hand, VSAs can vary the stiffness of their elastic elements by using additional aforementioned components and extra actuators. However, they suffer from mechanical complexity and bulkiness. As a new approach, F-VSAs incorporate all these components in their flexure transmission, which has virtual springs at its joints and defines the system's kinematics. We can control the configuration of the flexure transmission to dictate the overall stiffness of the system. Thus, F-VSA method offers a solution to the mechanical complexity issue of VSAs. These three approaches and their design components are summarized in a and b.

The Flexure Variable Stiffness Actuator (F-VSA) is an alternative to SEAs and VSAs. It reduces the mechanical complexity to enable miniaturized robot design providing force and stiffness output with a compact form factor. To illustrate how the F-VSA differs from SEAs and VSAs, we represent these three concepts in Fig. 3.2. The SEAs and VSAs are composed of the following elements:

- End-effector: The point of the system that interacts with the environment. Elastic actuators aim at controlling the force and position at the end-effector.
- Elastic elements: They add compliance to the system and generate force and torque based on their compression or tension. For SEAs and VSAs, springs are often used as elastic elements.
- Actuators: They control the elastic elements and therefore the force output at the end-effector.
- Transmissions: They define the kinematics, speed, and force characteristics of the actuator.

Unlike SEAs, VSAs add extra actuators, elastic elements, connectors, friction reducers, and mechanisms with different approaches to achieve variable stiffness [120, 130], increasing the mechanical complexity. As an alternative to SEAs and VSAs, F-VSAs utilize flexure patterns as both kinematic transmission and elastic elements. The inherent stiffness of the flexure joints used in the transmission defines the overall stiffness of the system. Therefore, by changing the configuration, one can vary the overall stiffness and control the force output and position of the end-effector. Furthermore, the flexure joint reduces the number of mechanical parts and components required for achieving multi-DoF structures as shown in Figure 3.2b. Thus, this method significantly reduces the mechanical complexity and bulkiness of the system by combining many functionalities in flexure transmission and ensuring mechanical capabilities and reduced assembly complexity.

Although improving the compactness of a force-output system by reducing the mechanical complexity, F-VSAs come with a stiffness modeling challenge, especially for multi-DoF systems. They require a general stiffness modeling of flexure transmission to estimate the overall stiffness at any configuration. The model needs to take into account material properties, geometric parameters, and any type of kinematic chains. For these reasons, we use the Matrix Structural Analysis (MSA) method for stiffness modeling of F-VSAs.

3.2.2 Matrix Structural Analysis method overview

To actively control the stiffness and force output of F-VSAs by changing their configuration, we study its all-inclusive stiffness model by considering initial and boundary conditions, material properties, and dimensions. In this thesis, we use the Matrix Structural Analysis (MSA) method [137] to model the stiffness of F-VSAs. Compared to two other stiffness modeling methods: virtual joint modeling (VJM) [138] and finite element analyses (FEA) [139] in the literature, the MSA has less computational expensiveness than the FEA method and also considers the flexibility of the links compared to VJM. Particularly, Klimchik et al. [140] presents a systematic approach to applying MSA method to a large range of mechanisms in their study. Their approach is compatible with over-constrained parallel mechanisms with closed-loop

chains, flexible links, and joints, making it the most suitable method to model the stiffness of F-VSAs.

The MSA method proposed by Klimchik et al. [140] can be achieved in four steps summarized by Fig. 3.6a:

1. **System description:** describe the mechanical system as a collection of elements which is composed of nodes, links, joints, platform, and boundary conditions:
 - The nodes are the basic elements of the system. The force-displacement relations between them are what define links and joints. A link is described with two nodes, while a joint can connect more than two nodes together. In addition, boundary conditions affect some nodes that can be under external loading. This is the case for the end-effector node.
 - Joints can be rigid, passive, or elastic and connect link, base, and platform. While rigid joints fully transmit displacement and force conditions between nodes, passive and elastic joints are defined with one or multiple Degrees of Freedom (DoF) in rotation and translation. Finally, the force transmitted along the free axis can be null for the passive joints or defined by a stiffness matrix for the elastic joint.
 - Links can be either rigid or flexible. While rigid links assume that the distance between nodes is kept constant, flexible links are defined using the stiffness matrix of the element. The latter can have a beam shape to simplify the problem or a complex geometry from which stiffness coefficients are extracted using a CAD-based method [141].
 - In a parallel manipulator, the platform connects the different branches of the system to the end-effector node. Similar to the links, the platform can be either rigid or flexible by including stiffness coefficients.
 - The boundary conditions are defined by the connections between the aforementioned elements and the system base. This category also includes the external wrenches applied on some of the nodes, necessary to constrain the system entirely.

2. **Force displacement relation:** for each element, we write all force-displacement relations in the matrix form as follows:

$$\begin{bmatrix} \mathbf{A}_W & \mathbf{A}_{\Delta t} \end{bmatrix} \cdot \begin{bmatrix} \mathbf{W} \\ \Delta \mathbf{t} \end{bmatrix} = \begin{bmatrix} \mathbf{b}_0 \end{bmatrix} \quad (3.1)$$

\mathbf{W} and $\Delta \mathbf{t}$ correspond respectively to the wrench and displacements variables along the three rotation and translation axis. \mathbf{A}_W and $\mathbf{A}_{\Delta t}$ are the coefficients matrices corresponding to \mathbf{W} and $\Delta \mathbf{t}$ respectively. \mathbf{b}_0 is the right-hand side of the corresponding equation/constraints, such as pre-loadings or external wrenches.

If we write (3.1) for links and joints with two nodes, we have twelve equations corresponding to the number of rows. In the case of joints linking three or a higher number of nodes, we will have six more equations per node. Finally, we have six equations for the boundary conditions.

3. **Matrix aggregation:** this method requires the concatenation of all the element matrix equations (3.1) into a larger linear matrix equation. The latter should contain the end-effector node equations in the last rows, such as

$$\begin{bmatrix} \mathbf{A} & \mathbf{B} \\ \mathbf{C} & \mathbf{D} \end{bmatrix} \cdot \begin{bmatrix} \boldsymbol{\mu} \\ \Delta \mathbf{t}_e \end{bmatrix} = \begin{bmatrix} \mathbf{b} \\ \mathbf{W}_e \end{bmatrix} \quad (3.2)$$

with \mathbf{B} , \mathbf{C} , and \mathbf{D} the coefficients associated with the end-effector node and equations, and \mathbf{A} the remaining equation coefficients. Force and displacement variables are aggregated in $\boldsymbol{\mu}$ while $\Delta \mathbf{t}_e$ is a vector of the six displacement variable of the end-effector. Finally, \mathbf{b} and \mathbf{W}_e are the initial conditions of the different element and end-effector, respectively.

4. **Solve the system:** consequently, we can derive the relation between end-effector displacement $\Delta \mathbf{t}_e$ and force \mathbf{W}_e from equation 3.2:

$$\mathbf{W}_e = (\mathbf{D} - \mathbf{C} \cdot \mathbf{A}^{-1} \cdot \mathbf{B}) \cdot \Delta \mathbf{t}_e + \mathbf{C} \cdot \mathbf{A}^{-1} \cdot \mathbf{b} \quad (3.3)$$

from which one can extract the desired stiffness matrix

$$\mathbf{Kc} = \mathbf{D} - \mathbf{C} \cdot \mathbf{A}^{-1} \cdot \mathbf{B} \quad (3.4)$$

and the constant force component:

$$\mathbf{W}_e^0 = \mathbf{C} \cdot \mathbf{A}^{-1} \cdot \mathbf{b} \quad (3.5)$$

To get a further understanding, we made an application example of the MSA method applied on a four-bar linkage in appendix A.7.

The MSA method is also applicable to the singular F-VSA configurations caused by a null moment arm on the joints. In these cases, the F-VSA cannot reconfigure, which makes the structure fully rigid. These particular configurations are considered by the MSA method that returns a stiffness matrix depending exclusively on the links' stiffnesses. However, the MSA method does not consider the kinematic limitations of the F-VSA structure. Hence, the stiffness of a mechanism blocked because of internal moving parts kinematic conflicts will not be assessed correctly with the current method. These singularities' stiffness should be analyzed by removing the joints reaching their displacement limit in the MSA description of the system.

3.3 F-VSA system: a four-DoF device with force and stiffness output

Based on the design method of section 3.2.1, we created an F-VSA system as a proof-of-concept. Our compliant structure provides force transmission, series elasticity, and variable stiffness and force output. First, this section describes the design and working principle of the F-VSA system. Then, we demonstrate that we can manufacture the F-VSA elements using several methods. Finally, we described our structure to apply the analytic model of section 3.2.2 and used it to develop a control strategy for the F-VSA system.

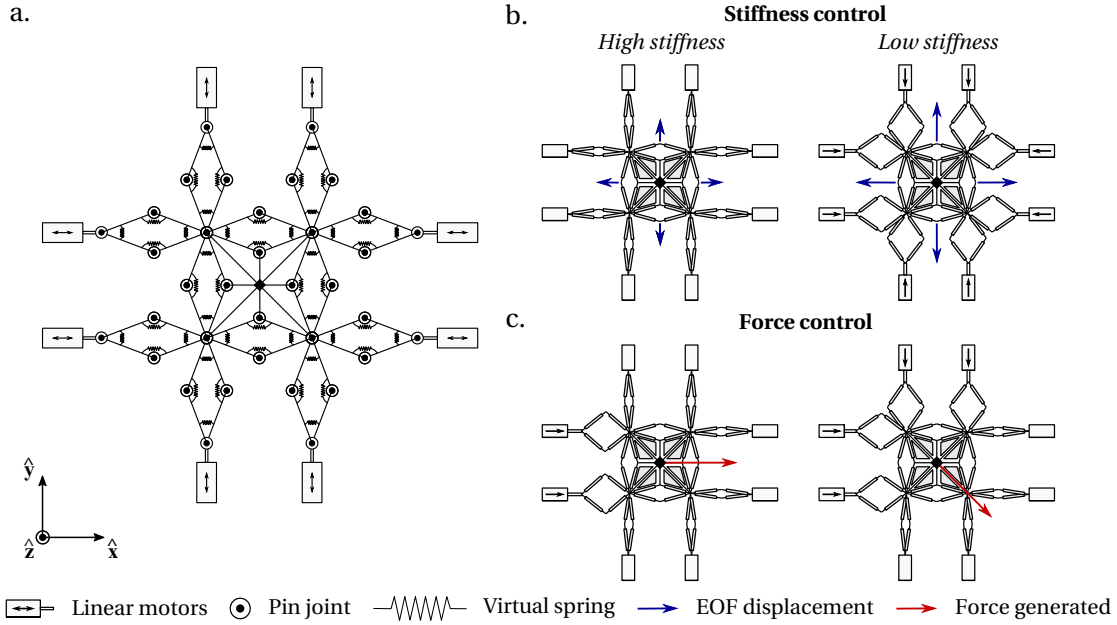


Figure 3.3: Working principle of the F-VSA system. a. The F-VSA system is composed of compliant joints that act as pin joints and virtual torsional springs. b. By controlling the configuration of the diamonds, we can vary and control the stiffness of the end-effector. c. Moreover, our device can generate force in a specific direction at the end-effector that can be controlled by changing the system's configuration.

3.3.1 Design and capabilities

We demonstrate the F-VSA design principle through a proof-of-concept shown in Fig. 3.1. This design is a highly redundant kinematic structure used as a four-DoF haptic system able to render force and stiffness output. It consists of a grid of twelve diamond patterns linked together by compliant pin joints and an out-of-plane mechanism in the center. The latter acts as the end-effector for user interaction and can move in translation in the \hat{x} , \hat{y} , and \hat{z} axes, and rotation in the \hat{z} axis. The external vertices of the outer eight diamond patterns are attached to linear servo motors through compliant hinge joints. The motors control the extension/contraction of the eight outer diamonds as shown in Fig. 3.3, which defines the input space of the device. These motors change the geometry of the outer diamond patterns,

3.3 F-VSA system: a four-DoF device with force and stiffness output

which changes the overall stiffness at the end-effector. When the diamonds are in the extended state, the stiffness is high; and when the diamonds are in the compressed state, the stiffness is low.

The F-VSA system is composed of the following types of repeating elements:

- **Diamond pattern:** This component primarily serves as the stiffness and transmission element of the device. It consists of four rigid tiles connected to each other with flexible hinges, such that it forms a closed-chain rhombus when viewed from the top. Its displacement is defined by the compression/extension in the diagonal directions.
- **Out-of-plane mechanism:** The main objective of this component is to generate out-of-plane motion in the F-VSA. It is a transmission that consists of a square with compliant pin joints along the diagonals and the lines joining mid-points of opposite edges. This divides the square into eight triangles with joints that alternate their direction of rotation. When the corner points of the square are pushed in, the mechanism pushes the central point out of the plane, as seen in Fig. 3.3a. Its displacement is thus defined by the planar motion of the corner points of the square, and the out-of-plane motion of its central point. We design the compliant pin joints of the out-of-plane mechanism to have negligible compliance compared to the diamonds.
- **Actuator:** This is the active component, whose main objective is to generate motion in the structure. It can be connected to either the diamond or the out-of-plane mechanism.

When combined together, networks of diamond and out-of-plane mechanisms can generate highly redundant motions with non-linear stiffness characteristics. When different sections are actively controlled with actuating elements, we can get a controllable surface that is compact, compliant, capable of moving in multiple directions, and can generate a large range of force and stiffness output along multiple degrees of freedom. We consider two main types of outputs:

1. **Stiffness control:** When deformed, internal restoring forces are developed at the joints of the device, which are transmitted to the end-effector when the latter moves. Due to the multiple joints in the system, this restoring force depends on the structure's geometry in addition to the materials used for making the pin joints. By controlling the actuators, we can reconfigure the structure's geometry, thereby tuning the natural stiffness at the end-effector.
2. **Force control:** The second way of producing force and stiffness output is by actively controlling the position of the motors. Due to the elasticity of the overall structure, these forces are generated indirectly through the deformation of the compliant joints.

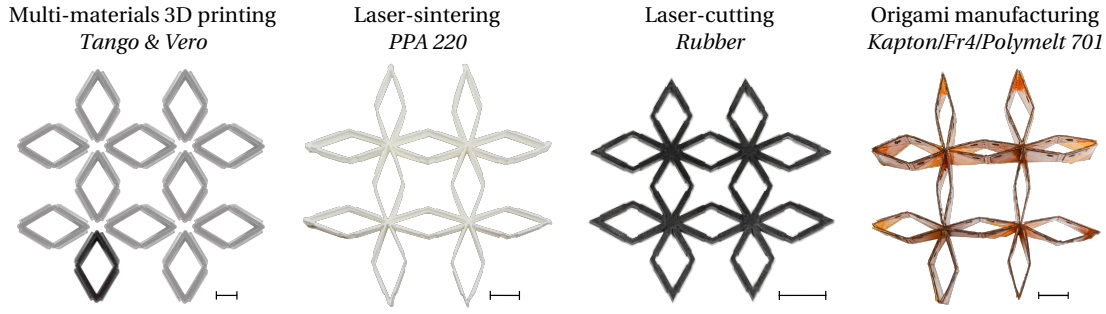


Figure 3.4: Proofs of concept using four manufacturing methods. We explored four manufacturing strategies to fabricate our system: multi-material 3D printing, laser-sintering, laser-cutting of flexible material, and origami manufacturing. All the scales of this figure have a 10 mm length. For each method, we made a proof of concept demonstrating that our design is independent of the fabrication method. Regarding the multi-material 3D printed prototype, only one diamond was built. We make the final prototype using the origami manufacturing method due to its robustness and ability to tune the stiffnesses of the hinges.

3.3.2 Manufacturing methods

Our platform relies on the stiffness of the compliant pin joint to modulate the force at the end-effector. Achieving such a device using conventional pin joints and springs is possible at the cost of a time-consuming assembly that would result in a bulkier platform. On the other hand, compliant joint combines spring and pin joint in a compact and assembly-free embodiment. They are also exempt from backlash, wear, and frictions and can be achieved through several manufacturing strategies. The choice of the latter depends on the application, the ability to tune the stiffness of the joints, and the fabrication time. We attempted to fabricate our device using the four following manufacturing processes:

- **Multi-materials 3D printing:** This technology benefits from all the advantages of conventional 3D printers and allows fast and assembly-free prototyping. We used the *Connex 500* to 3D print a diamond composed of flexible (*Tango*) and rigid (*Vero*) materials. With this technology, the stiffness of the joints is directly related to the material thickness and can be tuned by modifying the design parameters. However, we observed that the flexible material is prone to break after several folding of the joints.
- **Laser-sintering:** This manufacturing process produces assembly-free and robust prototypes. We used the *EOSINT P 395* to 3D print our complete device, using *PA 2200* as material. This method uses a laser that sinters the *PA 2200* powder layer-by-layer to create 3D structures. We designed a thin layer of the material to make compliant pin joints and tune their stiffness by modifying the layer's thicknesses. We create the links using a larger material thickness. However, the laser resolution limits the material size, which does not allow the fabrication of low-stiffness joints.
- **Laser-cutting of flexible materials:** This method uses a laser to cut a flexible material.

We used a high-precision custom UV laser to cut a rubber layer of 1 mm thickness. This manufacturing method is fast, assembly-free, and easily scalable. Similar to the laser-sintering process, joints and link stiffnesses are defined by the thickness, material, and design parameters of the layer. Nevertheless, larger stiffnesses require increased link and joint dimensions, which can be challenging for small devices.

- **Origami manufacturing:** This method consists in assembling layers of functional materials in 2D and folding the resulting stack to create a 3D structure. This manufacturing strategy allows the creation of compact, scalable, and highly customizable robots, known as Origami robots or Robogami [4, 6, 12, 21, 36, 37, 39, 68]. We fabricated this prototype of the F-VSA system with Kapton for the flexural joints and fiberglass FR4 for the rigid tiles. Kapton has been proven to be a reliable and durable material that can withstand numerous folding cycles at high-speed [142] and is therefore suitable for the F-VSA system's joints. Our origami-inspired layer-by-layer fabrication process is described in detail in section 3.3.3. This manufacturing method allows tuning material property, design, and thickness to create durable joints and links with different properties. However, the downsides of this method are caused by the minimal assembly and folding process, which are time-consuming.

The resulting devices are shown in Fig. 3.4. The aforementioned limitations of multi-material 3D printing, laser-sintering, and laser-cutting could be solved by using more suitable material and more precise machining. We selected the design dimensions of these prototypes by considering the constraints imposed by the manufacturing machines, such as printing, cutting area, or process resolution. In this study, since robustness and stiffness modulation are essential criteria, we fabricate our device using the origami manufacturing technique detailed in the next section. As for the other devices of this thesis, the manufacturing process has been optimized to minimize the number of functional layers. The resulting device design is large enough to enable easy manual assembly and folding process, and have its end-effector manipulated by hand.

3.3.3 Origami fabrication of the F-VSA system

The origami pattern presented in this chapter is novel and has been created to achieve our platform design. We wanted to create a metamaterial that would be highly reconfigurable to play with the inherent stiffness of its joints. We were strongly inspired by the kirigami pattern and folding process presented by [143], but changed the honeycombs into squares, constraining the structure to have a positive Poisson ratio. Our new pattern, as well as the folding sequence to achieve the F-VSA system, is shown in Fig. 3.5. This pattern also includes holes that are visible in Fig. 3.1. They are used to insert pins that align flexible and rigid layers during the assembly process. After creating and gluing this stack of functional layers, we fold half of the squares on themselves and insert extra water-bomb origami in the resulting interstices. The central square is the gap in which the platform, which is also an origami

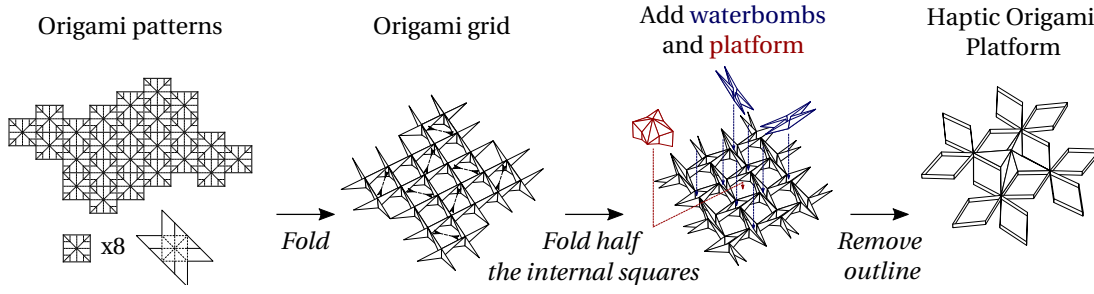


Figure 3.5: Origami folding sequence of the F-VSA system. First, the F-VSA system's pattern is laser cut on a flexible layer. The first folding process creates origami squares, of which half are folded on themselves to create interstices. Extra waterbombs are placed in these interstices, and the platform, also made out of a water-bomb pattern, is attached to the origami's central square. Extra external links and joints are removed from the resulting structure to create the final origami and attach it to the servo-motors.

water-bomb, is fixed onto. This folding sequence allows the making of the internal diamonds that compress or expand to modulate the stiffness of the platform. Lastly, we cut out the extra links and joints and fix the F-VSA system external diamonds to the servo-motors.

Our current prototype is made from three material layers: a 0.2 mm thickness Fr4 that is rigid and defines the system's links, a 0.05 mm thickness Kapton that creates the elastic joints, and one layer of Polymelt 701 used to glue Kapton and Fr4. First, we combine Kapton and Polymelt, and laser cut the result into the patterns presented by the first step of Fig. 3.5. With the help of alignments pins, we stack the Fr4 on the part that needs to be made rigid and fix it by melting the Polymelt using a heat press. Finally, the additional water-bomb and platform are created with the same method and integrated into the main structure during the folding process by heat pressing.

The CAD design of the FVSA layers can be found in appendix A.4.

3.3.4 System description for the MSA

To apply the MSA method to the F-VSA system, first, we assign the elements and nodes as described in the first step of the procedure presented in section 3.2.2. The F-VSA system has 52 flexible links, 76 passive or elastic joints, and one flexible platform for a total of 109 nodes, as shown in Figure 3.6. The links are composed of Kapton, FR4, and Polymelt. Since the thickness and stiffness of Fr4 is significantly larger than the others, we assume that only the latter contribute to the link stiffness. We approximate the links as beams of 12.5 mm length, 25 mm width, and 1 mm thickness and assume FR4 Young's modulus and Poisson coefficient as 24×10^9 and 0.136.

When it comes to the joints, as shown by Fig 3.6, the F-VSA system model requires three types of rotary joints: one-DoF Elastic (solid ellipse), one-DoF passive (dashed ellipse), and joints with one-DoF elastic and one-DoF passive (solid and dashed ellipse). We assume that

3.3 F-VSA system: a four-DoF device with force and stiffness output

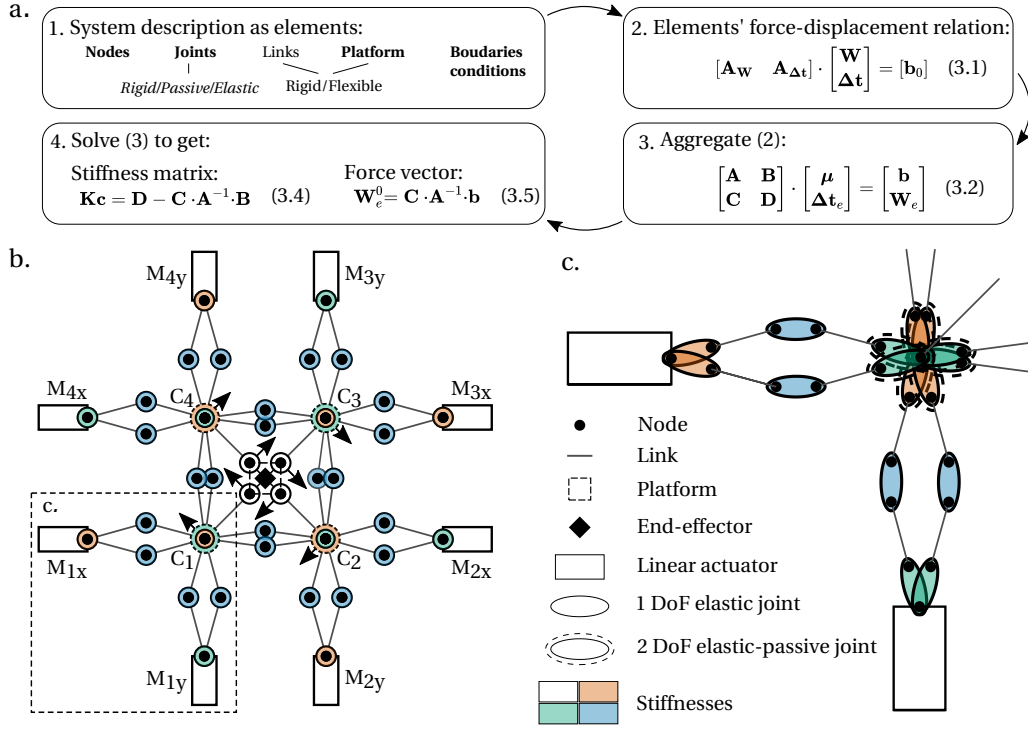


Figure 3.6: Description of the F-VSA system for the MSA method. a. Is a summary of the four steps of the MSA method. First, the system is described as five categories of elements and their associated types. For each element, write the force-displacement relation as matrix and aggregate them. Finally, in step 4, the sub-matrices of this aggregation allow finding the stiffness matrix and force vector relation. b. and c. show the locations of nodes, rigid links, and elastic and passive joints. The different stiffnesses of the joints that occur because of the folding process are indicated with a color code. Figure b represents the top view of the system and the orientation of the joints basis. The points C and M represent the four central nodes and the eight motors of the F-VSA system, respectively. Figure c zooms on a subpart of the F-VSA system and details the nodes' locations and the stiffnesses distribution among the joints.

joints that are not connected to the platform are elastic joints with one rotational DoF along the \hat{z} axis. The stiffnesses of joints are not identical since they are composed of a different number of layers due to our manufacturing process discussed in Appendix 3.3.3. Overall, the joints have four different stiffness values, as shown in Fig. 3.6 with a color map. It is worth noting that we assume that joints shown with white color have zero stiffness because their stiffness is significantly lower than the rest. The joints connected to the central nodes $C_{1,2,3,4}$ have an elastic DoF along the \hat{z} axis, and a passive DoF along the \hat{y} axis represented by the arrows on Fig 3.6a. This passive DoF is the same for the joints directly connected to the platform.

Finally, after assigning all the elements to the F-VSA system's links and joints, we apply the MSA technique [140] step-by-step as summarized in section 3.2.2. The details of the elements'

matrix are given in Appendix A.6. Consequently, we aggregate the MSA model components in the form of (3.2). Then, we derive the relation between end-effector displacement $\Delta \mathbf{t}_e$ and wrench \mathbf{W}_e as follows:

$$\mathbf{W}_{e(6 \times 1)} = (\mathbf{D}_{(6 \times 6)} - \mathbf{C}_{(6 \times 1296)} \cdot \mathbf{A}_{(1296 \times 1296)}^{-1} \cdot \mathbf{B}_{(1296 \times 6)}) \cdot \Delta \mathbf{t}_{e(6 \times 1)} + \mathbf{C}_{(6 \times 1296)} \cdot \mathbf{A}_{(1296 \times 1296)}^{-1} \cdot \mathbf{b}_{(1296 \times 1)} \quad (3.6)$$

from which one can extract the desired stiffness matrix

$$\mathbf{Kc}_{(6 \times 6)} = \mathbf{D}_{(6 \times 6)} - \mathbf{C}_{(6 \times 1296)} \cdot \mathbf{A}_{(1296 \times 1296)}^{-1} \cdot \mathbf{B}_{(1296 \times 6)} \quad (3.7)$$

and the force and torque values at initial condition:

$$\mathbf{W}_{e(6 \times 1)}^0 = \mathbf{C}_{(6 \times 1296)} \cdot \mathbf{A}_{(1296 \times 1296)}^{-1} \cdot \mathbf{b}_{(1296 \times 1)} \quad (3.8)$$

Using the equations (3.6), (3.7), and (3.8), we can calculate the stiffness of the F-VSA's end-effector position based on its configurations. Furthermore, we can find the force output at both initial and current configurations. Thus, the proposed model allows to control the stiffness and force output of the F-VSAs.

3.3.5 Force and stiffness control strategy

We present a strategy to control the force and stiffness of the F-VSA system. By virtue of its interconnected compliant elements, the F-VSA system acts as a multi-axis and variable stiffness series elastic actuator. Thus, by driving the F-VSA system to a specific configuration, we actively control its stiffness and force output in \hat{x} , \hat{y} , \hat{z} , and $\hat{\theta}$ directions, where θ corresponds to rotation in the \hat{z} axis. To achieve that, we use eight linear actuators to modulate the position of the diamonds' attachment points. By changing the compression of the diamonds, we drive the end-effector to its new position, which minimizes the overall energy stored in all joints' virtual springs. After the configuration change, there are two cases: either the end-effector's position stays the same or is moved. In the first case, we modify the energy required to move it or, in other words, the stiffness. In the second case, we induce motion or force output at the end-effector.

To be able to change the stiffness and force output of the F-VSA system's end-effector in a controlled manner, we use the model proposed in section 3.3.4. We write the equation (3.6) in simplified form as follows:

$$\mathbf{W}_{(6 \times 1)} = \mathbf{Kc}_{(6 \times 6)} \Delta \mathbf{t}_{e(6 \times 1)} + \mathbf{W}_{e(6 \times 1)}^0 \quad (3.9)$$

where $\mathbf{W}_{(6 \times 1)}$ and $\mathbf{W}_{e(6 \times 1)}^0$ are the force and torque vector felt by the user at the end-effector when its position is changed by $\Delta \mathbf{t}_{e(6 \times 1)}$ displacement vector and at the initial configuration. $\mathbf{Kc}_{(6 \times 6)}$ is the stiffness matrix of the end-effector.

In fact, the stiffness matrix $\mathbf{K}_{(6 \times 6)}$ and wrench matrix at the initial conditions $\mathbf{W}_{e(6 \times 1)}^0$ are functions of the end-effector position and orientation, and eight linear motor position inputs which are presented by $\mathbf{X}_{(6 \times 1)}$ and $\mathbf{U}_{(8 \times 1)}$ respectively. Thus, we can rewrite the equation (3.9) as follows:

$$\mathbf{W}_{(6 \times 1)} = \mathbf{K}_{(6 \times 6)}(\mathbf{X}_{(6 \times 1)}, \mathbf{U}_{(8 \times 1)}) \Delta \mathbf{t}_{e(6 \times 1)} + \mathbf{W}_{e(6 \times 1)}^0(\mathbf{X}_{(6 \times 1)}, \mathbf{U}_{(8 \times 1)}) \quad (3.10)$$

The equations (3.7) and (3.10) allow us to predict and control the stiffness and force output at the end-effector for a given end-effector position and orientation $\mathbf{X}_{(6 \times 1)}$, motor positions $\mathbf{U}_{(8 \times 1)}$, and end-effector displacement $\Delta \mathbf{t}_{e(6 \times 1)}$. Creating and solving these equations which include the inversion of a (1296 x 1296) matrix, take 1.5 seconds utilizing *Julia* programming language's default functions. Since it is not fast enough for real-time control applications, we created a lookup table with stiffness $\mathbf{K}_{(6 \times 6)}$ and initial wrench matrix $\mathbf{W}_{e(6 \times 1)}^0$ for different end-effector $\mathbf{X}_{(6 \times 1)}$ and motor positions $\mathbf{U}_{(8 \times 1)}$. This lookup table also includes the singular configurations mentioned in section 3.2.2 and can be used to move the F-VSA system into fully rigid configurations.

3.3.6 Actuators and sensing

We use standard servo motors (*TowerPro MG92B* - 0.3 Nm peak torque, 13 rad/s peak speed, 180 deg rotation) coupled with a custom gear rack mechanism to generate linear motion on the vertices of the eight outer diamond patterns. These servos and gear-rack mechanisms are fixed on an outer frame made using a 3 mm thick MDF sheet. We control these servo motors in open-loop as they have internal position-output correction. To measure the end-effector position, we use linear potentiometers (RDC1014A09) attached between $M_{1y} - C_1$, $M_{2x} - C_2$, $M_{3y} - C_3$, and $M_{4x} - C_4$ of Fig. 3.6a. Once the displacements $\|\overrightarrow{M_{1y}C_1}\|$, $\|\overrightarrow{M_{2x}C_2}\|$, $\|\overrightarrow{M_{3y}C_3}\|$, and $\|\overrightarrow{M_{4x}C_4}\|$ are known, we can determine their angles relative to the \hat{z} axis: θ_1 , θ_2 , θ_3 , and θ_4 using the following equations, which gives the angles and therefore the planar coordinates of the central nodes:

$$\begin{cases} \overrightarrow{C_1C_2} + \overrightarrow{C_3C_4} = 0 \\ \overrightarrow{C_1C_4} + \overrightarrow{C_3C_2} = 0 \end{cases} \quad (3.11)$$

For real-time sensing and control of the F-VSA system, we implement a numerical least-squares solver from the *Scipy* package in python.

3.4 Design of experiment

In this section, we design an experimental protocol to test the F-VSA system and compare the results with the model from section 3.3.4. However, the F-VSA system has many independent parameters that make the development of control algorithms challenging. For this reason, these experiments only target a reduced workspace where the lookup table of part 3.3.5 as

control algorithm gives a direct relation between stiffness and position. First, we characterize the stiffness K , of the F-VSA system at different control input values (U). Then, we implement force control at zero displacement, i.e., $X = 0$.

3.4.1 Experimental setup

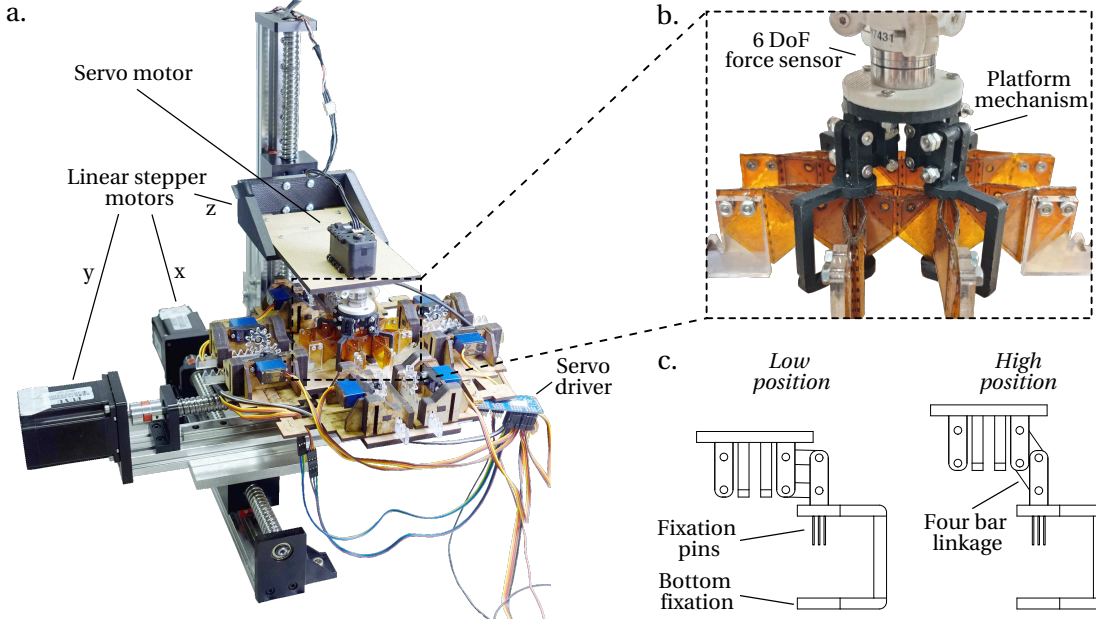


Figure 3.7: Experimental setup design to measure the end-effector force of the F-VSA system in all the workspace. a. Shows the platform that uses three linear stages to move the end-effector along the \hat{x} , \hat{y} and \hat{z} axis. Additionally, we use a servo motor to rotate the end-effector with an angle $\hat{\theta}$. b. In this experimental setup, we replace the origami platform with a custom 3D printed one with the same mechanical behavior. The latter allows to connect the six-DoF force sensor between the servo motor and F-VSA system. c. Fixation pins allow to correctly position and tighten the connection between platform and F-VSA system. In addition, to avoid unwanted motion of the attach between these two elements, we constrain the F-VSA system laterally with a four-bar linkage mechanism, and vertically using a bottom stopper.

As shown by Fig. 3.7a, we designed an experimental setup, to measure the end-effector force in the entire range of motion of the F-VSA system. This setup consists of three linear motors (Fuyu motion) for enforcing displacement on the F-VSA system end-effector in the x , y , and z directions, and a servo motor for enforcing rotational displacement in the $\hat{\theta}$ axis. The x and y linear motors are stacked on each other, and the Medium-Density Fibreboard (MDF) frame of the F-VSA system is rigidly fixed to the \hat{y} -axis linear motor, as seen in Figure 3.7. Similarly, the rotational servo motor is affixed on the \hat{z} -axis linear motor and rigidly connected to the end-effector of the F-VSA system. Attaching the F-VSA system to the experimental setup is challenging because of the complex motion of its end-effector. To address this, we designed a custom 3D printed attachment that fixes the end-effector to the force sensor. This attachment

consists of four four-bar linkages attached to the four vertices of the out-of-plane mechanism. During characterization, the four-bars linkages convert the upward motion of the \hat{z} -axis linear motor into horizontal motion, which compresses the water-bomb diagonally and generates the out-of-plane motion. When moved in the x , y , or θ directions, this attachment also rigidly holds the water-bomb position at the desired displacement. A *Nano17* 6-axis force sensor *ATI Industrial Automation*, force resolution - 12.5 mN is affixed to the servo motor and measures the interaction forces. Finally, to control and communicate with the F-VSA system, we use an *Arduino Mega* and a custom ROS package consisting of control algorithms and GUI.

3.4.2 Stiffness modulation experiment

We characterize the passive structural stiffness of the F-VSA system for different sets of control inputs to the servo motors. In this study, we only consider homogeneous inputs wherein all the motors have the same displacement from their resting position: 0, 1, 2, 3, 4, or 5 mm. Here, a motor displacement of 0 mm corresponds to its resting position when all the diamonds are fully extended and the end-effector cannot move. At a motor displacement of 5 mm, the end-effector can move a much larger distance. Thus, we see that the motion range of the end-effector depends on the motor displacement due to the flattening of the diamond patterns when fully extended. Similarly, they are also prone to collision with neighboring diamond patterns. To address this, we developed a custom algorithm presented in appendix A.5 that calculates the allowable range of motion of the end-effector along the four-DoF for the given control input value.

For every motor input condition, [0, 1, 2, 3, 4, 5 mm], we first find the range of motion of the end-effector in \hat{x} , \hat{y} , \hat{z} , and $\hat{\theta}$ using the aforementioned algorithm. We then define a grid of all possible points in the $xyz\theta$ space, with a resolution of 1 mm in \hat{x} , \hat{y} , and \hat{z} axes, and 5 degrees in the $\hat{\theta}$ axis. We then move the end-effector to each of these points sequentially using the experimental setup, measure the output force for two seconds, and record the average value.

	Force X	Force Y
(+)	$M_{1x} - M_{4x}$	$M_{1y} - M_{2y}$
(-)	$M_{2x} - M_{3x}$	$M_{3y} - M_{4y}$

Table 3.1: Relation between force vector set point and pair of motors to activate as control input.

3.4.3 Force control experiment

Using the model described in section 3.3.4, we demonstrate force control with the F-VSA system. We define a force field in the x - y space use the F-VSA system to deliver the desired output. This virtual field of forces \vec{f} is defined in the form of a vortex as shown in Fig. 3.9b, and is characterized by the following linear mapping:

$$\|\vec{f}\| = \begin{cases} 0 & \text{if } dist = 0 \\ f_{max} \frac{dist_{max} - dist}{dist_{max}} & \text{else} \end{cases} \quad (3.12)$$

$$Angle(\vec{f}) = Angle(\vec{cp}) - \frac{\pi}{2} - \alpha \quad (3.13)$$

where $dist$ is the distance between the vortex center C and the virtual point P position. The maximal distance that can be reached by P is $dist_{max}$. The maximal force amplitude f_{max} is reached for $dist = 0$. Finally, α is an angle offset that orients the vectors toward the center.

Using the experimental setup, we validate if the F-VSA system can generate the above force field. To do so, we define a grid of hundred points in the virtual x - y space of the system, as shown in Fig. 3.9b. For each point, we do the following steps:

1. Calculate the desired force output using Eq. (3.12) and (3.13).
2. Calculate the F-VSA system motor inputs that can provide this force using the lookup table defined in section 3.3.5. Since this experiment only considers 2D force control, we simplify the control problem using only pairs of motors to generate forces along the \hat{x} and \hat{y} directions. The link between forces direction and corresponding motor pair is given by table 3.1.
3. Move the eight motors to the calculated positions to render the desired interaction force.
4. Measure the force applied by the F-VSA system in \hat{x} and \hat{y} axes using the experimental setup.
5. Move the virtual cursor to the next point.

Starting from index point 0, we carry out the steps above and traverse through each point of the grid from index 0 to 99.

	Maximal features	
	Range of motion	Measured force
Planar translation	± 12.5 mm	4.7 N
Normal translation	± 8 mm	10 N
Rotation	± 65 deg	0.41 Nm

Table 3.2: Mechanical capabilities of the F-VSA system. The first column represents the maximal theoretical displacement, while the maximal measured forces are in the second column.

3.5 Experimental results

This section presents and analyses the results of the experiments described in section 3.4. First, we assess the precision of our model by comparing the predicted value with the measure

of the force at the end-effector. Then, the second experiment demonstrates that controlling the end-effector force at zeros displacement is achievable.

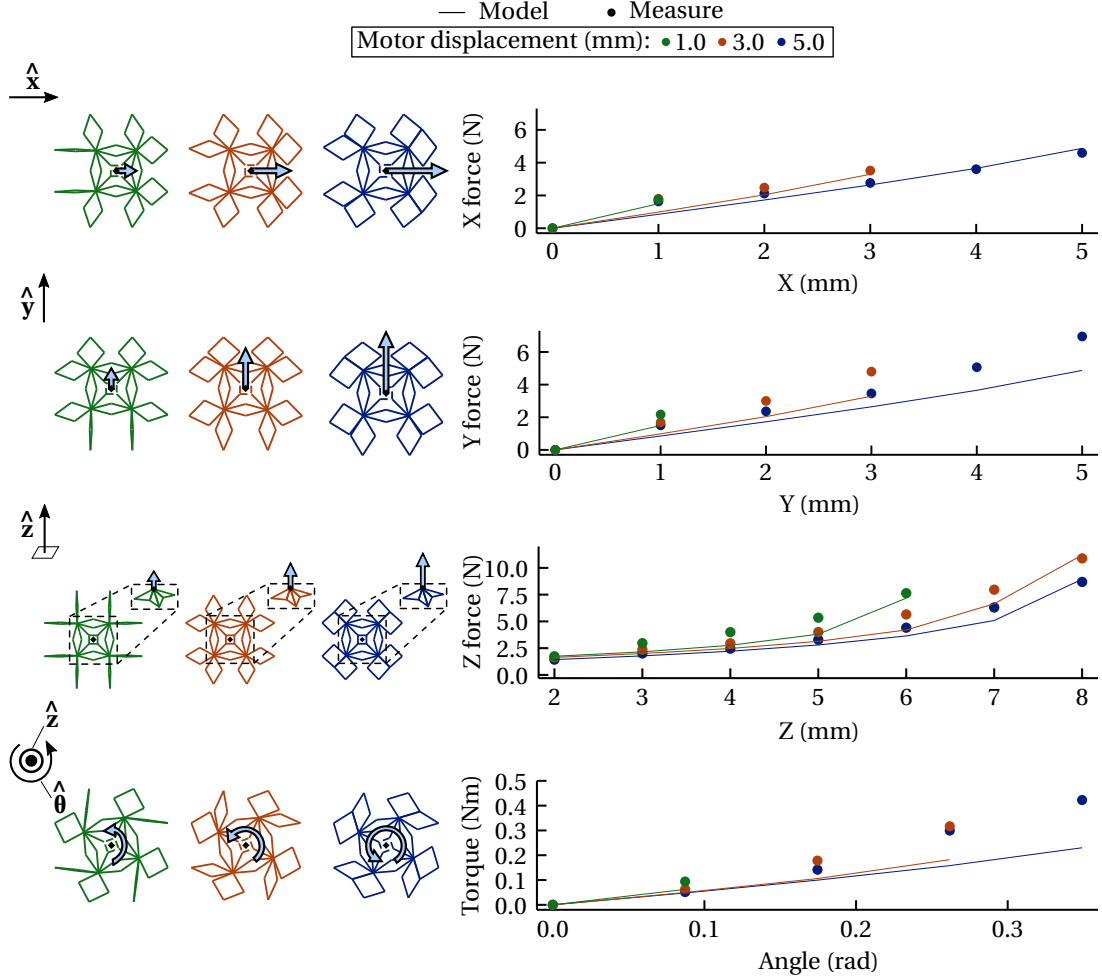


Figure 3.8: Stiffness characterization of the F-VSA system. Comparison between the force measured (scatter plot) and predicted by our model (solid line) for the translation along two axes, rotation, and normal displacement of the F-VSA system end-effector. To reduce the problem dimensions, we only represented a displacement starting from the origin and along one axis at the time for a height of 4 mm. Moreover, the motor displacement programmed for the experiment is the same for the eight servo and consists of a uniform reduction of the arms of 5 mm. The theoretical values are read from the model presented in section 3.3.4.

3.5.1 Stiffness modulation results

The result of the experiment presented by 3.4.2 is represented by Fig. 3.8 that shows four graphs associated with the four-DoF of the end-effector motion: x , y , z , and θ . For ease of presentation, we only show the results corresponding to the end-effector displacement in a single axis at a time. The top left and right graphs correspond to the force output during

uniaxial displacement in \hat{x} and \hat{y} axes respectively. Similarly, the bottom left and right graphs correspond to uniaxial displacement in \hat{z} and $\hat{\theta}$ axes respectively. In all graphs, the markers correspond to the measured data, and the continuous curves correspond to the model prediction. The different colors correspond to the control inputs. From Fig. 3.8, we see that for different motor inputs, the passive stiffness at the end-effector is different with the largest change in the \hat{x} , \hat{y} , and \hat{z} axes.

For the \hat{x} and \hat{y} axes, the end-effector force acts diagonally across the diamond patterns and therefore induces a moment at the compliant hinges. With increasing motor input, the moment arm of this diagonal force increases, inducing a larger moment. As a result, we see a decrease in the end-effector stiffness with an increase in motor input. In the \hat{z} axis, the external diamonds extend for a positive displacement, compress for a negative displacement. Similarly, the forces are also transformed into diagonal forces during displacement in the \hat{z} axis. Therefore we observe a similar pattern for the \hat{z} axis' stiffness decreases with increasing motor displacement. Lastly, during rotation along the $\hat{\theta}$ axis, four of the external diamonds are extended, and four are compressed. These two effects cancel each other up to some extent, which is why we observe a lesser effect on the stiffness.

The differences between the model and measured values can be attributed to the pretension in the compliant hinges, which is due to inconsistencies in the manufacturing process. This pretension has slight dissimilarities among the different compliant joints and is difficult to assess accurately. In this experiment, we assume the joints to be identical and the resting position of the F-VSA system to be at the center. The inaccuracies of this assumption lead to the asymmetry observed between \hat{x} axis and \hat{y} axis results.

We reported the maximal forces generated by the F-VSA system along the \hat{x} , \hat{y} , \hat{z} , and $\hat{\theta}$ axis in table 3.2.

3.5.2 Force control results

The result of the experiment described by 3.4.3 is given by Fig. 3.9b that shows the desired vs. measured forces in the force field in the area defined in the x - y space. Similarly, Fig. 3.9c shows the desired vs. measured force values in the \hat{x} and \hat{y} directions, measured in sequence while traversing through the grid points in the force field. We observe good agreement between the model and experiments with rms errors of 0.74 N in \hat{x} and 0.94 N in \hat{y} . This demonstrates the capabilities of the F-VSA system to recreate any other force field or impedance by adapting the presented method.

3.6 Conclusion and Future work

SEAs and VSAs are two methods commonly used for applications requiring stable force control performance. SEAs suffer from limited bandwidth due to the constant stiffness of their elastic

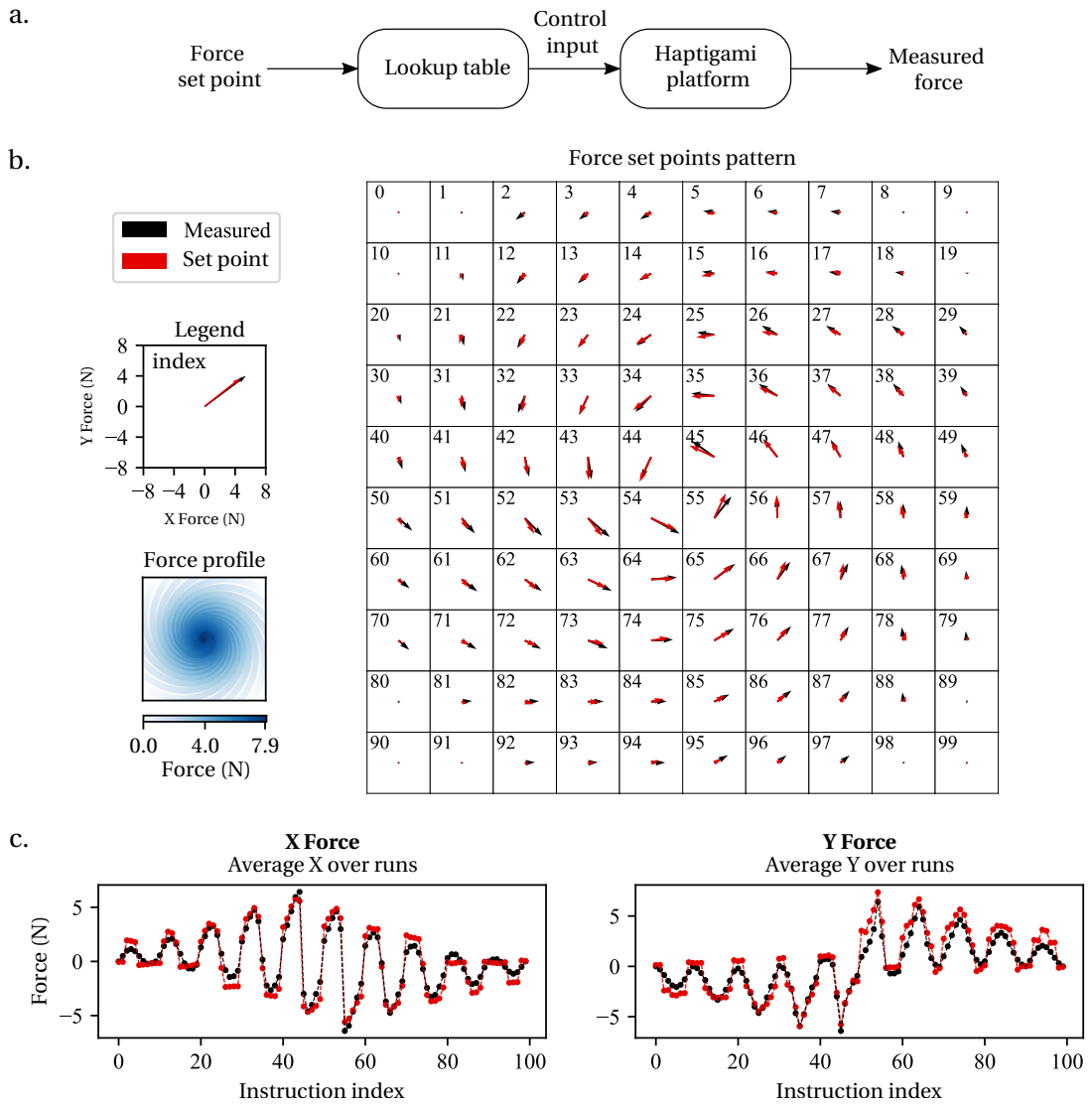


Figure 3.9: Control of the F-VSA system to render a vortex-shaped force field. a. Algorithm used for force tracking: a lookup table returns the motor control inputs associated with the current end-effector position input and desired force set point. In this experiment, the end-effector position is fixed and set to 0. After control of the linear actuators, we measured the force at the end-effector. b and c show the comparison between set point and the average of the measures for over four runs. We sent 100 set points in a vortex shape represented by figure b and compared it with the measured X and Y force values. The result is shown in b as vectors, and in c as plots.

elements. Although VSAs offer a solution by adding the capability to vary the stiffness of elastic elements, they suffer from mechanical complexity and bulkiness since they require several components for actuation, series elasticity, transmission, and structural support. In this chapter, we present flexure variable stiffness actuator (F-VSA), a novel method to address the mechanical complexity of VSAs. F-VSA combines the elements of elasticity, transmission, and variable stiffness by using a repeated folding network made of flexure joints. These joints both define the kinematics of a system and act as virtual springs. F-VSA can render different stiffness values by modulating its geometry by virtue of its design. Thus, it significantly reduces the number of components and parts needed compared to VSAs. Furthermore, the MSA-based stiffness modeling strategy enables active control of the force and stiffness output.

Using the F-VSA method, we designed and developed a four-DoF system with three translations and one rotation. The device can actively induce force output and motion during interaction and change its stiffness along its DoF. To apply force and stiffness control, we modeled the device using the MSA method and characterized it to validate the model. Then, we conducted a comprehensive force control experiment and illustrated that the device successfully generates a force with any direction and amplitude within the device's boundaries. The results show that this design principle can be extended for creating a myriad of multi-DoF devices with tunable stiffness and force output.

Future studies will investigate the inverse kinematic and stiffness model. This will enable the optimization of the F-VSA system design parameters to get the desired mechanical capabilities in force, stiffness, and motion range adapted for a specific application. In addition, there is a need to improve the current control strategy that limits the use of the F-VSA system to configurations associated with a unique stiffness output. Secondly, we will implement additional sensors to monitor metrics such as system geometry or output variables like the force or torque. This will allow closed-loop control and further improve precision. Then, future studies need to consider the plastic deformations of the F-VSA joints under large deformations [144], which is ignored in our current MSA modeling. Finally, one assumption of this study was that the initial resting positions of the compliant joints are well-known. However, inaccurate values or dissimilar resting positions among the repeating elements lead to discrepancies between the model and observed mechanical properties.

Regardless of these limitations, the work presented in this chapter constitutes a new approach to designing compact, scalable, variable stiffness devices with multi-DoF. Similar to VSA, this technology provides safe human-robot interactions for applications such as rehabilitation, or assistive devices. Moreover, increasing the compliant mechanisms' compactness enable the implementation of more functionalities in devices with space constraints such as wearable technologies. The F-VSA low-size and numerous DoF also offer better compatibility with the human complex biomechanics and allow the development of haptic devices with numerous functionalities, or enhanced control interfaces.

4 Robot-computer interface and simulation

In this chapter, we present a framework architecture that provides an high-level control interface allowing robot developers to control, test, and implement custom tasks for their devices. The proposed framework architecture is ROS-based and enables standardized and reusable codes transferable to different robotic platforms, preventing developers from starting every new project from scratch. This interface can be combined with a physics simulation engine where the user interacts with a virtual environment using the hardware's sensors. Depending on the interactive tasks, the simulation sends back data to be processed by the high-level control interface. The interface then controls the hardware's actuators and gives feedback to the user. This framework architecture is designed to be compatible with different hardware and simulation engines. We present a sample application for the Haptigami, F-VSA system, and an hand-grasped haptic device to demonstrate the versatility of this architecture.

4.1 Challenges in robotic software development

Developing novel hardware systems necessitates the creation of customized control interfaces. They enable users to tune the functional specifications of the robot, retrieve data, implement high-level control strategies, and connect it to simulation engines. While this interface is available with the robotic system, it is often challenging to adapt the interface to similar other platforms. This forces developers to re-invent the wheel and re-code standard algorithms from scratch for every novel platform. Moreover, it creates a lack of standard, making it difficult to assess the interface's efficiency.

Robotic Operating System (ROS) [145] solves these issues by offering a standardized open-source environment containing a set of state-of-the-art libraries and tools that significantly fasten, ease, and improve the reliability of robotic development. It implements hardware abstraction tools and simulation engines that allows developers to assess and improve their robot's efficiency in performing tasks without risks for the physical device. These tools connect to both low and high-level control algorithms of the ROS environment and select the most suitable tool for the application and tune its parameters. Furthermore, owing to ROS's efficient

message-passing system, it is convenient for developers to create custom scripts and access data for analysis or processing. Finally, ROS is an open-source environment that enables the community to contribute to, benefit, and learn from existing code. Numerous robotic developers from several fields (aerial [146], manipulation [147], mobility [148], and others) saw the benefit of ROS and delivered the ROS package associated with their device.

ROS is a versatile environment compatible with numerous tasks and robots. This flexibility gives freedom to the users when designing the architecture of a robot's package. However, this creates a lack of standard in the architecture's design. It is sometimes complex for new users to adapt existing codes to their own package. In addition, the architecture's differences create a bias affecting the performance assessment of their robots. It makes sense for a given field and similar robotic systems to use a standardized framework architecture to avoid these limitations and facilitate the framework implementation. This chapter proposes a standard architecture to connect, control, and simulate HRI robots. The developed framework architecture is divided into hardware, high-level control algorithms, and physics simulation engine. The high-level control interface is built using ROS and is compatible with several different hardware and simulation engines chosen to best suit the targeted application. This chapter describes the framework and its implementation for the Haptigami and F-VSA system. Finally, we present a complex application example with a hand-grasped kinesthetic haptic device to demonstrate that this framework can be adapted to other human-robot interface hardware.

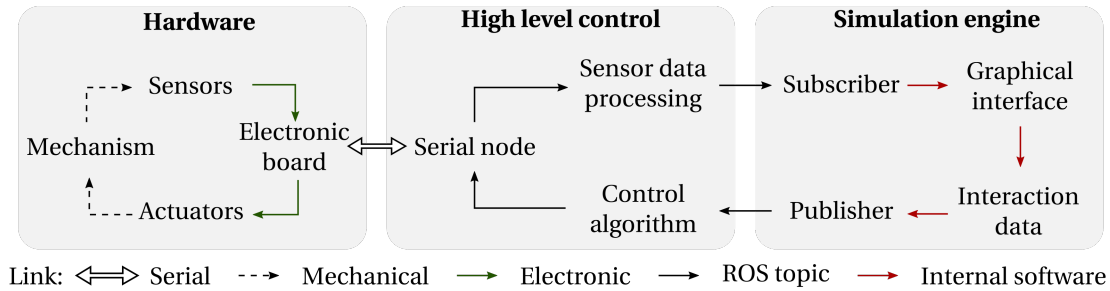


Figure 4.1: General interface architecture. Composed of hardware, high-level control, and simulation engine. The central section is ROS-based and compatible with various hardware and simulation engines. The electronic board extracts data from the sensors and sends it to a ROS node for processing and controlling the simulation. The control node takes the interactions data from the simulation as input and uses it to control the robot's actuators to return feedback to the user.

4.2 Communication interface architecture

This section details the general architecture of the interface interacting with our custom origami robots. Its structure is shown in Fig. 4.1 and consists of three main parts as detailed below.

4.2.1 Hardware

This part is about the robot and its internal components: mechanisms, sensors, actuators, and electronic boards. The latter embeds a loop that continuously interacts with the actuators, sensors, and a serial protocol for communicating with the computer. For every iteration, the board reads all sensors values, categorizes them using labels (“pressure”, “angles”, ...), and sends them to the computer. Each loop iteration also checks for incoming data from the computer. The incoming data are the control instructions for the actuators, such as position and valve duty cycle, etc... These instructions also use labels, thereby allowing the program to distribute them to the corresponding board output.

4.2.2 High-level control

The high-level control interface runs on the computer and is written under the ROS environment. It consists of a set of programs or nodes. Each of them dedicated to a single specific task, such as communication, data processing, etc... They all subscribe to a ROS topic (buses over which nodes exchange messages), analyze, and process the received data, and publish it in another topic. The high-level control software is composed of at least three nodes to communicate with the serial, process and publish the sensor data, and generate the control information from the control algorithm. The node interacting with the hardware by serial communication consists of a loop that waits for the board’s incoming sensor data. These data are parsed and published to their corresponding ROS topic based on their label. This node also subscribes to topics related to actuator control and transfers the instructions to the circuit board through serial communication after labeling them. Depending on the robot, multiple nodes process the sensor data to convert and extract the relevant information and publish them back to the ROS environment or simulation engine. Finally, the control node subscribes to the sensor data and the interactions information from the simulation engine. It inputs these data into a custom or pre-built controller to generate the actuator control commands. These commands are published to the serial communication node and transferred to the hardware. To assist others in developing their own application, it is good practice to include a robot model in the ROS package. This includes the CAD and description files that can be read by simulation engines such as *Unity* [149], *Gazebo* [150], *Rviz* [151] and *PyBullet* [152]. Since the robots described in previous chapters present mechanical closed-chains, the Spatial Data File (SDF) format is preferred. In all other cases, the Unified Robot Description Format (URDF) presents better compatibility with all ROS packages and is recommended.

4.2.3 Simulation engine

The simulation engine can be either custom-made or selected among the existing ones depending on the requirements of the robotic system. Since this engine needs to communicate with the high-level control interface of our architecture, it must include an ROS publisher and subscriber. Owing to the popularity of ROS, this is not a limiting constraint, and most

engines such as *Unity*, *SOFA*, *Gazebo*, or *PyBullet* are capable of interacting with the topics of the ROS control interface. The selection of the simulation engine depends on the application of the robot. For example, *Gazebo* relies on the *bullet* engine and is unable to simulate soft objects, while *Unity*, *PyBullet*, and *SOFA* would be the better choice for virtual reality, robotic, and medical applications, respectively. The simulation engine is the part of our framework that defines a task for the user to achieve with the hardware. The events occurring in the virtual world return information, such as position, contact, and interaction forces, which are published to the high-level control interface through a ROS topic.

4.3 Application examples

The framework described in the previous sections was adapted to the robots developed in this thesis for control and demonstration purposes. The model-based algorithms to control our robots in terms of applied force or position, described in the previous chapter, are currently implemented in the hardware part. In this section, we discuss the development of the high-level control interface and simulation engine necessary to connect with and use our novel robotic systems.

4.3.1 Haptigami

The work presented here demonstrates the linking of the Haptigami to the *Gazebo* simulation engine. For this project, we have access to the custom-made encoders that indicate the motors' angles and, consequently, the Haptigami configuration. These encoders also enable a closed-loop control of the motors when an instruction is received from the computer. We implemented a ROS package to interact with the circuit board of the Haptigami through a serial connection. This package includes an SDF model of the Haptigami, its associated CAD files, and the scripts necessary to start a *Gazebo* simulation environment.

The Haptigami model, objects, and environment are loaded when the simulation is initiated. During the interactions with the object, the Haptigami configuration changes, and its new virtual configuration is reported to the real robot to make the user feel the interaction. To this end, the high-level control interface continuously runs a ROS node that extracts the distances between the top and bottom platforms of the Haptigami. These distances correspond to the lengths of the three tendons that are converted into motor rotations. These rotations are sent to the circuit board through the serial node. Consequently, the real Haptigami follows the simulation in real-time.

For testing the high-level control interface, we implemented a carousel in *Gazebo*, as shown in Fig. 4.2a. It consists of a disc of small thickness with small bumps on its top, regularly spaced over 360°. This carousel's center is fixed in the simulation environment. Only the rotation

of the carousel around the normal axis is permitted. The Haptigami is placed on top of the carousel such that its bottom platform is in contact with the carousel while its top platform is fixed in space. At the beginning of the simulation, the carousel starts rotating, and the orientation of the bottom platform of the Haptigami changes while sliding on the carousel's bumps. Due to the orientation of the bumps, both the roll and pitch of the Haptigami are affected in this simulation. Finally, the orientation changes are reported to the real prototype in real-time. The experimental setup of this demonstration is shown in Fig. 4.2b.

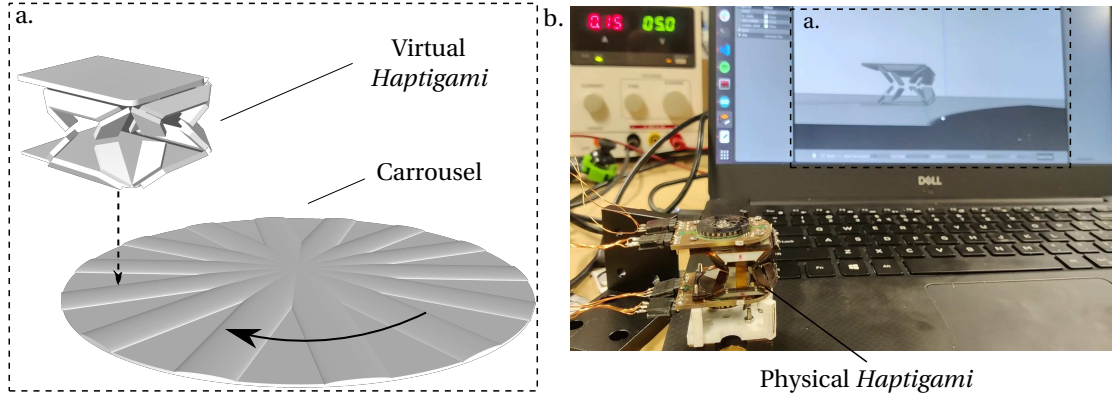


Figure 4.2: Haptigami interface. a. Virtual model of the Haptigami in the Gazebo environment interface. This model is placed on a carousel with bumps that rotate underneath and deform the Haptigami structure. This deformation is processed by the high-level control interface and converted into piezo-motors rotation instructions that control the device; b. Experimental setup where the virtual Haptigami changes the device's configuration in real-time.

4.3.2 F-VSA system

The F-VSA system's working principle, stiffness model, and real-time open-loop control despite the computational expensiveness has already been discussed in the previous chapter. A ROS package communicates with the board and servo driver through the serial node to control the F-VSA system configuration. The position of the end-effector is given by four linear potentiometers, as described in section 3.3.6, and sent to the ROS environment. In this project, the purpose of the high-level control interface is to extract the end-effector position and control the force generated by the device based on this position. For this project, we developed two simple demonstrations that do not require an external simulation tool. The simulation engine was created as a ROS node included in the package.

The first demonstration uses the planar translation of the end-effector to control the position of a cursor on a computer application, which resembles a TrackPoint or nub. As shown in Fig. 4.3a, we attached a 3D printed part to the central nodes of the F-VSA system that can be manipulated by the user. When the simulation starts, the ROS package receives values from the potentiometers and analyses them to determine the end-effector position. The simulation engine uses this value to control the position of the point in real-time, visualized using the

Matplotlib library [153].

The second demonstration shown in Fig. 4.3b is a kinesthetic force feedback haptic joystick. The user controls the cursor like the first demonstration, and a force related to the cursor's position on the screen is provided as feedback. This force field has a vortex shape as defined in the experiment of section 3.4.1. From the cursor position, a node returns the associated force vector, as well as the corresponding motor position given by the force/configuration lookup table. The motor position is then transferred to the hardware using the serial node. Next, the surface reconfigures, making the user feels the virtual vortex.

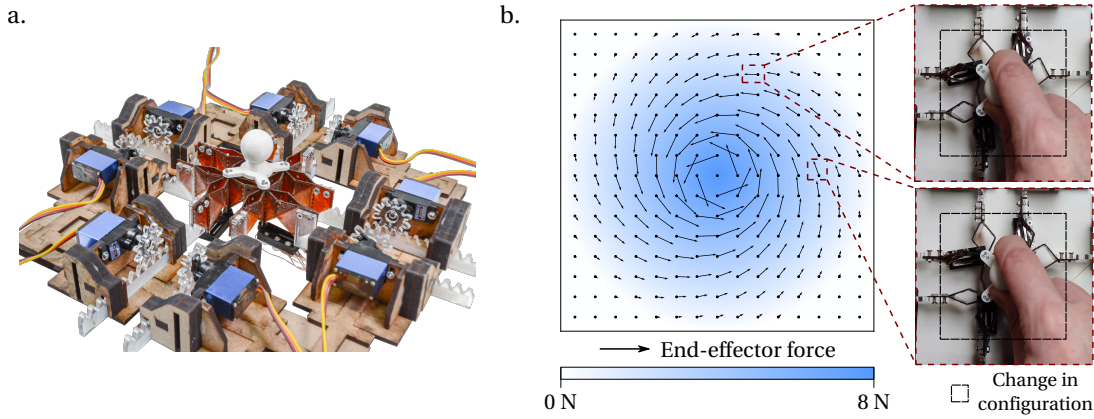


Figure 4.3: F-VSA system interface. a. F-VSA system is equipped with a 3D printed part and serves as a haptic joystick. The user manipulates this end-effector to move a cursor in the simulation, similar to a TrackPoint. In Fig. b, the fold pattern is deformed to render a force at the end-effector depending on the cursor position on the plane. This force pattern is a vortex with a maximum force of 8 N at the center that decreases linearly to a value of 0 N at the extremities.

4.3.3 Hand-grasped kinesthetic haptic device

In this section, we demonstrate the application of the developed framework on a hand-grasped haptic device that renders finger independent kinesthetic force and stiffness feedback. This device has the shape of a hand and is compatible with finger biomechanics. Each of the five fingers is equipped with pneumatic pouches that induce an extension of the finger structures when inflated. By regulating the pressure inside the pouches, the force generated by the fingers is controlled. In addition, the pressure defines the compliance of the pouch and, therefore, can generate stiffness feedback on the finger. This device aims to provide haptic feedback to the user when interacting with soft and hard objects in a virtual environment. Using the architecture presented in section 4.2, we developed the high-level control interface and connected it to the simulation engine *Unity*.

First, the sensors import this device's configuration into the virtual environment. *LeapMotion* is used to get the position and orientation of the palm in space. The finger angles are

given by five flexible sensors in the device and read by the electronic board. The serial node continuously parses and sends these data into the ROS environment, where they are processed to be compatible with Unity. The latter receives these data using the *rosharp* [154] package and displays a capsule hand that follows the position of the real hand in real-time. This virtual hand is a modified version of the *LeapMotion Interaction Engine*'s capsule hand. We adapted it to take the finger angles from the flexible sensors and palm position from leapmotion as inputs.

Most physics engines are efficient at generating contact information between rigid bodies. However, they behave poorly in the case of grasping and tend to push the object away when too much force is applied. The *LeapMotion Interaction Engine* has addressed this problem and proposes an elegant solution by generating a layer around the object that allows the hand to penetrate it and trigger contact without confusing the engine. Each object contains a custom script that continuously sends its material name and the fingers in contact with the object to ROS.

The high-level control interface receives this information and controls only the fingers in contact with the object. The material name is entered into a lookup table that associates the object's stiffness to PID coefficients. These coefficients are sent to the node in charge of the PID that controls the pressure inside the pouches. Harder objects are associated with higher pressure, whereas lower pressure allows rendering the object's compliance. Finally, the PID controller node returns the valves' duty cycles to the circuit board through the serial node.

We used this interface to implement and simulate an interaction with a soft and a rigid object. The user equipped the hand-grasped device and tried to grasp these objects in the simulation engine. Interaction with the rigid object inflated the pouches of the finger in contact to maximum pressure, giving the user an impression of contact with a rigid surface. The soft object gives an intermediate pressure to the pouches, which gives this feedback of softness. We programmed the soft object to visually deform when the virtual hand tries to interact with it to enhance the illusion. This experiment is shown in Fig. 4.4a for the rigid object, and Fig. 4.4b for the soft object.

4.4 Conclusion

This chapter presents a general framework architecture that facilitate the implementation of high-level control and simulation of HRI devices. The part of our framework that deals with the high-level control interface is compatible with several hardware and simulation engines. As a demonstration, we used our framework to interact with two of the devices presented in this thesis and a hand-grasped kinesthetic haptic device. Depending on the application, we connected our high-level control interface to three different simulation engines: Gazebo, Unity, and a custom simulation engine in the form of a ROS node. First, we demonstrated that this architecture allows the computer to command the Haptigami. Next, the F-VSA system and hand-grasped device were demonstrated in closed-loop interactions, where the user gets feedback in response to an action in real-time. Our proposed architecture standardized

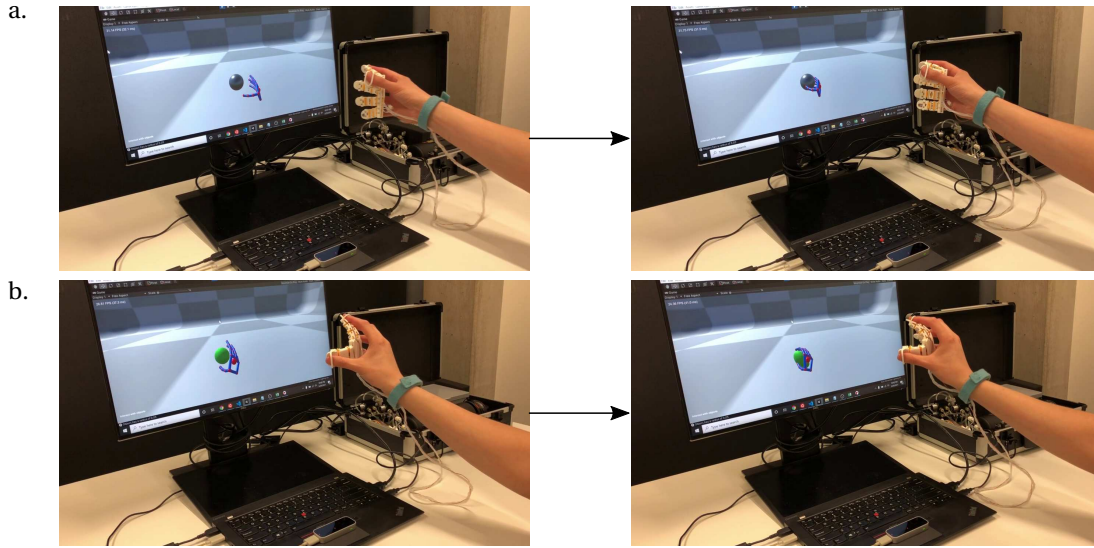


Figure 4.4: Hand-grasped kinesthetic haptic device interface. In this demonstration, we simulate a hand in the virtual environment Unity that follows the motion of the real one through our device's sensors. We used this simulation to interact with two balls of different stiffness: a rigid ball (figure a), and a soft ball (figure b). The high-level control interface activates the fingers in contact with the object and controls the actuator input pressure to render the stiffness depending on the interaction. A high pressure render rigid object while a low pressure gives the feedback of softness. In the latter case, visual feedback is provided by deforming the object in the simulation.

the hardware-computer interface implementation. This promotes re-using of the code and accelerating the product development process. All the tools used in the demonstrations are open source, except for Unity.

The quantitative evaluation of these interactions has not been performed in this thesis as it would have required the creation of novel experimental protocols. In addition, user studies would be required to assess the capabilities of any haptic applications. Moreover, most haptic applications require around 1000Hz as sampling frequency [155], which can be challenging to implement with the current hardware, software, and communication protocols. Our proposed architecture needs to be improved for efficient data processing and visualization in the simulation engine to target the field of haptics. These limitations will be addressed in future works. In this thesis, we developed this robot-computer interface as a way to interact with our robots and to get the data during the experiments presented in the previous chapters. Our framework benefits from the ROS environments in terms of tools, library and state of the art algorithms, and proposes architecture and code re-usable for other robotic platforms. Finally, the application presented in this chapter proves that one can use our framework to achieve interactions with a virtual environment in real-time and with several devices.

5 Conclusion and future outlook

This thesis aimed to develop compact, multi-DoF, and mechanically capable robots for meso-scale interactions with humans. The amalgamation of these three pillars at the meso-scale is challenging for conventional robotics due to the bulkiness of parts, actuators, and the complex 3D assembly of small components. In this study, an alternative approach known as origami robotics was considered. It uses a fast and minimal assembly method to efficiently create scalable mechanisms with numerous flexure joints and DoF. Hence, origami robotics can successfully either improve compactness, provide multiple DoF, or be mechanically capable. However, it still struggles to achieve the trade-off between the three pillars that was envisioned in this thesis. This is because of the challenges in design, kinematics, controls, actuators integration, and meso-scale capabilities.

In this thesis, three robots demonstrating that the aforementioned trade-offs are achievable were developed:

- Our *low-profile compliant transmissions* exhibits potential for the creation of a compact system with tunable and capable mechanical output.
- *Haptigami* has several functionalities integrated into a compact design.
- The flexure variable stiffness actuators (*F-VSA*) demonstrates that origami robotics is a promising approach to achieve the desired trade-off between compactness, DoF, and mechanical capabilities.

Through experiments and demonstrations of these robots, this thesis pushed forward the current limitations of origami robotics with the following contributions:

- Design and manufacturing of compact, multi-DoF, and mechanically capable robots for meso-scale human-machine interaction.
- Development of models, control strategies, and simulation environments suitable for these novel systems.

- Assessment of the proposed robots' capabilities via the creation of adapted characterization platforms and experimental protocols.

Compact, multi-DoF and mechanically capable robots, and control interface

The section provides an overview of the robotic systems developed during this thesis, the manner in which they could be used as fundamental building blocks of future robotic systems, and what future work should be investigated.

Low-profile compliant transmissions

Chapter I presents hybrid transmissions that combine the compactness and minimal assembly-based manufacturing of origami robotics with the kinematic and mechanical efficiency of conventional mechanics. This technology solves the challenges related to the miniaturization of conventional mechanisms. It also overcomes the limitations of origami robotics in terms of complex design and kinematics.

The transmissions benefit from functional material properties that provide additional flexibility to the mechanisms, no longer limited to in-plane motion. They are compatible with conventional actuators such as rotary motors and efficiently transform the input force and motion for the targeted application, paving the way to additional design possibilities. As a demonstration, two well-known and widely used transmission mechanisms were prototyped: slider-crank and cam-follower.

However, there are limitations in the current version of these transmissions. First, the origami manufacturing process is less flexible than standard 3D assembly, which imposes design constraints and limits the kinematic capabilities. Both the mechanisms presented rely on an external elastic origami frame to reset the follower position. Subsequently, the speed and force transmitted depend on the properties of the functional material. This prevents the direct application of the dynamic model for rigid mechanisms. In addition, the impact of different functional materials on transmission capabilities needs to be investigated. For example, stretchable materials may lead to the development of novel series elastic actuators, or more rigid materials may allow reversible motion without the additional origami frames.

Regardless of these limitations, the proposed low-profile compliant transmissions can be used as a building block to create mechanically complex and capable robots without compromising compactness. Their manufacturing process is fast, assembly-free, scalable, and can create other well-known traditional transmissions. In addition, owing to their low-profile, these transmissions can also be considered as layers and stacked into new transmissions or a multi-DoF robot.

Haptigami

Chapter II presents the *Haptigami*, a fingertip haptic device that provides vibrotactile and three-DoF cutaneous feedback. This device solves the challenges of conventional mechanics, where increasing the number of DoF automatically hinders the device compactness as it multiplies mechanisms, parts and actuators. Origami robotics enables reducing the number of parts, but at the cost of complex kinematics that only use pin joints. Moreover, most actuators suffer from capabilities limitations in terms of force and speed at small-scale which affects their abilities to target applications such as HRI.

This robot is currently the most lightweight and smallest haptic system for this number of functionalities. It owes its compactness and mechanical efficiency to low-profile compliant transmissions combined with an under-actuated design, customized piezo-motors, and associated control strategy. The resulting device can render force, speed, and motion compatible with the human cutaneous bandwidth for haptic applications. This project also involved the development of a five-DoF characterization platform to measure the force capabilities of meso-scale systems

However, the high compactness of the *Haptigami* creates constraints in terms of mechanical efficiency. For example, tuning the displacement and force of the compliant transmissions is difficult as it may affect the aspect ratio of the overall device. Moreover, it uses low-profile piezo-motors that cannot be miniaturized without significantly reducing the output force. Furthermore, these actuators are also controlled using a bang-bang controller that does not adjust the output force. Hence, a force control strategy is required for the piezo-motors, such as tuning the piezo's ultrasonic wave frequency, to significantly enhance the *Haptigami*'s range of applications. Finally, a user study is still required to assess the system's efficiency to render feedback to the user.

The *Haptigami* demonstrates that compactness no longer involves a lack of DoF. It illustrates that the low-profile compliant transmissions can be used as building blocks for more complex systems. The design of the *Haptigami* being based on a delta robot, its use as a manipulator base or stacking them into a robotic arm can be envisioned. The design method developed in this study can be applied to multi-scale robotics to enhance the number of DoF by eliminating the limitations caused by bulky materials and complex manufacturing.

Flexure Variable Stiffness Actuator

Chapter III presents the Flexure Variable Stiffness Actuator (F-VSA), which is a novel, compact, multi-DoF, and mechanically capable elastic actuator. Unlike conventional elastic actuators, the F-VSA does not necessitate the assembly of numerous parts and actuators. This reduces the complexity, weight, size, and time of assembly of the robotic system.

The proposed (F-VSA) combines the advantages of Series Elastic Actuators (SEAs) and Variable Stiffness Actuators (VSAs) such as safety, compliance, and force control for human interactions, without affecting their mechanical complexity. It uses origami as the elastic element that acts as transmission, while the inherent stiffness of flexure hinges avoid the assembly

of additional springs. Hence, the *F-VSA* benefits from origami robotics in manufacturing process, multi-DoF compact structure design, and flexure hinge mechanical efficiency. As a demonstration, a prototype capable of rendering four DoF, position, force, and stiffness output at the end-effector was developed. This project also included the development of a characterization platform to assess the force capabilities of the *F-VSA*.

However, the *F-VSA* transmission's numerous DoF are attained at the cost of complex kinematics. Consequently, the design process is laborious, which complicates the system's model and control strategy. In addition, the choice of material and design directly affects the flexure hinges' capabilities and must be optimized for targeting a stiffness range adapted to the application goal. Future studies could tackle these issues by implementing new design strategies and more efficient modeling methods.

This system demonstrates that origami robotics is capable of creating compact and mechanically capable multi-DoF systems, owing to origami flexure hinge's inherent stiffness. It offers a compact alternative to the complexity of *VSA*, is easier to manufacture, scalable, and includes transmissions. In addition, it enables the creation of compliant meso-scale robots better suited for human interactions.

Robot-computer interface and simulation

Chapter IV presents a possible interface architecture to control and connect the hardware of the previous chapters to a simulation engine. The latter allows the development of virtual tasks that the user can achieve through our hardware for human-robot interactions. This architecture is ROS-based and benefits from numerous open-source libraries that facilitate data collection, visualization, and controller creation. It makes easier the development, readability, and re-usability of the code. This framework can be connected to a simulation engine that best suits the task using the ROS environment. The user controls the simulation through the hardware embedded sensors and receives real-time feedback of the simulation through the hardware's actuators.

Future work should enhance the current interface and embedded software to be compatible with more hardware and simulation engines. A major improvement could target the increase of the global refresh rate to at least 1000 Hz to render high stiffness that maintains a passive behavior with impedance control in conventional force feedback. This requires code optimization and consequent improvements in hardware and control strategies. Nevertheless, the *F-VSA* system used as a haptic joystick could also address this limitation. With this project, the natural tunability of the structure's stiffness has the potential to simplify the control since the minute adjustment of the force is made by the mechanical impedance of the structure and not by the feedback control. Finally, the efficiency of this architecture needs to be assessed. It will require developing experimental protocols, assessment methods, and user studies for haptic applications.

The previous chapter also demonstrated that our high-level control interface can be used to create applications for three different systems: the Haptigami, *F-VSA* system, and hand-grasped haptic device. First, a virtual Haptigami is deformed due to virtual interactions, and

this change in configuration is replicated on the real one. Second, the F-VSA joystick was used as a haptic joystick for the user to feel a vortex-shaped force field. Finally, we provided stiffness feedback to the user when a virtual soft or rigid ball was grabbed in the simulation through a hand-grasped haptic device.

Discussion about the thesis contributions

This section presents the contributions of this thesis regarding the creation of compact, multi-DoF, and mechanically capable systems.

Design and manufacturing

Design and manufacturing are tightly linked in origami robotics owing to non-conventional kinematics, layer-by-layer fabrication, and functional materials. Traditional origami fabrication primarily relied on layer cutting, 2D assembly of functional layers, and heat pressing. However, this process could manufacture pin joints only structures, whose combination into other kinematic transmissions increases the complexity of the overall kinematics, design, and requires more space. This thesis explores novel design and manufacturing methods to overcome the complex design and kinematic challenges of origami robotics without hindering the efficiency of its manufacturing process.

Compared to conventional origami robots, our systems necessitate a more challenging manufacturing approach during 2D assembly and heat pressing because of the stack's floating parts and non-uniform thickness. In addition, the complex folding process must be made less laborious through careful design and material selection. This requirement is reflected in the novel origami pattern used in the *F-VSA*. Finally, the most important contribution of this thesis in this category was achieved in the development of low-profile compliant transmissions and the *Haptigami*. These systems are made with a complex stack of layers with multiple materials, internal moving parts, and floating elements. They are challenging to manufacture by conventional layer-by-layer methods. The techniques developed in this thesis to tackle these complex devices can aid in the creation of future origami-inspired robots that will no longer be forced to use flexure hinges as joints exclusively. Therefore, through this study, a pathway to new design and manufacturing methods for complex robotic systems has been provided. This thesis aims to support the development of origami robots that would benefit from low-profile and functional materials to enhance their capabilities and number of DoF. Finally, these methods are compatible with mass production, which aids in the distribution, fabrication time, and cost of robots.

Modeling and low-level control

The robots created in this thesis are composed of multiple DoF, non-conventional actuators, and use material properties to achieve their objective. For this reason, the application of con-

ventional control methods to origami robotics is challenging, and there is a need to investigate new control strategies. The latter also implies the development of new embedded sensing strategies enabling open and closed-loop control. The contributions of this thesis can be divided between positioned-controlled and force controlled-robots.

The proposed low-profile compliant transmission, and consequently the resulting *Haptigami* are positioned-controlled. We used their kinematics similitude with conventional mechanisms and added the constraints induced by the origami robotics design. This includes the flexibility of the material used, and decoupled forward and backward motion of the slider. The *Haptigami* uses the low-profile slider-crank in a folded configuration to control the orientation of the end-effector. Because this fingertip robot is compliant, the kinematics are no longer exclusively dependent on the internal mechanisms and must also consider the deformation caused by the finger. Moreover, the *Haptigami* is under-actuated, which allows for more compactness at the cost of a more complex control strategy. Finally, a custom, compact, and precise encoder integrated into the piezo-motor frame was created.

The *F-VSA* controls the force position and stiffness of the end-effector by modulating the origami configuration. Compared to conventional two-springs *VSA*, the proposed system is composed of numerous elastic joints and mechanical closed-chains that make the application of traditional stiffness models a challenge. In this study, a general method yielding the *F-VSA* stiffness matrix as output for any configuration was adapted and implemented. This method is computationally expensive, and several strategies to make it compatible with real-time applications were explored. Finally, position sensors and associated kinematic models were implemented to obtain the system configuration, which was used as input to the stiffness model.

In summary, this thesis made multiple contributions in the development of position and stiffness model, control strategies, and sensor implementation of multi-DoF, unconventionally, and under-actuated origami robots.

Characterization methods

The development of robotic systems requires a quantifiable method to assess their capabilities. However, most of the strategies used by conventional robotics cannot be transferred to origami systems owing to their compliant properties, numerous DoF, and non-conventional actuation. The primary challenge lies in the size of these robots, as it hinders the integration of actuators and sensors. In this thesis, several characterization platforms and their associated experimental protocols were designed and manufactured to measure the force and speed of the unique robots.

Position characterization was achieved using a vision-based platform, where one or multiple cameras recorded the end-effector displacement. A software-based approach or image processing algorithms were used to extract the end-effector displacement.

Regarding force measurements, the *Haptigami* and *F-VSA*'s end-effector moves along four to five DoF and generates multi-axial forces and torques. Moreover, the force generated is dependent on the motor's actuation and overall system configuration. This thesis created a

multi-DoF characterization platform equipped with a six-DoF force sensor connected to the robot's end-effector. This platform moves the end-effector of meso-scale robots in all the possible workspace and measures the force generated by the system. The proposed characterization protocol aimed to cover sufficient actuation patterns for multiple system configurations and create a database of the measured forces. Finally, methods for attaching the origami robots to the platforms despite the complexity of their crease pattern were investigated.

This work regarding the proposed system's characterization is transferable to any meso-scale robot and can be used by future research for a quantitative assessment of their system.

Broad impact and future work

Through these devices and contributions, the ideas developed during this thesis contribute to pushing the current limits of robotics. The improved origami robots are expected to pave the way for novel design strategies. They will augment the current robotic capabilities, distribution, and their use in everyday life. The fast, cheap, assembly-free, and efficient manufacturing method of origami robots greatly enhances their accessibility for common users. In addition, this fabrication method significantly improves robotics compactness, which presents several advantages. First, it is easier for meso-scale robots to accompany humans all day because their size renders them easily transportable or even wearable. Second, human-robot interactions necessitate mechanisms sized to human biomechanics, and their resolution is directly related to the end-effector's dimensions. Next, reducing the size of the mechanism saves space and enables the implementation of additional functionalities. Consequently, the resulting systems are more capable of handling changing conditions, multiple environments, and daily tasks. There is considerable potential in using the material properties to enhance or create novel functionalities. The inherent stiffness of the joints allows for an increase in capabilities and user safety without requiring additional spring assembly. Furthermore, the material flexibility enables transmissions to go out-of-plane and comply with the user body. It is expected that future studies will investigate the use of stretchable or meta-materials to tune the transmission capability and increase their efficiency.

The actuators' limited capabilities usually impact the output power, speed, and range of motion of robots at the meso-scale. This thesis explored the use of non-conventional actuation methods combined with compact kinematic transmissions to overcome this limitation. However, further investigation is needed for this concept, both in terms of actuation and transmissions. Piezo-motors are still at an early stage of development, and numerous power supply and control challenges need to be addressed. Alternative actuation methods relying on other principles can offer additional advantages and are currently active research fields. Fortunately, the transmissions used in this study are easily customizable and may be compatible with future actuation strategies.

The transmissions are also a promising proof of concept; however, their design must be improved. In addition creating a library of multiple low-profile compliant transmissions can provide engineers with a powerful tool fastening customization and production of robots.

Further studies related to software can automatize design and manufacturing of the mechanisms depending on their output and compactness constraints. This would make mechanical design more accessible for the common user. The designs presented in this thesis may offer novel approaches for developing non-conventional kinematics and transmissions capable of achieving atypical motion that use compliance to adapt to their environment and loading conditions.

Additional functionalities and new multi-task mechanisms create room for developing efficient and challenging control strategies. This thesis focused on model-based approaches to achieve relatively simple tasks. Future work could investigate data-driven approaches to identify our devices' transfer function and offer a clearer view of the control issue that might arise when optimizing the performance. In addition, a constantly changing environment and tasks probably require the investigation of more complex modeling or even reinforcement learning approaches. This requires creating a simulation environment adapted to origami robotics mechanisms and capabilities. This is significant in the case of haptic applications in virtual reality that may account for new capabilities being offered by the proposed systems.

The methods proposed in this thesis could significantly impact numerous HRI fields such as virtual reality, control interfaces, teleoperations, and medical. First, all these fields will benefit from compact haptic interfaces. This feature enables devices to target any body part or be easily embedded in any structure. These haptic interfaces with sufficient mechanical capabilities and DoF could render feedback compatible with various tasks. For example, virtual reality could simulate various shapes, sizes, and stiffness objects. Control interfaces and teleoperation could significantly enhance control performances by adjusting the user's motion. The latter would enable to improve the motion's accuracy or notify the user about the collisions encountered by the remote device. Second, multi-DoF control interfaces could multiply the variety of inputs provided by a user on a single end-effector. Additionally, multiple DoF would allow simultaneous inputs from multiple fingers or body parts by increasing the number of controllable end-effectors. These capabilities would make interactions with machines more intuitive, decreasing the learning time and increasing the efficiency of achieving a task. Finally, such devices will benefit medical applications such as surgery or rehabilitation. This field requires compactness and DoF to fit the body part size or increase the wearability for longer and various rehabilitation exercises. Furthermore, the significant mechanical capabilities of this technology could make assistive robotics less cumbersome. Consequently, it will facilitate the creation of robots for rehabilitation or human augmentation applications and their diffusion. This thesis has focused on one method of bridging the gap between compactness, DoF, and mechanical capabilities, proving that this is an achievable trade-off is feasible. This study also opens many possibilities that require further research to fully exploit and distribute origami-inspired robotics. Nevertheless, the preliminary results obtained are promising, and are expected to serve as fundamental building blocks of future research. Thus, this thesis paves the way for mechanisms with improved capabilities and is a step towards a better collaboration between robots and humans in everyday life.

A Appendices

A.1 Slider-crank mechanism CAD design

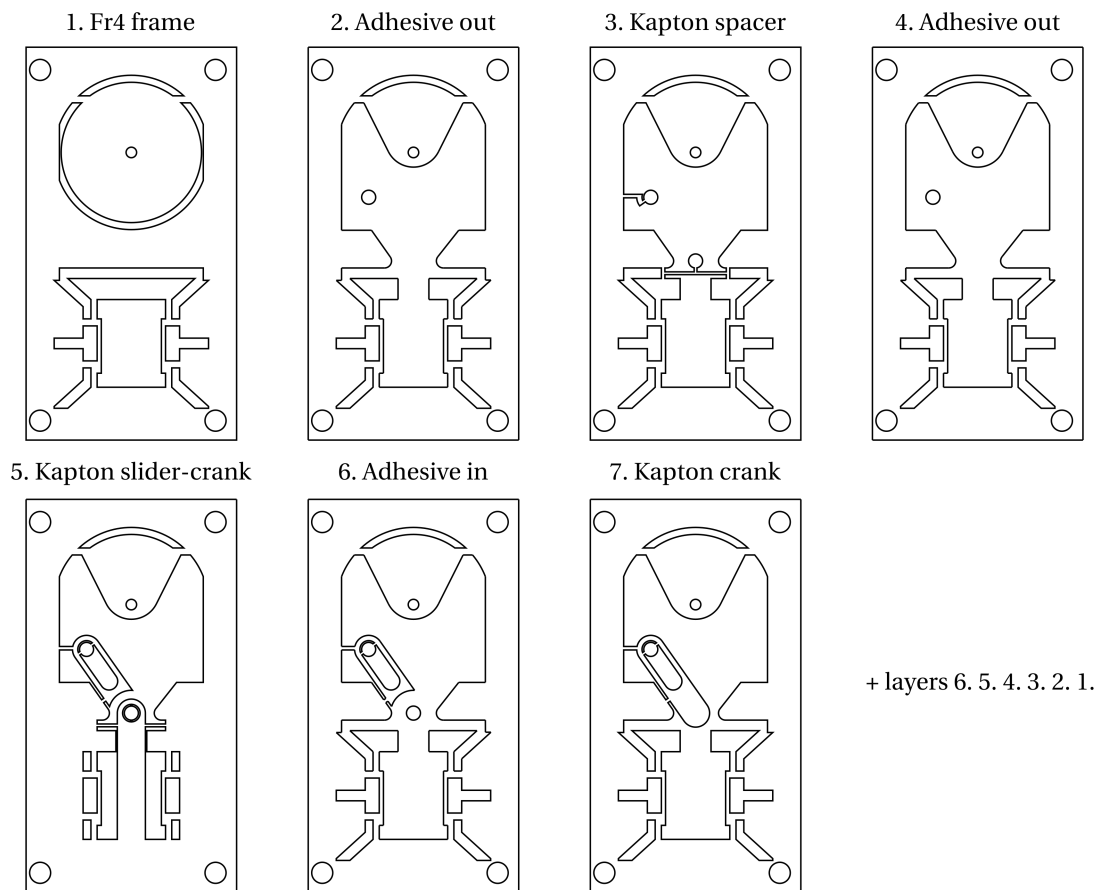


Figure A.1: Slider-crank mechanism CAD design. This mechanism is composed of thirteen layers: two layers of Fr4 define the links; five layers of Kapton for the joints, crank, and slider; six layers of adhesive. Stacking in order layers 1 to 13, heat pressing, and removing the outline and bridges gives the low-profile slider-crank mechanism.

A.2 Cam-follower mechanism CAD design

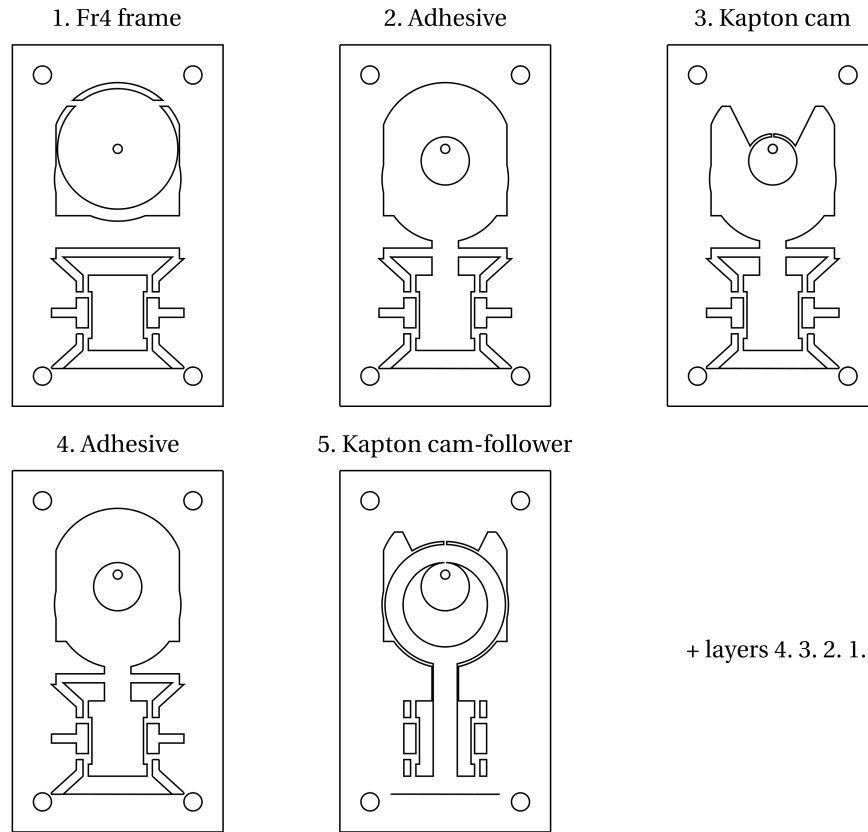


Figure A.2: Cam-follower CAD design. This mechanism is composed of nine layers: two layers of Fr4 define the links; three layers of Kapton for the joints, cam, and slider; and six layers of adhesive. Stacking in order layers 1 to 9, heat pressing, and removing the outline and bridges gives the low-profile cam-follower mechanism.

A.3 Haptigami CAD design

The Haptigami is a complex device composed of twenty-five layers creating four slider-crank mechanisms. The structure is divided into two floors shown by Fig. A.3 and A.4, each including two slider-crank mechanisms. In the case of a manual assembly, it is recommended to manufacture the two floors separately before combining them in the heat press.

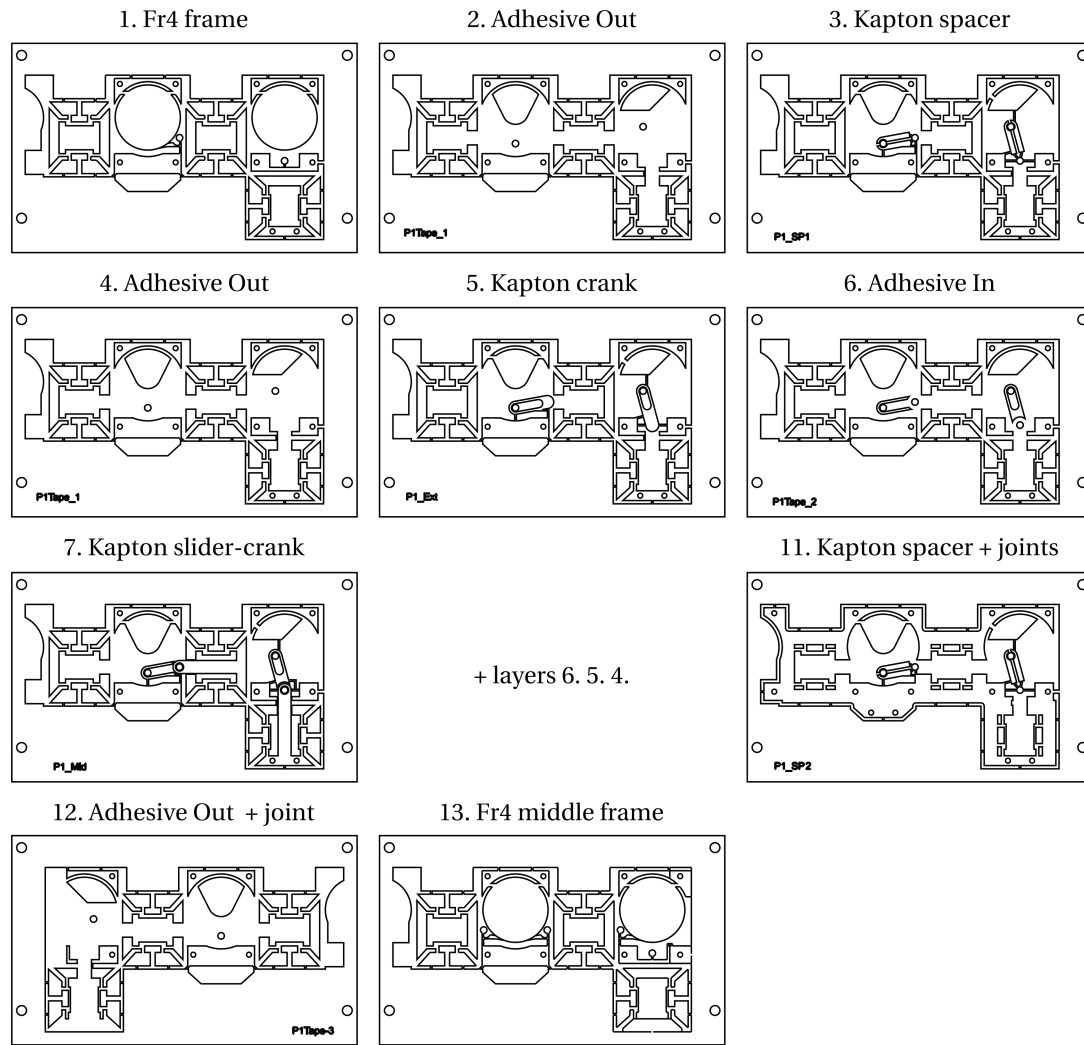


Figure A.3: Haptigami CAD design - floor 1. The first floor of the Haptigami includes two slider-crank mechanisms in charge of the roll. It is composed of thirteen layers: two layers of Fr4 define the links; five layers of Kapton for the joints, crank, and slider; six layers of adhesive. The mechanism is created by stacking in order layers 1 to 13 and heat-pressing. This design enables to remove layer 13's Fr4 on the left part of the left rotor and the link at the very bottom after assembly. This is necessary to create gaps that enable the insertion of layer 11's right and bottom parts during the folding process.

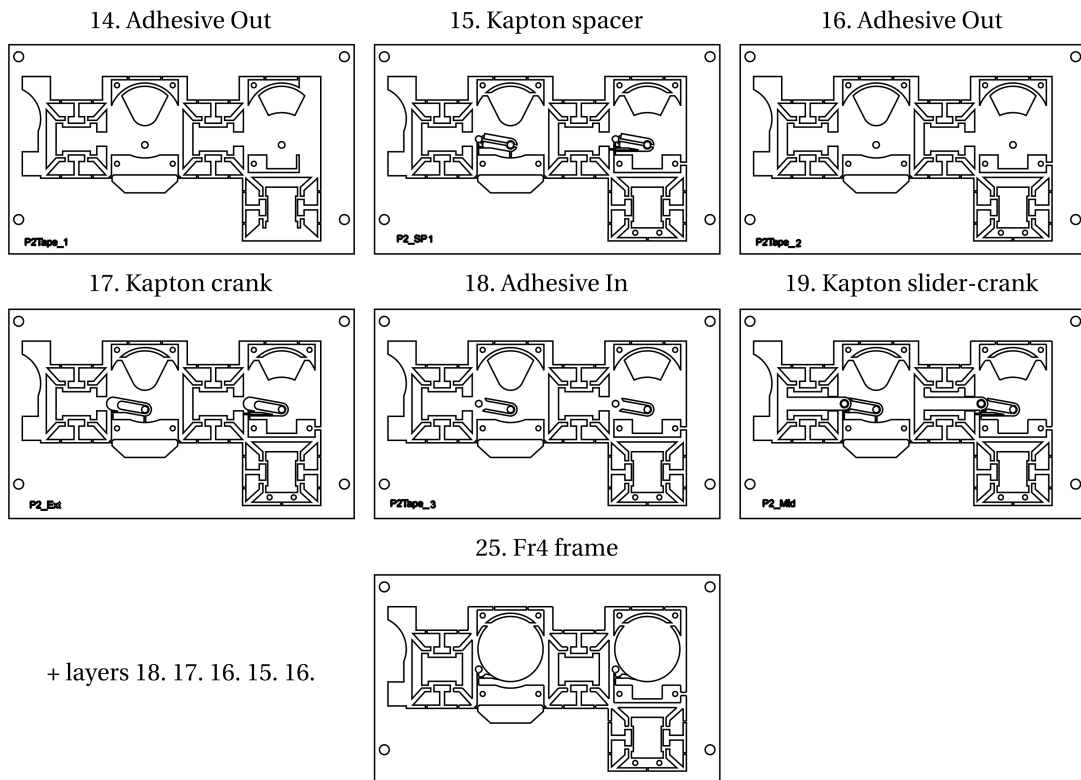


Figure A.4: Haptigami CAD design - floor 2. The second floor of the Haptigami includes two slider-crank mechanisms in charge of the roll and pitch. It is composed of twelve layers: one layers of Fr4 define the links; five layers of Kapton for the joints, crank, and slider; six layers of adhesive. The mechanism is created by stacking in order layers 14 to 25 and heat-pressing.

A.4 F-VSA CAD design

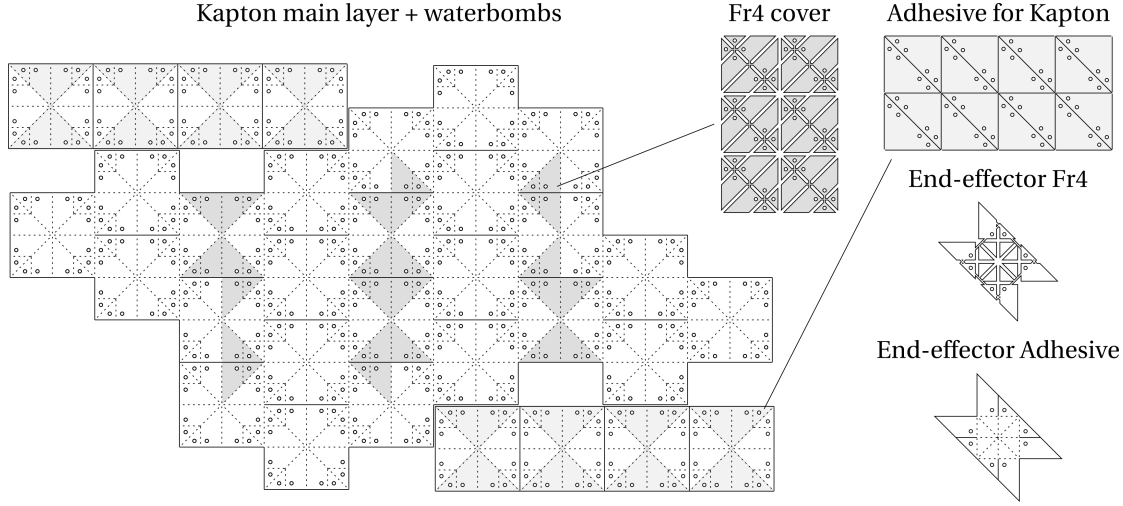


Figure A.5: F-VSA CAD design. This design consists of five elements. First, the Kapton main layer coated with adhesive is cut, aligned with the FR4 cover, heat-pressed, and FR4 bridges are removed. This layer is folded and heat-pressed to create a grid-like origami. Next, extra Kapton waterbombs patterns are folded, coated with a layer of adhesive, inserted into the interstices of the main structure, and fixed using heat-pressing. The end-effector consists of a waterbomb Kapton layer coated with adhesive and attached with FR4. The latter is then inserted into the central square of the main structure grid and fixed using heat-press or screws.

A.5 Workplace determination

The complex structure of the F-VSA system makes some configurations not achievable for the two following reasons. First, the diamonds cannot be extended more than two times the size of their side length. Secondly, during compression, the diamonds are expanding laterally, leading to constraints in terms of space. Indeed, the more the diamonds are compressed, the more the diamonds are prone to get in contact with each other. In this regard, we developed an algorithm able to assess if the Haptigami configuration is correct, given its motor and end-effector position. From these two inputs, this function, called *isHaptigamiCorrect*, deduces the position of all Haptigami's vertices and checks if the two aforementioned conditions are respected. To compute our device workspace, we use *isHaptigamiCorrect* inside Algorithm 1. The latter tests the configuration for several motor and end-effector positions and returns the list of possible configurations. The final workspace is given by table 3.2 and allows 12.5 mm in x and y displacement, 65 deg in rotation, and 8 mm for the normal displacement.

Algorithm 1 Algorithm used to compute the possible workspace of the Haptigami

```

motor_Pos ← list of motor positions
EF_Pos ← list endeffector positions in x, y, z, α
configList ← empty list
for all mP in motor_Pos do
  for all pos in EF_Pos do
    if isHaptigamiCorrect(mP, pos) then
      configList.append([mP, pos])
    end if
  end for
end for

```

A.6 Matrix Structural Analysis

As described by 3.2.2, the first step when applying the MSA method is to describe the system as a set of matrix equations. Let \mathbf{W}_i and $\Delta \mathbf{t}_i$ be respectively the six force and six displacements variables associated with node *i*. Since our system is composed of 109 nodes, the total number of variables is 1308. As indicated by Klimchik et al. [140], the equations for the elements of the F-VSA system presented in section 3.3.4 a.k.a. (i) flexible links, (ii) flexible platform, (iii) passive joints, (iv) elastic joints, (v) passive/elastic joints, (vi) elastic supports and (v) external loadings are:

- (i) **Flexible link:** connects two nodes *i* and *j* through stiffness coefficients associated with the forces and stiffness variables \mathbf{W}_i and $\Delta \mathbf{t}_i$. Each link gives a system of twelve equations, resulting in an aggregated matrix of 624 rows, as presented below:

$$\begin{bmatrix} \{-\mathbf{I}_{ij}\} & \{\mathbf{K}^{ij}\} \end{bmatrix} \cdot \begin{bmatrix} \{\mathbf{W}_{ij}\} \\ \{\Delta \mathbf{t}_{ij}\} \end{bmatrix} = \mathbf{0} \quad (\text{A.1})$$

- (ii) **Flexible platform:** is a set of *n* nodes connected to the end-effector through stiffness coefficients, similar to the flexible link case. The F-VSA system has four nodes linked to the end-effector to create the platform, which results in 30 equations presented as:

$$\begin{bmatrix} \{-\mathbf{I}_{ij}\} & \{\mathbf{K}_{12 \times 12}^{ij}\} \\ \mathbf{0} & \{\mathbf{K}_{12 \times 12}^{ij}\} \end{bmatrix} \cdot \begin{bmatrix} \{\mathbf{W}_{ij}\} \\ \{\Delta \mathbf{t}_{ij}\} \end{bmatrix} = \begin{bmatrix} \mathbf{0} \\ \mathbf{W}_{ext} \end{bmatrix} \quad (\text{A.2})$$

with \mathbf{W}_{ext} the external force applied to the end-effector.

- (iii) **Passive joints:** they are used to connect the F-VSA system's platform to the rest of the system. Each passive joint creates twelve equations, giving a total of 48 rows in its matrix

form:

$$\begin{bmatrix} \mathbf{0} & \{\Lambda_i^r, -\Lambda_j^r\} \\ \{\Lambda_i^r, \Lambda_j^r\} & \mathbf{0} \\ \{\Lambda_i^p\} & \mathbf{0} \\ \{\Lambda_j^p\} & \mathbf{0} \end{bmatrix} \cdot \begin{bmatrix} \{\mathbf{W}_{ij}\} \\ \{\Delta \mathbf{t}_{ij}\} \end{bmatrix} = \mathbf{0} \quad (\text{A.3})$$

assuming all initial conditions null. In this equation, Λ is a matrix made from the joint's orthonormal basis. Λ^r is an aggregation of the base's vector along the rigid directions, while Λ^p only considers the base's vectors along which the motion is free to occur.

- (iv) **Elastic joints:** they connect four nodes to create two joints in the F-VSA system's diamonds. Each joint create twelve equations, giving an aggregated matrix of 288 rows. The Elastic joint matrix is:

$$\begin{bmatrix} \mathbf{0} & \{\Lambda_i^r, -\Lambda_j^r\} \\ \{\mathbf{I}_i, \mathbf{I}_j\} & \mathbf{0} \\ \{\Lambda_i^e\} & \{-\mathbf{K}_i^e \Lambda_i^e, \mathbf{K}_j^e \Lambda_j^e\} \end{bmatrix} \cdot \begin{bmatrix} \{\mathbf{W}_{ij}\} \\ \{\Delta \mathbf{t}_{ij}\} \end{bmatrix} = \mathbf{0} \quad (\text{A.4})$$

considering the initial condition null. In this case, \mathbf{K}^e is the stiffness matrix of the joint along its DoF, and Λ^p is replaced by Λ^e but serves the same function.

- (v) **Passive-Elastic joints:** the planar part of the F-VSA system is connected to the pop-up mechanism through four passive-elastic joints. The latter are two-DoF joints whose \hat{x} axis has been rotated to point toward the platform, acting as elastic joint along the \hat{z} axis, and passive joint along the \hat{y} axis. Since all four joints are interconnected for each of the four central nodes, all four joints are interconnected, each cluster creates 54 equations, for a total of 216 equations. The matrix of a passive-elastic joint is given by:

$$\begin{bmatrix} \mathbf{0} & \{\Lambda_i^r, -\Lambda_j^r\} \\ \{\Lambda_i^r, \Lambda_j^r\} & \mathbf{0} \\ \{\Lambda_i^p\} & \mathbf{0} \\ \{\Lambda_i^e\} & \{-\mathbf{K}_i^e \Lambda_i^e, \mathbf{K}_j^e \Lambda_j^e\} \end{bmatrix} \cdot \begin{bmatrix} \{\mathbf{W}_{ij}\} \\ \{\Delta \mathbf{t}_{ij}\} \end{bmatrix} = \mathbf{0} \quad (\text{A.5})$$

with no pre-loading of the joints.

- (vi) **Elastic support:** similar to the elastic joints, they are used to connect the F-VSA system to the support. Each of them give six equations, for a total of 96 equations. The matrix form of a elastic support is:

$$\begin{bmatrix} \mathbf{0} & \{\Lambda_i^r, -\Lambda_j^r\} \\ \{\Lambda_i^e\} & \{-\mathbf{K}_i^e \Lambda_i^e, \mathbf{K}_j^e \Lambda_j^e\} \end{bmatrix} \cdot \begin{bmatrix} \{\mathbf{W}_{ij}\} \\ \{\Delta \mathbf{t}_{ij}\} \end{bmatrix} = \mathbf{0} \quad (\text{A.6})$$

with no pre-loading of the joints.

- (vii) **External loadings:** Apply the following set of equation for every node under an external

wrench \mathbf{W}_e :

$$\begin{bmatrix} -\mathbf{I}_{6 \times 6} & \mathbf{0} \end{bmatrix} \cdot \begin{bmatrix} \{\mathbf{W}_{ij}\} \\ \{\Delta \mathbf{t}_{ij}\} \end{bmatrix} = \mathbf{W}_e \quad (\text{A.7})$$

Concatenating equations (A.1) to (A.7) while making sure to aggregate the platform equation in last, give the system of equation (3.2). Finally, \mathbf{A} \mathbf{B} \mathbf{C} , and \mathbf{D} can be extracted from this matrix and we use equation (3.4).

A.7 Modeling example: MSA applied to a diamond

This subsection applied the method described in 3.2.2 to a single diamond of the system described by nodes 1 to 9 in Fig. 3.6 b. It is worth noting that the F-VSA system's stiffness can only be found by using the MSA to the whole system at once. Therefore, this subsection is just a detailed example to help the reader understand how to apply the MSA to a simple sub-mechanism.



Figure A.6: MSA model of a single diamond. A single diamond and its end-effector is modeled by nine nodes, four links and six joints. We consider the links flexible and the joints elastic along one-DoF with a stiffness k . The linear actuator is considered as the support and the floating node nine as the end-effector.

1. **System description and force-displacement relations:** As represented by Fig. 3.6b, a single diamond is composed of nine nodes that define four links and six joints. The total number of variables is

$$\text{number of nodes} \times 6 \text{ displacements vars} \times 6 \text{ wrench vars} \quad (\text{A.8})$$

hence 108.

- **Flexible Links:** Four links gives a total of 48 equations, leading to the following matrix:

$$\begin{bmatrix} -\mathbf{I}_{12 \times 12} & \mathbf{0} & \mathbf{0} & \mathbf{0} & \mathbf{K}_{12 \times 12}^{12} & \mathbf{0} & \mathbf{0} & \mathbf{0} \\ \mathbf{0} & -\mathbf{I}_{12 \times 12} & \mathbf{0} & \mathbf{0} & \mathbf{0} & \mathbf{K}_{12 \times 12}^{34} & \mathbf{0} & \mathbf{0} \\ \mathbf{0} & \mathbf{0} & -\mathbf{I}_{12 \times 12} & \mathbf{0} & \mathbf{0} & \mathbf{0} & \mathbf{K}_{12 \times 12}^{56} & \mathbf{0} \\ \mathbf{0} & \mathbf{0} & \mathbf{0} & -\mathbf{I}_{12 \times 12} & \mathbf{0} & \mathbf{0} & \mathbf{0} & \mathbf{K}_{12 \times 12}^{78} \end{bmatrix}_{48 \times 108} \quad (\text{A.9})$$

- **Elastic joints and support:** We assume all joints elastic with a stiffness k and

one-DoF along $\hat{\mathbf{z}}$. Therefore, one can write:

$$\Lambda^r = \begin{bmatrix} 1 & 0 & 0 & 0 & 0 & 0 \\ 0 & 1 & 0 & 0 & 0 & 0 \\ 0 & 0 & 1 & 0 & 0 & 0 \\ 0 & 0 & 0 & 1 & 0 & 0 \\ 0 & 0 & 0 & 0 & 1 & 0 \end{bmatrix}; \Lambda^e = \begin{bmatrix} 0 & 0 & 0 & 0 & 0 & 1 \end{bmatrix} \quad (\text{A.10})$$

The joints between nodes 2,3 and 6,7 create 24 equations and lead to the following matrix:

$$\begin{bmatrix} 0 & 0 & 0 & 0 & 0 & 0 & 0 & 0 & \Lambda^r & -\Lambda^r & 0 & 0 & 0 & 0 & 0 & 0 \\ 0 & 0 & 0 & 0 & 0 & 0 & 0 & 0 & 0 & 0 & \Lambda^r & -\Lambda^r & 0 & 0 & 0 & 0 \\ 0 & 1 & 1 & 0 & 0 & 0 & 0 & 0 & 0 & 0 & 0 & 0 & 0 & 0 & 0 & 0 \\ 0 & 0 & 0 & 0 & 1 & 1 & 0 & 0 & 0 & 0 & 0 & 0 & 0 & 0 & 0 & 0 \\ 0 & \Lambda^e & 0 & 0 & 0 & 0 & 0 & 0 & k\Lambda^e & -k\Lambda^e & 0 & 0 & 0 & 0 & 0 & 0 \\ 0 & 0 & 0 & 0 & 0 & \Lambda^e & 0 & 0 & 0 & 0 & 0 & k\Lambda^e & -k\Lambda^e & 0 & 0 & 0 \end{bmatrix}_{24 \times 108} \quad (\text{A.11})$$

Since the joints between 4, 9 and 5 are grouped, we can combine 6 equations and write the 18 equations system such as:

$$\begin{bmatrix} 0 & 0 & 0 & 0 & 0 & 0 & 0 & 0 & 0 & \Lambda^r & 0 & 0 & 0 & 0 & -\Lambda^r & 0 \\ 0 & 0 & 0 & 0 & 0 & 0 & 0 & 0 & 0 & 0 & \Lambda^r & 0 & 0 & 0 & -\Lambda^r & 0 \\ 0 & 0 & 1 & 1 & 0 & 0 & 0 & 0 & 0 & 0 & 0 & 0 & 0 & 0 & 1 & 0 \\ 0 & 0 & 0 & \Lambda^e & 0 & 0 & 0 & 0 & 0 & 0 & k\Lambda^e & 0 & 0 & 0 & -k\Lambda^e & 0 \\ 0 & 0 & 0 & 0 & \Lambda^e & 0 & 0 & 0 & 0 & 0 & 0 & k\Lambda^e & 0 & 0 & -k\Lambda^e & 0 \end{bmatrix}_{18 \times 108} \quad (\text{A.12})$$

Finally, this system has two elastic joints linked to the support which lead to 12 equations:

$$\begin{bmatrix} 0 & 0 & 0 & 0 & 0 & 0 & 0 & 0 & 0 & \Lambda^r & 0 & 0 & 0 & 0 & 0 & 0 \\ 0 & 0 & 0 & 0 & 0 & 0 & 0 & 0 & 0 & 0 & \Lambda^r & 0 & 0 & 0 & 0 & 0 \\ \Lambda^e & 0 & 0 & 0 & 0 & 0 & 0 & 0 & 0 & -k\Lambda^e & 0 & 0 & 0 & 0 & 0 & 0 \\ 0 & 0 & 0 & 0 & 0 & 0 & \Lambda^e & 0 & 0 & 0 & 0 & 0 & 0 & -k\Lambda^e & 0 & 0 \end{bmatrix}_{12 \times 108} \quad (\text{A.13})$$

- **External loadings:** are used to constrain the system at the end-effector. We assume that no load apply on the end-effector i.e. $\mathbf{W}_e = \mathbf{0}$

$$[0 \ 0 \ 0 \ 0 \ 0 \ 0 \ 0 \ 0 \ 0 \ -1 \ 0 \ 0 \ 0 \ 0 \ 0 \ 0 \ 0]_{6 \times 108} \quad (\text{A.14})$$

gives the last six equations.

2. **Matrix aggregation:** Concatenating equation (A.9) to (A.14) gives the following system:

$$\begin{bmatrix} \mathbf{A}_{102 \times 102} & \mathbf{B}_{102 \times 6} \\ \mathbf{C}_{6 \times 102} & \mathbf{D}_{6 \times 6} \end{bmatrix} \cdot \begin{bmatrix} \boldsymbol{\mu} \\ \Delta \mathbf{t}_e \end{bmatrix} = \mathbf{0}_{102 \times 1} \quad (\text{A.15})$$

with A an invertible square matrix.

3. **Solve the system:** Finally, as seen in 3.2.2, we use equation (3.4) and (3.5) to find the stiffness matrix $\mathbf{K}_{6 \times 6}$ or the constant force component \mathbf{W}_e^0

Bibliography

- [1] T. B. Sheridan, "Human-robot interaction: status and challenges," *Human factors*, vol. 58, no. 4, pp. 525–532, 2016.
- [2] J. Y. Chen and M. J. Barnes, "Human-robot interaction," *Handbook of human factors and ergonomics*, pp. 1121–1142, 2021.
- [3] A.-N. Sharkawy, "Human-robot interaction: Applications," *arXiv preprint arXiv:2102.00928*, 2021.
- [4] A. Firouzeh and J. Paik, "Robogami: A fully integrated low-profile robotic origami," *Journal of Mechanisms and Robotics*, vol. 7, no. 2, p. 021009, 2015.
- [5] A. Firouzeh, Y. Sun, H. Lee, and J. Paik, "Sensor and actuator integrated low-profile robotic origami," in *2013 IEEE/RSJ International Conference on Intelligent Robots and Systems*, pp. 4937–4944, Ieee, 2013.
- [6] J. Paik, "Soft robot design methodology for 'push-button' manufacturing," *Nature Reviews Materials*, vol. 3, no. 6, p. 81, 2018.
- [7] P. S. Sreetharan, J. P. Whitney, M. D. Strauss, and R. J. Wood, "Monolithic fabrication of millimeter-scale machines," *Journal of Micromechanics and Microengineering*, vol. 22, no. 5, p. 055027, 2012.
- [8] J.-S. Koh and K.-J. Cho, "Omega-shaped inchworm-inspired crawling robot with large-index-and-pitch (lip) sma spring actuators," *IEEE/ASME Transactions On Mechatronics*, vol. 18, no. 2, pp. 419–429, 2012.
- [9] S. Miyashita, S. Guitron, M. Ludersdorfer, C. R. Sung, and D. Rus, "An untethered miniature origami robot that self-folds, walks, swims, and degrades," in *2015 IEEE International Conference on Robotics and Automation (ICRA)*, pp. 1490–1496, IEEE, 2015.
- [10] M. Salerno, K. Zhang, A. Menciassi, and J. S. Dai, "A novel 4-dof origami grasper with an sma-actuation system for minimally invasive surgery," *IEEE Transactions on Robotics*, vol. 32, no. 3, pp. 484–498, 2016.

- [11] H. Shigemune, S. Maeda, Y. Hara, N. Hosoya, and S. Hashimoto, "Origami robot: A self-folding paper robot with an electrothermal actuator created by printing," *IEEE/ASME Transactions on Mechatronics*, vol. 21, no. 6, pp. 2746–2754, 2016.
- [12] Z. Zhakypov, K. Mori, K. Hosoda, and J. Paik, "Designing minimal and scalable insect-inspired multi-locomotion millirobots," *Nature*, vol. 571, no. 7765, pp. 381–386, 2019.
- [13] H. Suzuki and R. J. Wood, "Origami-inspired miniature manipulator for teleoperated microsurgery," *Nature Machine Intelligence*, vol. 2, no. 8, pp. 437–446, 2020.
- [14] J. K. Paik, A. Byoungkwon, D. Rus, and R. J. Wood, "Robotic origamis: Self-morphing modular robot," in *ICMC*, no. CONF, 2012.
- [15] M. T. Tolley, S. M. Felton, S. Miyashita, D. Aukes, D. Rus, and R. J. Wood, "Self-folding origami: shape memory composites activated by uniform heating," *Smart Materials and Structures*, vol. 23, no. 9, p. 094006, 2014.
- [16] R. Niiyama, X. Sun, C. Sung, B. An, D. Rus, and S. Kim, "Pouch motors: Printable soft actuators integrated with computational design," *Soft Robotics*, vol. 2, no. 2, pp. 59–70, 2015.
- [17] Z. Zhakypov, M. Mete, J. Fiorentino, and J. Paik, "Programmable fluidic networks design for robotic origami sequential self-folding," in *2019 2nd IEEE International Conference on Soft Robotics (RoboSoft)*, pp. 814–820, IEEE, 2019.
- [18] X. Sun, S. M. Felton, R. Niiyama, R. J. Wood, and S. Kim, "Self-folding and self-actuating robots: a pneumatic approach," in *Robotics and Automation (ICRA), 2015 IEEE International Conference on*, pp. 3160–3165, IEEE, 2015.
- [19] J. Wang, S. Li, D. Gao, J. Xiong, and P. S. Lee, "Reconfigurable and programmable origami dielectric elastomer actuators with 3d shape morphing and emissive architectures," *NPG Asia Materials*, vol. 11, no. 1, pp. 1–7, 2019.
- [20] Z. Zhakypov, J.-L. Huang, and J. Paik, "A novel torsional shape memory alloy actuator: Modeling, characterization, and control," *IEEE Robotics & Automation Magazine*, vol. 23, no. 3, pp. 65–74, 2016.
- [21] Z. Zhakypov and J. Paik, "Design methodology for constructing multimaterial origami robots and machines," *IEEE Transactions on Robotics*, vol. 34, no. 1, pp. 151–165, 2018.
- [22] Z. Zhakypov, M. Falahi, M. Shah, and J. Paik, "The design and control of the multi-modal locomotion origami robot, tribot," in *2015 IEEE/RSJ International Conference on Intelligent Robots and Systems (IROS)*, pp. 4349–4355, IEEE, 2015.
- [23] S. Miyashita, C. D. Onal, and D. Rus, "Self-pop-up cylindrical structure by global heating," in *Intelligent Robots and Systems (IROS), 2013 IEEE/RSJ International Conference on*, pp. 4065–4071, IEEE, 2013.

- [24] M. Yao, C. H. Belke, H. Cui, and J. Paik, "A reconfiguration strategy for modular robots using origami folding," *The International Journal of Robotics Research*, vol. 38, no. 1, pp. 73–89, 2019.
- [25] C. Liu, S. Yu, and M. Yim, "A fast configuration space algorithm for variable topology truss modular robots," in *2020 IEEE International Conference on Robotics and Automation (ICRA)*, pp. 8260–8266, IEEE, 2020.
- [26] S. M. Felton, M. T. Tolley, C. D. Onal, D. Rus, and R. J. Wood, "Robot self-assembly by folding: A printed inchworm robot," in *2013 IEEE International Conference on Robotics and Automation*, pp. 277–282, IEEE, 2013.
- [27] S. Felton, M. Tolley, E. Demaine, D. Rus, and R. Wood, "A method for building self-folding machines," *Science*, vol. 345, no. 6197, pp. 644–646, 2014.
- [28] D. W. Haldane, C. S. Casarez, J. T. Karras, J. Lee, C. Li, A. O. Pullin, E. W. Schaler, D. Yun, H. Ota, A. Javey, *et al.*, "Integrated manufacture of exoskeletons and sensing structures for folded millirobots," *Journal of Mechanisms and Robotics*, vol. 7, no. 2, p. 021011, 2015.
- [29] A. Pagano, T. Yan, B. Chien, A. Wissa, and S. Tawfick, "A crawling robot driven by multi-stable origami," *Smart Materials and Structures*, vol. 26, no. 9, p. 094007, 2017.
- [30] D. Jeong and K. Lee, "Design and analysis of an origami-based three-finger manipulator," *Robotica*, vol. 36, no. 2, pp. 261–274, 2018.
- [31] A. Rafsanjani, Y. Zhang, B. Liu, S. M. Rubinstein, and K. Bertoldi, "Kirigami skins make a simple soft actuator crawl," *Science Robotics*, vol. 3, no. 15, p. eaar7555, 2018.
- [32] M. Luo, R. Yan, Z. Wan, Y. Qin, J. Santoso, E. H. Skorina, and C. D. Onal, "Orisnake: Design, fabrication, and experimental analysis of a 3-d origami snake robot," *IEEE Robotics and Automation Letters*, vol. 3, no. 3, pp. 1993–1999, 2018.
- [33] S. Mintchev, M. Salerno, A. Cherpillod, S. Scaduto, and J. Paik, "A portable three-degrees-of-freedom force feedback origami robot for human–robot interactions," *Nature Machine Intelligence*, vol. 1, no. 12, pp. 584–593, 2019.
- [34] S. G. Faal, F. Chen, W. Tao, M. Agheli, S. Tasdighikalat, and C. D. Onal, "Hierarchical kinematic design of foldable hexapedal locomotion platforms," *Journal of Mechanisms and Robotics*, vol. 8, no. 1, p. 011005, 2016.
- [35] P. Birkmeyer, K. Peterson, and R. S. Fearing, "Dash: A dynamic 16g hexapedal robot," in *Intelligent Robots and Systems, 2009. IROS 2009. IEEE/RSJ International Conference on*, pp. 2683–2689, IEEE, 2009.
- [36] F. H. Giraud, Z. Zhakypov, and J. Paik, "Design of low-profile compliant transmission mechanisms," in *2019 IEEE/RSJ International Conference on Intelligent Robots and Systems (IROS)*, pp. 2700–2707, 2019.

Bibliography

- [37] F. H. Giraud, S. Joshi, and J. Paik, "Haptigami: a fingertip haptic interface with vibrotactile and 3-dof cutaneous force feedback," *IEEE Transactions on Haptics*, 2021.
- [38] F. H. Giraud, M. Mete, and J. Paik, "Flexure variable stiffness actuators," *Advanced Intelligent Systems*, 2022.
- [39] R. Wood, S. Avadhanula, R. Sahai, E. Steltz, and R. Fearing, "Microrobot design using fiber reinforced composites," *Journal of Mechanical Design*, vol. 130, no. 5, p. 052304, 2008.
- [40] J. K. Paik, R. K. Kramer, and R. J. Wood, "Stretchable circuits and sensors for robotic origami," in *Intelligent Robots and Systems (IROS), 2011 IEEE/RSJ International Conference on*, pp. 414–420, IEEE, 2011.
- [41] C. D. Onal, R. J. Wood, and D. Rus, "An origami-inspired approach to worm robots," *IEEE/ASME Transactions on Mechatronics*, vol. 18, no. 2, pp. 430–438, 2013.
- [42] S. Li, D. M. Vogt, D. Rus, and R. J. Wood, "Fluid-driven origami-inspired artificial muscles," *Proceedings of the National Academy of Sciences*, p. 201713450, 2017.
- [43] R. V. Martinez, C. R. Fish, X. Chen, and G. M. Whitesides, "Elastomeric origami: programmable paper-elastomer composites as pneumatic actuators," *Advanced functional materials*, vol. 22, no. 7, pp. 1376–1384, 2012.
- [44] A. Firouzeh and J. Paik, "Grasp mode and compliance control of an underactuated origami gripper using adjustable stiffness joints," *Ieee/asme Transactions on Mechatronics*, vol. 22, no. 5, pp. 2165–2173, 2017.
- [45] D. H. Myszka, *Machines and mechanisms*. Prentice Hall, 2004.
- [46] J. Angeles and C. S. López-Cajún, *Optimization of cam mechanisms*, vol. 9. Springer Science & Business Media, 2012.
- [47] H. Ellesgaard, E. Johansen, T. Olesen, H. Andersen, and M. H. Hansen, "Electro-mechanical wave device," May 25 2010. US Patent 7,723,900.
- [48] "Pcbmotor website." <https://pcbmotor.com/>, 2012.
- [49] J. Cannan and H. Hu, "Human-machine interaction (hmi): A survey," *University of Essex*, 2011.
- [50] T. Rose, C. S. Nam, and K. B. Chen, "Immersion of virtual reality for rehabilitation-review," *Applied ergonomics*, vol. 69, pp. 153–161, 2018.
- [51] N. Jafari, K. D. Adams, and M. Tavakoli, "Haptics to improve task performance in people with disabilities: A review of previous studies and a guide to future research with children with disabilities," *Journal of rehabilitation and assistive technologies engineering*, vol. 3, p. 2055668316668147, 2016.

- [52] D. P. Losey, C. G. McDonald, E. Battaglia, and M. K. O'Malley, "A review of intent detection, arbitration, and communication aspects of shared control for physical human-robot interaction," *Applied Mechanics Reviews*, vol. 70, no. 1, p. 010804, 2018.
- [53] N. C. Nilsson, S. Serafin, F. Steinicke, and R. Nordahl, "Natural walking in virtual reality: A review," *Computers in Entertainment (CIE)*, vol. 16, no. 2, p. 8, 2018.
- [54] C. Pacchierotti, S. Sinclair, M. Solazzi, A. Frisoli, V. Hayward, and D. Prattichizzo, "Wearable haptic systems for the fingertip and the hand: taxonomy, review, and perspectives," *IEEE transactions on haptics*, vol. 10, no. 4, pp. 580–600, 2017.
- [55] T. Hulin, M. Rothhammer, I. Tannert, S. S. Giri, B. Pleintinger, H. Singh, B. Weber, and C. Ott, "Fingertac—a wearable tactile thimble for mobile haptic augmented reality applications," in *International Conference on Human-Computer Interaction*, pp. 286–298, Springer, 2020.
- [56] H. A. Sonar, A. P. Gerratt, S. P. Lacour, and J. Paik, "Closed-loop haptic feedback control using a self-sensing soft pneumatic actuator skin," *Soft robotics*, vol. 7, no. 1, pp. 22–29, 2020.
- [57] C. Pacchierotti, A. Tirmizi, and D. Prattichizzo, "Improving transparency in teleoperation by means of cutaneous tactile force feedback," *ACM Transactions on Applied Perception (TAP)*, vol. 11, no. 1, pp. 1–16, 2014.
- [58] F. Chinello, M. Malvezzi, C. Pacchierotti, and D. Prattichizzo, "Design and development of a 3rrs wearable fingertip cutaneous device," in *2015 IEEE International Conference on Advanced Intelligent Mechatronics (AIM)*, pp. 293–298, IEEE, 2015.
- [59] D. Leonardis, M. Solazzi, I. Bortone, and A. Frisoli, "A wearable fingertip haptic device with 3 dof asymmetric 3-rsr kinematics," in *2015 IEEE World Haptics Conference (WHC)*, pp. 388–393, IEEE, 2015.
- [60] S. B. Schorr and A. M. Okamura, "Three-dimensional skin deformation as force substitution: Wearable device design and performance during haptic exploration of virtual environments," *IEEE transactions on haptics*, vol. 10, no. 3, pp. 418–430, 2017.
- [61] F. Chinello, C. Pacchierotti, M. Malvezzi, and D. Prattichizzo, "A three revolute-revolute-spherical wearable fingertip cutaneous device for stiffness rendering," *IEEE Transactions on Haptics*, vol. 11, no. 1, pp. 39–50, 2018.
- [62] Y. Mo, A. Song, and H. Qin, "Analysis and performance evaluation of a 3-dof wearable fingertip device for haptic applications," *IEEE Access*, vol. 7, pp. 170430–170441, 2019.
- [63] F. Chinello, M. Malvezzi, D. Prattichizzo, and C. Pacchierotti, "A modular wearable finger interface for cutaneous and kinesthetic interaction: control and evaluation," *IEEE Transactions on Industrial Electronics*, vol. 67, no. 1, pp. 706–716, 2019.

- [64] E. M. Young and K. J. Kuchenbecker, "Implementation of a 6-dof parallel continuum manipulator for delivering fingertip tactile cues," *IEEE transactions on haptics*, vol. 12, no. 3, pp. 295–306, 2019.
- [65] M. Gabardi, M. Solazzi, D. Leonardis, and A. Frisoli, "A new wearable fingertip haptic interface for the rendering of virtual shapes and surface features," in *2016 IEEE Haptics Symposium (HAPTICS)*, pp. 140–146, IEEE, 2016.
- [66] H. Culbertson, S. B. Schorr, and A. M. Okamura, "Haptics: The present and future of artificial touch sensation," *Annual Review of Control, Robotics, and Autonomous Systems*, vol. 1, pp. 385–409, 2018.
- [67] D. Leonardis, M. Solazzi, I. Bortone, and A. Frisoli, "A 3-rsr haptic wearable device for rendering fingertip contact forces," *IEEE transactions on haptics*, vol. 10, no. 3, pp. 305–316, 2016.
- [68] J.-L. Huang, Z. Zhakypov, H. Sonar, and J. Paik, "A reconfigurable interactive interface for controlling robotic origami in virtual environments," *The International Journal of Robotics Research*, vol. 37, no. 6, pp. 629–647, 2018.
- [69] F. H. Giraud, Z. Zhakypov, and J. Paik, "Design of low-profile compliant transmission mechanisms," in *2019 IEEE/RSJ International Conference on Intelligent Robots and Systems (IROS)*, pp. 2700–2707, IEEE, 2019.
- [70] S. Scheggi, L. Meli, C. Pacchierotti, and D. Prattichizzo, "Touch the virtual reality: using the leap motion controller for hand tracking and wearable tactile devices for immersive haptic rendering," in *ACM SIGGRAPH 2015 Posters*, pp. 1–1, 2015.
- [71] D. Tsetserukou, S. Hosokawa, and K. Terashima, "Linktouch: A wearable haptic device with five-bar linkage mechanism for presentation of two-dof force feedback at the fingerpad," in *2014 IEEE Haptics Symposium (HAPTICS)*, pp. 307–312, IEEE, 2014.
- [72] M. Solazzi, A. Frisoli, and M. Bergamasco, "Design of a novel finger haptic interface for contact and orientation display," in *2010 IEEE Haptics Symposium*, pp. 129–132, IEEE, 2010.
- [73] D. Prattichizzo, F. Chinello, C. Pacchierotti, and M. Malvezzi, "Towards wearability in fingertip haptics: a 3-dof wearable device for cutaneous force feedback," *IEEE Transactions on Haptics*, vol. 6, no. 4, pp. 506–516, 2013.
- [74] I. Sarakoglou, N. G. Tsagarakis, and D. G. Caldwell, "A compact tactile display suitable for integration in vr and teleoperation," in *2012 IEEE International Conference on Robotics and Automation*, pp. 1018–1024, IEEE, 2012.
- [75] S.-C. Kim, C.-H. Kim, G.-H. Yang, T.-H. Yang, B.-K. Han, S.-C. Kang, and D.-S. Kwon, "Small and lightweight tactile display (salt) and its application," in *World Haptics 2009-Third Joint EuroHaptics conference and Symposium on Haptic Interfaces for Virtual Environment and Teleoperator Systems*, pp. 69–74, IEEE, 2009.

-
- [76] G. Frediani, D. Mazzei, D. E. De Rossi, and F. Carpi, "Wearable wireless tactile display for virtual interactions with soft bodies," *Frontiers in bioengineering and biotechnology*, vol. 2, p. 31, 2014.
- [77] I. M. Koo, K. Jung, J. C. Koo, J.-D. Nam, Y. K. Lee, and H. R. Choi, "Development of soft-actuator-based wearable tactile display," *IEEE Transactions on Robotics*, vol. 24, no. 3, pp. 549–558, 2008.
- [78] K. Minamizawa, S. Fukamachi, H. Kajimoto, N. Kawakami, and S. Tachi, "Gravity grabber: wearable haptic display to present virtual mass sensation," in *ACM SIGGRAPH 2007 emerging technologies*, pp. 8–es, 2007.
- [79] M. Bianchi, E. Battaglia, M. Poggiani, S. Ciotti, and A. Bicchi, "A wearable fabric-based display for haptic multi-cue delivery," in *2016 IEEE haptics symposium (HAPTICS)*, pp. 277–283, IEEE, 2016.
- [80] A. Frisoli, M. Solazzi, F. Salsedo, and M. Bergamasco, "A fingertip haptic display for improving curvature discrimination," *Presence: Teleoperators and Virtual Environments*, vol. 17, no. 6, pp. 550–561, 2008.
- [81] B. T. Gleeson, S. K. Horschel, and W. R. Provancher, "Design of a fingertip-mounted tactile display with tangential skin displacement feedback," *IEEE Transactions on Haptics*, vol. 3, no. 4, pp. 297–301, 2010.
- [82] A. Girard, M. Marchal, F. Gosselin, A. Chabrier, F. Louveau, and A. Lécuyer, "Haptip: Displaying haptic shear forces at the fingertips for multi-finger interaction in virtual environments," *Frontiers in ICT*, vol. 3, p. 6, 2016.
- [83] M. Hosseini, Y. Pane, A. Sengül, J. De Schutter, and H. Bruyninckx, "A novel haptic glove (exoten-glove) based on twisted string actuation (tsa) system for virtual reality," in *International Conference on Human Haptic Sensing and Touch Enabled Computer Applications*, pp. 612–622, Springer, 2018.
- [84] R. Fagiani, F. Massi, E. Chatelet, Y. Berthier, and A. Akay, "Tactile perception by friction induced vibrations," *Tribology International*, vol. 44, no. 10, pp. 1100–1110, 2011.
- [85] S. Pabon, E. Sotgiu, R. Leonardi, C. Brancolini, O. Portillo-Rodriguez, A. Frisoli, and M. Bergamasco, "A data-glove with vibro-tactile stimulators for virtual social interaction and rehabilitation," in *10th Annual Intl Workshop on Presence*, pp. 345–348, 2007.
- [86] F. Sanfilippo, L. I. Hatledal, and K. Pettersen, "A fully-immersive haptic-audio-visual framework for remote touch," in *Proc. IEEE International Conference on Innovations in Information Technology*, 2015.
- [87] J. Foottit, D. Brown, S. Marks, and A. M. Connor, "Development of a wearable haptic game interface," *arXiv preprint arXiv:1604.08322*, 2016.

- [88] Y. Chen, H. Feng, J. Ma, R. Peng, and Z. You, "Symmetric waterbomb origami," *Proceedings of the Royal Society A: Mathematical, Physical and Engineering Sciences*, vol. 472, no. 2190, p. 20150846, 2016.
- [89] P. K. Mogensen, K. Carlsson, S. Villemot, S. Lyon, M. Gomez, C. Rackauckas, T. Holy, D. Widmann, T. Kelman, D. Karrasch, A. Levitt, A. N. Riseth, C. Lucibello, C. Kwon, D. Barton, J. TagBot, M. Baran, M. Lubin, S. Choudhury, S. Byrne, S. Christ, T. Arakaki, T. A. Bojesen, benneti, and M. R. G. Macedo, "Juliansolvers/nlsolve.jl: v4.5.1," dec 2020.
- [90] Maplesoft, a division of Waterloo Maple Inc., Waterloo, Ontario, "Maple," 2019.
- [91] G. Bradski, "The OpenCV Library," *Dr. Dobb's Journal of Software Tools*, 2000.
- [92] M. Kristan, A. Leonardis, J. Matas, M. Felsberg, R. Pflugfelder, L. Cehovin Zajc, T. Vojir, G. Hager, A. Lukežić, A. Eldesokey, *et al.*, "The visual object tracking vot2017 challenge results," in *Proceedings of the IEEE international conference on computer vision workshops*, pp. 1949–1972, 2017.
- [93] A. Abdouni, M. Djaghoul, C. Thieulin, R. Vargiolu, C. Paillet-Mattei, and H. Zahouani, "Biophysical properties of the human finger for touch comprehension: influences of ageing and gender," *Royal Society open science*, vol. 4, no. 8, p. 170321, 2017.
- [94] B. M. Dzidek, M. J. Adams, J. W. Andrews, Z. Zhang, and S. A. Johnson, "Contact mechanics of the human finger pad under compressive loads," *Journal of The Royal Society Interface*, vol. 14, no. 127, p. 20160935, 2017.
- [95] S. Joshi and J. Paik, "Multi-dof force characterization of soft actuators," *IEEE Robotics and Automation Letters*, vol. 4, no. 4, pp. 3679–3686, 2019.
- [96] S. A. Wall and W. Harwin, "A high bandwidth interface for haptic human computer interaction," *Mechatronics*, vol. 11, no. 4, pp. 371–387, 2001.
- [97] S. J. Lederman and R. L. Klatzky, "Sensing and displaying spatially distributed fingertip forces in haptic interfaces for teleoperator and virtual environment systems," *Presence: Teleoperators & Virtual Environments*, vol. 8, no. 1, pp. 86–103, 1999.
- [98] A. Hein and M. Brell, "Contact-a vibrotactile display for computer aided surgery," in *Second Joint EuroHaptics Conference and Symposium on Haptic Interfaces for Virtual Environment and Teleoperator Systems (WHC'07)*, pp. 531–536, IEEE, 2007.
- [99] I. M. Bullock and A. M. Dollar, "Classifying human manipulation behavior," in *2011 IEEE International Conference on Rehabilitation Robotics*, pp. 1–6, IEEE, 2011.
- [100] M. A. Robertson, H. Sadeghi, J. M. Florez, and J. Paik, "Soft pneumatic actuator fascicles for high force and reliability," *Soft robotics*, vol. 4, no. 1, pp. 23–32, 2017.

-
- [101] Q. Xie, T. Wang, S. Yao, Z. Zhu, N. Tan, and S. Zhu, "Design and modeling of a hydraulic soft actuator with three degrees of freedom," *Smart Materials and Structures*, vol. 29, no. 12, p. 125017, 2020.
- [102] N. Kellaris, V. Gopaluni Venkata, G. M. Smith, S. K. Mitchell, and C. Keplinger, "Peano-hassel actuators: Muscle-mimetic, electrohydraulic transducers that linearly contract on activation," *Science Robotics*, vol. 3, no. 14, p. eaar3276, 2018.
- [103] X. Ji, X. Liu, V. Cacucciolo, Y. Civet, A. El Haitami, S. Cantin, Y. Perriard, and H. Shea, "Untethered feel-through haptics using 18- μ m thick dielectric elastomer actuators," *Advanced Functional Materials*, vol. 31, no. 39, p. 2006639, 2021.
- [104] W. Wang and S.-H. Ahn, "Shape memory alloy-based soft gripper with variable stiffness for compliant and effective grasping," *Soft robotics*, vol. 4, no. 4, pp. 379–389, 2017.
- [105] J. Walker, T. Zidek, C. Harbel, S. Yoon, F. S. Strickland, S. Kumar, and M. Shin, "Soft robotics: A review of recent developments of pneumatic soft actuators," in *Actuators*, vol. 9, p. 3, Multidisciplinary Digital Publishing Institute, 2020.
- [106] P. Boyraz, G. Runge, and A. Raatz, "An overview of novel actuators for soft robotics," in *Actuators*, vol. 7, p. 48, Multidisciplinary Digital Publishing Institute, 2018.
- [107] Y.-J. Kim, S. Cheng, S. Kim, and K. Iagnemma, "A novel layer jamming mechanism with tunable stiffness capability for minimally invasive surgery," *IEEE Transactions on Robotics*, vol. 29, no. 4, pp. 1031–1042, 2013.
- [108] J. Zhou, Y. Chen, Y. Hu, Z. Wang, Y. Li, G. Gu, and Y. Liu, "Adaptive variable stiffness particle phalange for robust and durable robotic grasping," *Soft robotics*, vol. 7, no. 6, pp. 743–757, 2020.
- [109] Y. S. Narang, J. J. Vlassak, and R. D. Howe, "Mechanically versatile soft machines through laminar jamming," *Advanced Functional Materials*, vol. 28, no. 17, p. 1707136, 2018.
- [110] Y.-F. Zhang, N. Zhang, H. Hingorani, N. Ding, D. Wang, C. Yuan, B. Zhang, G. Gu, and Q. Ge, "Fast-response, stiffness-tunable soft actuator by hybrid multimaterial 3d printing," *Advanced Functional Materials*, vol. 29, no. 15, p. 1806698, 2019.
- [111] M. Pan, C. Yuan, X. Liang, T. Dong, T. Liu, J. Zhang, J. Zou, H. Yang, and C. Bowen, "Soft actuators and robotic devices for rehabilitation and assistance," *Advanced Intelligent Systems*, p. 2100140, 2021.
- [112] N. El-Atab, R. B. Mishra, F. Al-Modaf, L. Joharji, A. A. Alsharif, H. Alamoudi, M. Diaz, N. Qaiser, and M. M. Hussain, "Soft actuators for soft robotic applications: a review," *Advanced Intelligent Systems*, vol. 2, no. 10, p. 2000128, 2020.
- [113] G. A. Pratt and M. M. Williamson, "Series elastic actuators," in *Proceedings 1995 IEEE/RSJ International Conference on Intelligent Robots and Systems. Human Robot Interaction and Cooperative Robots*, vol. 1, pp. 399–406, IEEE, 1995.

Bibliography

- [114] H. Vallery, J. Veneman, E. Van Asseldonk, R. Ekkelenkamp, M. Buss, and H. Van Der Kooij, "Compliant actuation of rehabilitation robots," *IEEE Robotics & Automation Magazine*, vol. 15, no. 3, pp. 60–69, 2008.
- [115] C. Lee, S. Kwak, J. Kwak, and S. Oh, "Generalization of series elastic actuator configurations and dynamic behavior comparison," in *Actuators*, vol. 6, p. 26, Multidisciplinary Digital Publishing Institute, 2017.
- [116] P. Agarwal, J. Fox, Y. Yun, M. K. O'Malley, and A. D. Deshpande, "An index finger exoskeleton with series elastic actuation for rehabilitation: Design, control and performance characterization," *The International Journal of Robotics Research*, vol. 34, no. 14, pp. 1747–1772, 2015.
- [117] A. Baldoni, M. Cempini, M. Cortese, S. Crea, M. C. Carrozza, and N. Vitiello, "Design and validation of a miniaturized sea transmission system," *Mechatronics*, vol. 49, pp. 149–156, 2018.
- [118] A. L. Junior, R. M. de Andrade, and A. Bento Filho, "Series elastic actuator: Design analysis and comparison," *Recent Advances in Robotic Systems*, p. 203, 2016.
- [119] Y.-H. Lai, S.-Y. Huang, and C.-C. Lan, "A force-controlled parallel robot for large-range stiffness rendering in three dimensions," *IEEE Robotics and Automation Letters*, 2021.
- [120] B. Vanderborght, A. Albu-Schäffer, A. Bicchi, E. Burdet, D. G. Caldwell, R. Carloni, M. Catalano, O. Eiberger, W. Friedl, G. Ganesh, *et al.*, "Variable impedance actuators: A review," *Robotics and autonomous systems*, vol. 61, no. 12, pp. 1601–1614, 2013.
- [121] A. Lelevé, T. McDaniel, and C. Rossa, "Haptic training simulation," *Frontiers in Virtual Reality*, vol. 1, p. 3, 2020.
- [122] F. Conti and O. Khatib, "A new actuation approach for haptic interface design," *The International Journal of Robotics Research*, vol. 28, no. 6, pp. 834–848, 2009.
- [123] J. Hurst, A. Rizzi, and D. Hobbelen, "Series elastic actuation: Potential and pitfalls," in *International conference on climbing and walking robots*, 2004.
- [124] R. v. Ham, T. Sugar, B. Vanderborght, K. Hollander, and D. Lefeber, "Compliant actuator designs," *IEEE Robotics & Automation Magazine*, vol. 3, no. 16, pp. 81–94, 2009.
- [125] A. Bicchi, G. Tonietti, M. Bavaro, and M. Piccigallo, "Variable stiffness actuators for fast and safe motion control," in *Robotics research. The eleventh international symposium*, pp. 527–536, Springer, 2005.
- [126] S. Wolf, G. Grioli, O. Eiberger, W. Friedl, M. Grebenstein, H. Höppner, E. Burdet, D. G. Caldwell, R. Carloni, M. G. Catalano, *et al.*, "Variable stiffness actuators: Review on design and components," *IEEE/ASME transactions on mechatronics*, vol. 21, no. 5, pp. 2418–2430, 2015.

-
- [127] X. Li, H. Zhu, W. Lin, W. Chen, and K. H. Low, "Structure-controlled variable stiffness robotic joint based on multiple rotary flexure hinges," *IEEE Transactions on Industrial Electronics*, vol. 68, no. 12, pp. 12452–12461, 2020.
- [128] J. Luo, S. Wang, Y. Zhao, and Y. Fu, "Variable stiffness control of series elastic actuated biped locomotion," *Intelligent Service Robotics*, vol. 11, no. 3, pp. 225–235, 2018.
- [129] S. H. Lee, H. J. Lee, K. H. Lee, K. T. Nam, and J. C. Koo, "A novel variable stiffness scotch yoke series elastic actuator for enhanced functional stiffness," *Microsystem Technologies*, vol. 26, pp. 3395–3402, 2020.
- [130] A. Jafari, H. Q. Vu, and F. Iida, "Determinants for stiffness adjustment mechanisms," *Journal of intelligent & robotic systems*, vol. 82, no. 3-4, pp. 435–454, 2016.
- [131] M. Mete and J. Paik, "Closed-loop position control of a self-sensing 3-dof origami module with pneumatic actuators," *IEEE Robotics and Automation Letters*, vol. 6, no. 4, pp. 8213–8220, 2021.
- [132] D. Rus and C. Sung, "Spotlight on origami robots," *Science Robotics*, vol. 3, no. 15, p. eaat0938, 2018.
- [133] D. Rus and M. T. Tolley, "Design, fabrication and control of origami robots," *Nature Reviews Materials*, vol. 3, no. 6, pp. 101–112, 2018.
- [134] G. Palli, G. Berselli, C. Melchiorri, and G. Vassura, "Design of a variable stiffness actuator based on flexures," 2011.
- [135] H. Xin, G. Chen, and B. Li, "Design of a variable stiffness actuator based on beam flexure and bistable mechanism," in *2019 IEEE 9th Annual International Conference on CYBER Technology in Automation, Control, and Intelligent Systems (CYBER)*, pp. 370–374, IEEE, 2019.
- [136] P. Bilancia, G. Berselli, and G. Palli, "Virtual and physical prototyping of a beam-based variable stiffness actuator for safe human-machine interaction," *Robotics and Computer-Integrated Manufacturing*, vol. 65, p. 101886, 2020.
- [137] H. C. Martin, "Introduction to matrix methods of structural analysis(book on matrix methods of structural analysis including truss, beams, coordinate transformations, force and displacement methods, programming, etc)," *NEW YORK, MCGRAW-HILL BOOK CO., 1966. 331 P*, 1966.
- [138] C. Gosselin *et al.*, "Stiffness mapping for parallel manipulators," *IEEE transactions on Robotics and Automation*, vol. 6, no. 3, pp. 377–382, 1990.
- [139] K.-J. Bathe, "Finite element method," *Wiley encyclopedia of computer science and engineering*, pp. 1–12, 2007.

Bibliography

- [140] A. Klimchik, A. Pashkevich, and D. Chablat, “Fundamentals of manipulator stiffness modeling using matrix structural analysis,” *Mechanism and Machine Theory*, vol. 133, pp. 365–394, 2019.
- [141] A. Klimchik, A. Pashkevich, and D. Chablat, “Cad-based approach for identification of elasto-static parameters of robotic manipulators,” *Finite Elements in Analysis and Design*, vol. 75, pp. 19–30, 2013.
- [142] R. Malka, A. L. Desbiens, Y. Chen, and R. J. Wood, “Principles of microscale flexure hinge design for enhanced endurance,” in *2014 IEEE/RSJ International Conference on Intelligent Robots and Systems*, pp. 2879–2885, IEEE, 2014.
- [143] R. M. Neville, F. Scarpa, and A. Pirrera, “Shape morphing kirigami mechanical metamaterials,” *Scientific reports*, vol. 6, no. 1, pp. 1–12, 2016.
- [144] B. Y. Dharmadasa, H. Mallikarachchi, and F. Lopez Jimenez, “Characterizing the mechanics of fold-lines in thin kapton membranes,” in *2018 AIAA Spacecraft Structures Conference*, p. 0450, 2018.
- [145] M. Quigley, K. Conley, B. Gerkey, J. Faust, T. Foote, J. Leibs, R. Wheeler, A. Y. Ng, *et al.*, “Ros: an open-source robot operating system,” in *ICRA workshop on open source software*, vol. 3, p. 5, Kobe, Japan, 2009.
- [146] J. L. Sanchez-Lopez, R. A. S. Fernández, H. Bavle, C. Sampedro, M. Molina, J. Pestana, and P. Campoy, “Aerostack: An architecture and open-source software framework for aerial robotics,” in *2016 International Conference on Unmanned Aircraft Systems (ICUAS)*, pp. 332–341, IEEE, 2016.
- [147] K. A. Khan, “Ros-based control of a manipulator arm for balancing a ball on a plate,” 2017.
- [148] M. Köseoğlu, O. M. Çelik, and Ö. Pektaş, “Design of an autonomous mobile robot based on ros,” in *2017 International Artificial Intelligence and Data Processing Symposium (IDAP)*, pp. 1–5, IEEE, 2017.
- [149] J. K. Haas, “A history of the unity game engine,” 2014.
- [150] N. Koenig and A. Howard, “Design and use paradigms for gazebo, an open-source multi-robot simulator,” in *2004 IEEE/RSJ International Conference on Intelligent Robots and Systems (IROS)(IEEE Cat. No. 04CH37566)*, vol. 3, pp. 2149–2154, IEEE, 2004.
- [151] H. R. Kam, S.-H. Lee, T. Park, and C.-H. Kim, “Rviz: a toolkit for real domain data visualization,” *Telecommunication Systems*, vol. 60, no. 2, pp. 337–345, 2015.
- [152] E. Coumans and Y. Bai, “Pybullet, a python module for physics simulation for games, robotics and machine learning.” <http://pybullet.org>, 2016–2021.

- [153] J. D. Hunter, “Matplotlib: A 2d graphics environment,” *Computing in Science & Engineering*, vol. 9, no. 3, pp. 90–95, 2007.
- [154] M. Bischoff, “ROS SHARP,” June 2019.
- [155] S. D. Laycock and A. Day, “Incorporating haptic feedback for the simulation of a deformable tool in a rigid scene,” *Computers & Graphics*, vol. 29, no. 3, pp. 341–351, 2005.

FRÉDÉRIC GIRAUD

Sentier de la Gare 5,
1020 Renens VD
+33 61 474 0145
fred.g966@gmail.com
Linkedin | Google Scholar



Highlights

PhD candidate in robotics, my research focus in designing, fabricating, modeling, and controlling novel meso-scale robotic platforms for human-robot interactions. I have hands-on experience in multiple disciplinary fields, including computer sciences, multi-scale systems design and manufacturing, and mechanics toward human-machine interfaces and robotics.

Open-source enthusiast, I am eager to explore new disciplines, improve my current skills and contribute to the community.

Education

Ph.D., Robotics and Intelligent Systems <i>École Polytechnique Fédérale de Lausanne, Switzerland</i>	2018 - August 2022
M.S., Microelectronics and Computer Science, major in Biomedical Devices <i>Mines Saint-Etienne (IMT), France</i>	2014 - 2017
M.S. Micro and Nanoelectronics MINELEC <i>Aix-Marseille University, France</i>	2016 - 2017
Bachelor in Physic and Engineering (<i>Preparatory classes</i>) <i>Jean-Perrin, France</i>	2012 - 2014

Skills

Computer Sciences:

- ▷ **Programming Language:** Python ; Julia ; C++ ; C ; Embedded C (*Arduino, STM32, PIC18*) ; CircuitPython ; Java ; VHDL ; Labview (*CLAD*) ; Maple ; Assembly (*8051*) ; Matlab & Simulink
- ▷ **Machine Learning:** Data Analysis and model classification ; Deep Learning (*Pytorch*) ; Reinforcement learning
- ▷ **Simulation:** Robotic Operating System (ROS) ; Gazebo ; PyBullet ; Unity ; Abaqus
- ▷ **Other:** Unix systems ; Latex ; Office

Computer Assisted Design

FreeCad ; Fusion 360 ; SolidWorks

Electronic design and simulation:

KiCad ; Eagle PCB ; Ledit ; Proteus ISIS/ARES ; FPGA (*Vivado with Zedboard*) ; Cadence (*Virtuoso, Spectre*)

Manufacturing:

- ▷ **3D printer:** Filament and resine
- ▷ **Laser cutter:** Trotec Speedy 400 and customized high precision UV lasers
- ▷ **Clean room:** Spin coating ; Oxygen Plasma ; Photolithography ; Evaporation ; Sputtering

Graphics:

Gimp2 ; Inkscape ; Blender ; OpenShot

Research Experiences

Active origami platforms for human-robot interactions <i>PhD. Thesis</i>	Feb. 2018 to Present
--	----------------------

Reconfigurable Robotics Laboratory - École Polytechnique Fédérale de Lausanne, Switzerland

Investigate the advantages of Origami Robotics in creating novel human-robot interfaces with improved mechanical capabilities compared to conventionally designed devices.

During this thesis, I worked on the design, manufacturing, modeling, and control of:

- ▷ *Low-Profile Compliant Transmission Mechanisms*: layer-by-layer manufacturing and control of 2D transmissions.
- ▷ *Haptigami*: a wearable fingertip haptic interface with vibrotactile and three degrees-of-freedom force feedback.
- ▷ *Digits*: development of the hardware and software interface and virtual environment for a hand-grasped wearable Haptic device that renders stiffness feedback.
- ▷ *Flexure Variable Stiffness Actuators*: a novel haptic interface using the origami hinges inherent stiffness to control the end-effector position, force, and stiffness along four degrees of freedom.

Non-invasive brain stimulation and its impact on Brain-Computer Interface Apr. - Sept. 2017

Master's Thesis

Chair in Brain Machine Interfaces - École Polytechnique Fédérale de Lausanne, Switzerland

- ▷ Online removal of transcranial Alternative Current Stimulation (tACS) artefact from EEG channels
- ▷ Study of Brain-Computer Interface paradigm coupled with tACS stimulation

Infrared transmission of a rat's EEG acquired by Organic Transistors Feb. - Mar. 2017

Final year Research Project

Bioelectronic Laboratory - Mines Saint-Etienne (IMT), France

- ▷ Electrical circuit for brain signal conditioning from Organic Electrochemical Transistors (OECTs) and PWM modulation
- ▷ Hardware and software design for infrared PWM demodulation

Soft and stretchable sensor for hand rehabilitation Mar. - Sep. 2016

Master second year internship

Laboratory for soft BioElectronic Interfaces - EPFL, Switzerland

- ▷ Microfabrication of biocompatible and stretchable sensors in a clean room environment
- ▷ Design of an electronic board and software to use these sensors

Development of an optical tactile interface Mar. - Apr. 2015

Master first year internship

Biorobotics laboratory - Aix-Marseille University, France

- ▷ Mathematical theory and software application for finger localization on a glass interface

Printing RFID antennas on flexible supports 2012 - 2014

Bachelor internship

Flexible Electronic Laboratory - Centre de Microelectronique de Provence, France

- ▷ Mathematical modeling of the behavior of RFID antenna
- ▷ Theoretical and experimental comparison of an inkjet-printed RFID with a standard RFID

Additional experiences and achievements

Public outreach:

Presented lab research in conferences, seminars, and lab visits for diverse audiences

Teaching:

Prepared and delivered lectures, mentored student course projects, conducted exercise and laboratory sessions, and supervised students for their semester or thesis projects

Working with patients:

The technology developed for professional and Hackathon's projects required interactions and tests on healthy subjects and patients with motor disabilities

Project leadership:

- ▷ Hackahealth challenge: develop a custom solution for disabled people (two editions) 2019 ; 2021
- ▷ Winner of Start'Innov challenge and best Startup Prize of the Entrepreneuriales 2015 - 2016
- ▷ Organizer of science vulgarization events for hospitalized children through games 2015
- ▷ Activity designer for Illu-Mines, a science vulgarization association 2014-2015

Charity work:

- ▷ Volunteer for Emmaüs France 2014 - 2016
- ▷ Relief worker in Benin for three weeks: installation of lighting in isolated schools 2011

Publications

Giraud, F. H., Zhakypov, Z., & Paik, J. (2019, November). Low-Profile Compliant Transmission Mechanisms. International Conference on Intelligent Robots and Systems (IROS)

Giraud, F. H., Joshi, S., & Paik, J. (2021). *Haptigami*: a wearable fingertip haptic interface with vibrotactile and three degrees-of-freedom force feedback. IEEE Transactions on Haptics + Best poster award (IROS 2019)

Giraud, F. H., Mete, M., & Paik, J. (2022) Flexure Variable Stiffness Actuators. Advanced Intelligent Systems

Personal Information

French ; Fluent english speaker ; Single ; Male ; 27 years old ; Swiss B permit ; Driving license